

LETTER TO THE EDITOR

# A rigorous detection of interstellar CH<sub>3</sub>NCO: An important missing species in astrochemical networks<sup>★,★★</sup>

J. Cernicharo<sup>1</sup>, Z. Kisiel<sup>2</sup>, B. Tercero<sup>1</sup>, L. Kolesníková<sup>3</sup>, I. R. Medvedev<sup>4,5</sup>, A. López<sup>1</sup>, S. Fortman<sup>4</sup>, M. Winnewisser<sup>4</sup>, F. C. de Lucia<sup>4</sup>, J. L. Alonso<sup>3</sup>, and J.-C. Guillemin<sup>6</sup>

<sup>1</sup> Grupo de Astrofísica Molecular, Instituto de CC. de Materiales de Madrid (ICMM-CSIC), Sor Juana Inés de la Cruz 3, Cantoblanco, 28049 Madrid, Spain

e-mail: jose.cernicharo@csic.es

<sup>2</sup> Laboratory of Mm- and Submm- Spectroscopy, Institute of Physics, Polish Academy of Sciences, Al. Lotnikow 32/46, 02-668 Warszawa, Poland

e-mail: kisiel@ifpan.edu.pl

<sup>3</sup> Grupo de Espectroscopía Molecular (GEM), Edificio Quifima, Área de Química-Física, Laboratorios de Espectroscopía y Bioespectroscopía, Parque Científico UVa, Unidad Asociada CSIC, Universidad de Valladolid, 47011 Valladolid, Spain

<sup>4</sup> Department of Physics, The Ohio State University, 191 W. Woodruff Ave, Columbus, OH 43210, USA

<sup>5</sup> Wright State University, 3640 Colonel Glenn Hwy, Dayton, OH 45435, USA

<sup>6</sup> Institut des Sciences Chimiques de Rennes, École Nationale Supérieure de Chimie de Rennes, CNRS, UMR 6226, 11 Allée de Beaulieu, CS 50837, 35708 Rennes Cedex 7, France

Received 9 October 2015 / Accepted 1 February 2016

## ABSTRACT

The recent analysis of the composition of the frozen surface of comet 67P/Churyumov-Gerasimenko has revealed a significant number of complex organic molecules. Methyl isocyanate (CH<sub>3</sub>NCO) is one of the more abundant species detected on the comet surface. In this work we report extensive characterization of its rotational spectrum resulting in a list of 1269 confidently assigned laboratory lines and its detection in space towards the Orion clouds where 399 lines of the molecule have been unambiguously identified. We find that the limited mm-wave laboratory data reported prior to our work require some revision. The abundance of CH<sub>3</sub>NCO in Orion is only a factor of ten below those of HNCO and CH<sub>3</sub>CN. Unlike the molecular abundances in the coma of comets, which correlate with those of warm molecular clouds, molecular abundances in the gas phase in Orion are only weakly correlated with those measured on the comet surface. We also compare our abundances with those derived recently for this molecule towards Sgr B2 (Halfen et al. 2015, ApJ, 812, L5). A more accurate abundance of CH<sub>3</sub>NCO is provided for this cloud based on our extensive laboratory work.

**Key words.** ISM: abundances – ISM: individual objects: Orion KL – ISM: molecules – methods: laboratory: molecular – molecular data – ISM: clouds

## 1. Introduction

Ice mantles on dust grains are formed from the accretion of gas phase molecules during the gravitational collapse of clouds that form new stars and their planetary systems. Surface reactions increase the chemical complexity of the mantles which, when their temperature rises, release their frozen molecular material to the gas phase (Herbst & van Dishoeck 2009). The gas and dust material of the cloud cores formed during the gravitational collapse participate in the formation of giant gas planets and rocky bodies

\* This paper makes use of the following ALMA data: ADS/JAO.ALMA#2011.0.00009.SV. ALMA is a partnership of ESO (representing its member states), NSF (USA), and NINS (Japan) with NRC (Canada), NSC, and ASIAA (Taiwan), and KASI (Republic of Korea), in cooperation with the Republic of Chile. The Joint ALMA Observatory is operated by ESO, AUI/NRAO, and NAOJ. This work was also based on observations carried out with the IRAM 30-meter telescope. IRAM is supported by INSU/CNRS (France), MPG (Germany), and IGN (Spain).

\*\* Full Table A.6 is only available at the CDS via anonymous ftp to [cdsarc.u-strasbg.fr](http://cdsarc.u-strasbg.fr) (130.79.128.5) or via <http://cdsarc.u-strasbg.fr/viz-bin/qcat?J/A+A/587/L4>

such as comets, asteroids, and the Earth. Comets are considered to be a repository of information on their frozen surface of the gas and dust composition of the primitive solar nebula. As they approach the Sun in their journey their surface ices start to evaporate and to create a coma of gas and dust that has been extensively studied at all wavelengths (Bockelée-Morvan et al. 2000; Crovisier 2006; Mumma & Charnley 2011). A good correlation has been found between the type of molecules detected in the coma of comets and those of warm molecular clouds (Bockelée-Morvan et al. 2000; Biver et al. 2015).

The Cometary Sampling and Composition (COSAC) experiment aboard Rosetta's Philae lander has measured in situ abundances of the main components of the surface of comet 67P/Churyumov-Gerasimenko (Goesmann et al. 2015). Most of the “gas on the rocks” species assigned by COSAC are well-known interstellar molecules. However, many of the species detected by COSAC have not been observed in the coma of previously observed comets (Goesmann et al. 2015), while some organic molecules observed in the coma of comets are not detected by COSAC. Nevertheless, the coma organics can be formed by UV irradiation of the ices forming alcohols and

carbonyls from CO and H<sub>2</sub>O ices (Muñoz Caro & Dartois 2013). Among the organic molecules detected on the surface of the comet, only one was not detected in space, methyl isocyanate (CH<sub>3</sub>NCO), which could potentially contribute to the mass peak  $m/z = 57$  of COSAC. Although it is a molecule of potential relevance, to our knowledge it has not been included in any astrochemical network, and to date its detection has only been reported towards Sgr B2 based on a reduced number of lines (Halfen et al. 2015), whereas on 67P/Churyumov-Gerasimenko it was identified as one of the most abundant molecules after water (Goesmann et al. 2015). The most promising interstellar clouds in which to search for CH<sub>3</sub>NCO are hot cores and hot corinos.

In 2006 we started a sensitive line survey in the millimetre domain (80–280 GHz) of Orion using the IRAM 30 m radio telescope (Tercero et al. 2010) with the goal of fully characterizing its chemical composition (see Appendix B). However, owing to the high kinetic temperature of the gas,  $T_K \approx 100$ –300 K, many rotational and vibrational levels of abundant species are populated, producing a forest of spectral lines. Around 15000 spectral features were initially detected of which 8000 were unassigned. A systematic work programme in spectroscopic laboratories was started, which allowed us to significantly reduce the number of unidentified lines and to detect new molecules such as NH<sub>3</sub>D<sup>+</sup> (Cernicharo et al. 2013; Domenech et al. 2013), CH<sub>3</sub>COOCH<sub>3</sub> (Tercero et al. 2013), and CH<sub>3</sub>OCH<sub>2</sub>CH<sub>3</sub> (Tercero et al. 2015).

In this Letter we report on the complete laboratory spectroscopic characterization of CH<sub>3</sub>NCO and the detection of 399 of its lines in Orion. We also discuss the spectroscopic data used by Halfen et al. (2015) and comment on their column density estimations towards Sgr B2.

## 2. Spectroscopy

CH<sub>3</sub>NCO was initially searched for in our Orion data by using the available sub-40 GHz microwave spectroscopic work for this species (Koput 1986). However, irrespective of the usual problems of extrapolation outside the data region, we faced additional problems affecting the rotational spectrum of this molecule (see Fig. 1). Koput complemented his thorough experimental investigation of the 8–40 GHz region by Stark spectroscopy with analysis based on fitting a five-dimensional, quasi-symmetric top Hamiltonian. He was unable to fit the measured transition frequencies to experimental accuracy, but he reached unambiguous assignment of rotational transitions in many internal rotation substates of the ground and the two lowest excited states of the CNC bending vibrational mode (Koput 1986). The very low effective barrier to internal rotation,  $V_3 = 21 \text{ cm}^{-1}$ , was found to result in a series of low-lying internal rotor states, with the distribution close to that of the free rotor pattern, and estimated energies relative to the  $m = 0$  ground state of  $8.4 \text{ cm}^{-1}$  for the  $m = 1$  substate,  $36.8 \text{ cm}^{-1}$  for  $m = 2$ ,  $79.7$  and  $80.3 \text{ cm}^{-1}$  for the two nearly degenerate  $m = 3$  substates, and  $140.6 \text{ cm}^{-1}$  for  $m = 4$ . The next higher vibrational state was found to be the first excited state of the CNC bending mode,  $v_b = 1$  at  $182.2 \text{ cm}^{-1}$ . That state, in turn, carries its own stack of internal rotor states, and so on. The resulting high state density and considerable vibration-rotation coupling are the main reason why the laboratory understanding of the rotational spectrum of this molecule has been considerably delayed.

In order to derive a reliable CH<sub>3</sub>NCO line list for astrophysical applications we decided to cut through these problems by using the procedure described in detail in Appendix A and already discussed in two progress reports (Kisiel et al. 2010, 2015). The complete experimental spectrum in the region 40–363 GHz was

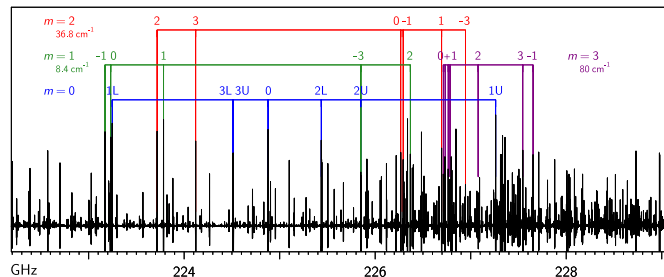


**Fig. 1.** Room-temperature rotational spectrum of CH<sub>3</sub>NCO in the  $J=26$ –25 transition region. The spectrum is devoid of features that normally aid assignment, such as identifiable progressions of transitions in rotational or vibrational quantum numbers. The visible complexity is due to the presence of nearly free internal rotation of the methyl group (described by the quantum number  $m$ ) and the low-frequency CNC bending motion. Vibrational energies of the lowest  $m$  states relative to the ground state ( $m = 0$ ) and the  $K$  assignment are indicated. The high density of states leads to perturbations in frequencies of many transitions, such as the considerable shift to low frequency of the ground state  $K = 3$  lines.

measured and was first broken down into over 220 correlated line sequences. The assignment reached by Koput (1986), was then transferred to the sequences extending over the entire covered frequency range. As a result, we derived a line list for the most relevant rotational transition sequences for CH<sub>3</sub>NCO consisting almost entirely of experimental frequencies and free from any extrapolation (see Appendix A).

Our extensive spectroscopic coverage allows line-by-line comparison (see Table A.7) with the newly reported spectroscopic data in Halfen et al. (2015), where the Koput sub-40 GHz data is extended by 21 laboratory measurements in the region 60–87.5 GHz. We find good agreement between our data and the Halfen et al. (2015) data for 13 out of the 21 reported lines, and this includes the  $K_a = 0, 1$ ,  $m = 0$  lines crucial to the Sgr B2(N) detection in their work. At the same time we note that seven lines show intriguing frequency differences of very close to 1 MHz between these two data sets. There is also a discrepancy in assignment concerning the line at 77 107.478 MHz, which according to our analysis is  $K = -2$ ,  $m = 2$  and not  $K = +1$ ,  $m = 1$ , and its upper level is 91 K and not 44 K. This limited agreement suggests that extrapolations made in Halfen et al. (2015) may be rather uncertain. The worst case is provided by the predicted line at 102 829.29 MHz searched for in Halfen et al. (2015), since it turns out that there is no line in the laboratory spectrum within  $\pm 10$  MHz. Our comprehensive study of the laboratory spectrum of CH<sub>3</sub>NCO showed that, even with self-consistent data, multi  $m$ -state fitting of this spectrum to experimental accuracy, and thus reliable predictions, are not yet possible. We emphasize again that the line list of 1269 lines up to 362 GHz that we report in Appendix A covers the frequency region relevant to astrophysical searches by means of actual laboratory measured frequencies.

## 3. Results

Once the key transitions of CH<sub>3</sub>NCO were assigned in the laboratory, we used the resulting line list to search for this species in Orion KL. Of the 521 lines of CH<sub>3</sub>NCO expected in the frequency coverage of the IRAM 30 m data (80–280 GHz), 236 are found to be unblended with other features, and 163 are partially blended but still identifiable in the combined line profiles with the contaminating lines. The remaining 122 lines are completely

blended with strong features of one or more of the most abundant species, most of them above 200 GHz where the line density in Orion becomes very considerable. None of the unblended or partially blended features is missing. Figure 2 shows a selected number of lines from our line survey and from the ALMA Science Verification (SV) data of Orion (see also Fig. B.1 which shows all 399 detected lines). The ALMA data between 213.7 and 246.7 GHz mitigates line blending owing to the high spatial resolution that distinguishes between the contributions from the different hot cores of Orion. Hence, many features that are fully contaminated in the IRAM data do appear clearly in the ALMA observations. The dipole moment of  $\text{CH}_3\text{NCO}$  is high, 2.88 D (Kasten & Dreizler 1986), but its partition function at 150 K is also very high ( $\approx 3.0 \times 10^4$ , see Appendix A). As a result the lines appear weaker than for species with similar abundances and dipole moments. Nevertheless, the current detection of  $\text{CH}_3\text{NCO}$  in space is based on the largest data set of convincingly assigned lines for a previously unobserved molecule. Moreover, the assigned lines correspond to the strongest unidentified features we have in our data. In the 30 m and ALMA SV data the lines are strikingly prominent (see Figs. 2 and B.1).

In order to derive the relative abundance of  $\text{CH}_3\text{NCO}$  with respect to other organic molecules found in the comet, we used the MADEX code (Cernicharo 2012) to model all the lines that we detected with the IRAM 30 m radio telescope and the ALMA interferometer. The spatial distribution of these species, as observed with the ALMA data, together with that of  $\text{CH}_3\text{NCO}$ , is shown in Figs. 3 and B.3. At first glance the spatial distribution of  $\text{CH}_3\text{NCO}$  looks similar to that of the other species with two emission peaks, A and B symmetrically placed with respect to source  $n$ . However, a detailed inspection of these figures shows significant differences in the extent of their spatial distribution and in the position of the maxima. The most similar spatial distributions are those of  $\text{CH}_3\text{NCO}$ ,  $\text{HNCO}$ ,  $\text{NH}_2\text{CHO}$ , and  $\text{CH}_3\text{CN}$ . The species HDO, which traces water vapour, also shows A and B cores and is used to derive relative abundances with respect to  $\text{H}_2\text{O}$  (see Appendix B). The remaining molecules have their emission peaks at different positions and with a different spatial extent (see Appendix B). Similar discrepancies in the spatial distribution of other molecular species in Orion have been reported (see Appendix B). Spatial correlation between species with similar chemical routes could help in assessing this new detection. In Appendix B we discuss various aspects regarding the complexity of this source and, in addition, very little is known about the formation routes of  $\text{CH}_3\text{NCO}$  so the suspicion that this species could be related to  $\text{HNCO}$  or  $\text{NH}_2\text{CHO}$  is still very tentative. The main support that the maps provide for the detection is the correlation between the two  $\text{CH}_3\text{NCO}$  maps that depict the distribution of the molecule for two different internal rotation states ( $m=0$  and  $m=1$ ; see Figs. 3 and B.3), which shows that the lines arise cospatially removing the possibility of their origin from different species. In Appendix B we discuss the spatial distribution of the species shown in Figs. 3 and B.3.

Because of the different angular resolution of our data, two sets of models (the methods are described in Appendix B) have been run in order to fit the molecular emission of all these species. We used one model for the single-dish data, which provides a convolved view of the source structure with the angular resolution of the 30m telescope that ranges from  $10''$  to  $27''$ , and a different model for the ALMA data, which have an angular resolution of  $1''.8 \times 1''.8$  (see Appendix B). The methyl isocyanate lines are reasonably well fitted with a kinetic temperature of 150 K. The column densities obtained from the ALMA data are given in Table B.1, which also reproduces

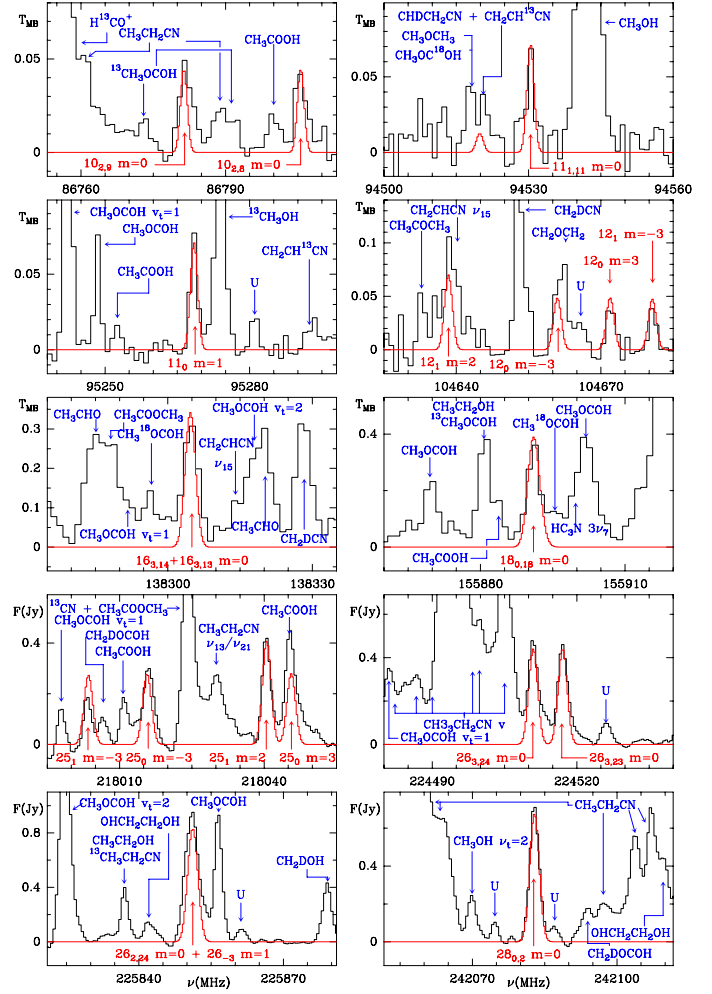


**Fig. 2.** Selected lines of  $\text{CH}_3\text{NCO}$  as observed with the IRAM 30 m radio telescope (toward the IRc2 source at  $\alpha_{2000.0} = 5^{\text{h}}35^{\text{m}}14^{\text{s}}.5$ ,  $\delta_{2000.0} = -5^{\circ}22'30''$ ,  $0.5''$  north to source  $I$ , see Fig. 3) and the ALMA interferometer (Position A, see Fig. 3). The red lines show the model of  $\text{CH}_3\text{NCO}$  emission discussed in the text. Red labels show the quantum numbers of the corresponding lines. Blue labels show the species responsible for the other features observed in each panel. The complete set of detected lines of  $\text{CH}_3\text{NCO}$  is shown in Fig. B.1. The intensity units for the last four panels (ALMA data) are in Jy/beam. They can be transformed into brightness temperature,  $T_{\text{B}}$ , by multiplying the intensities by a factor of 9. The intensity scale for the 30 m IRAM telescope is the main-beam antenna temperature in K.

the relative abundances of the species found by COSAC. The CO abundance in the comet was poorly determined by COSAC (Goesmann et al. 2015) and we have referred all abundances to  $\text{H}_2\text{O}$  as in the COSAC results. Table B.1 shows that  $\text{CH}_3\text{NCO}$  in the Orion clouds is 400, 15, 10, and 5 times less abundant than  $\text{CH}_3\text{OH}$ ,  $\text{HNCO}$ ,  $\text{CH}_3\text{CN}$ , and  $\text{CH}_3\text{CH}_2\text{CN}$ , respectively. However,  $\text{CH}_3\text{NCO}$  is more abundant than amines, aldehydes, and acetones.

#### 4. Discussion

We attempted to detect two isomers of  $\text{CH}_3\text{NCO}$ :  $\text{CH}_3\text{CNO}$  (acetonitrile oxide) and  $\text{CH}_3\text{OCN}$  (methyl cyanate). The energy difference of these isomers relative to the most stable one ( $\text{CH}_3\text{NCO}$ ) is  $8785 \text{ cm}^{-1}$  ( $25.1 \text{ kcal mol}^{-1}$ ) for  $\text{CH}_3\text{OCN}$  and  $20090 \text{ cm}^{-1}$  ( $57.4 \text{ kcal mol}^{-1}$ ) for  $\text{CH}_3\text{CNO}$

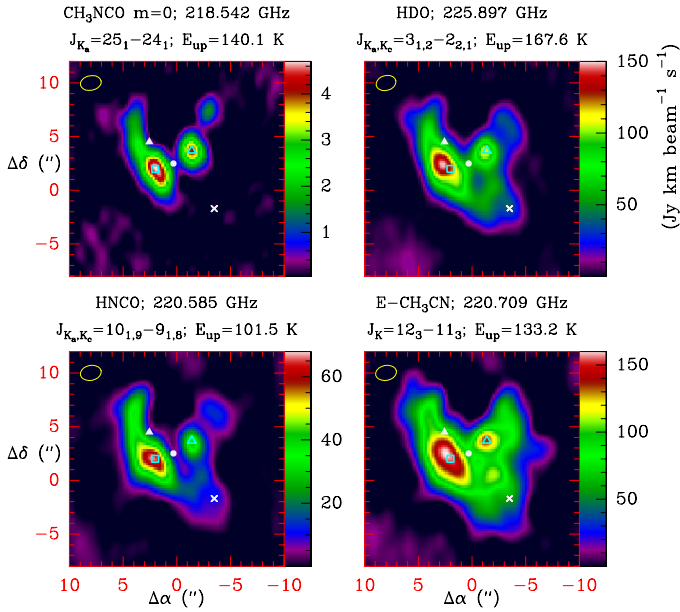


**Fig. 3.** Spatial distribution of CH<sub>3</sub>NCO (*top left panel*) together with those of several molecular species as identified at the top of each panel. The data are from ALMA Science Verification observations. The different positions discussed in the text are indicated by symbols (white triangle: source *I*; white circle: source *n*; ×: the compact ridge; cyan unfilled square/triangle: Positions A/B, which are the two emission peaks of CH<sub>3</sub>NCO). Additional molecular emission maps are shown in Fig. B.3.

(Pasinazki & Westwood 2001). CH<sub>3</sub>CNO has been characterized in the laboratory at millimetre wavelengths (Winnewisser et al. 1982). We derive an upper limit for its column density in Orion of  $\leq 6 \times 10^{13} \text{ cm}^{-2}$ , i.e., a factor of  $\approx 100$  below that for CH<sub>3</sub>NCO (see Table B.1). The experimental rotational spectra of methyl cyanate were recorded recently in the millimetre wave domain from 130 to 350 GHz and more than 300 internal rotation A-E doublets were successfully analysed (Kolesniková et al., in prep.). From the predicted spectrum we also derive an upper limit to its column density of  $\leq 1 \times 10^{14} \text{ cm}^{-2}$ . Hence, only the most stable isomer, CH<sub>3</sub>NCO, seems to be present in Orion. Tercero et al. (2013) found a negative detection of three isomers of methyl acetate and ethyl formate in Orion KL. López et al. (2014) also found upper limits to the abundance of the isocyanide isomers of ethyl and vinyl cyanide. A large discussion of the importance of bonding energy differences in the abundances of interstellar isomers was provided by Remijan et al. (2005). López et al. (in prep.) address the detection and abundances of two isomers of methyl formate in Orion KL.

We have searched for CH<sub>3</sub>NCO toward a cold prestellar core, B1-b, in which a large variety of complex organic molecules, some of them typical of hot cores, have been found: CH<sub>3</sub>O, CH<sub>3</sub>OCOH, CH<sub>3</sub>OCH<sub>3</sub>, CH<sub>3</sub>CHO, and CH<sub>3</sub>SH. The abundances of these species relative to H<sub>2</sub>,  $X \approx 10^{-11}$  (Cernicharo et al. 2012), are much lower in B1-b than in Orion. Using the data from Cernicharo et al. (2012) we have obtained an upper limit for the column density of CH<sub>3</sub>NCO in B1-b of  $\leq 2 \times 10^{11} \text{ cm}^{-2}$  ( $X \leq 2 \times 10^{-12}$ ).

CH<sub>3</sub>NCO has also been found towards Sgr B2 by Halfen et al. (2015). They derive a rather low rotational temperature,  $T_{\text{rot}} \approx 24 \text{ K}$ . However, we have searched for CH<sub>3</sub>NCO in other public line surveys of Sgr B2 (Belloche et al. 2013) and found clear identification of methyl isocyanate in the warm gas of Sgr B2, with  $T_K \approx 200 \text{ K}$  and  $N(\text{CH}_3\text{NCO}) = 5 \times 10^{17} \text{ cm}^{-2}$

for the  $63 \text{ km s}^{-1}$  component and  $3 \times 10^{17} \text{ cm}^{-2}$  for the second component at  $73 \text{ km s}^{-1}$  (see Appendix B). Using our laboratory frequencies, partition function and energy of the levels we have been able to identify 76 lines (43 unblended and 33 partially blended) in the 3 mm Sgr B2(N) data of Belloche et al. (2013). Several lines claimed missing in Halfen et al. (2015) are in fact well detected, but at  $\approx 10 \text{ MHz}$  from the predictions they use (see Fig. B.2). Most of the lines shown in Fig. B.2 have not been detected by Halfen et al. (2015) since they correspond to CH<sub>3</sub>NCO transitions with  $K \geq 2$  and/or  $m \geq 2$ . Assuming the column densities derived by Belloche et al. (2013) for the hot component at 200 K and  $v_{\text{LSR}} \approx 63 \text{ km s}^{-1}$ , we derive  $N(\text{CH}_3\text{OH})/N(\text{CH}_3\text{NCO}) \approx 40$ ,  $N(\text{HNCO})/N(\text{CH}_3\text{NCO}) \approx 40$ , and  $N(\text{CH}_3\text{CN})/N(\text{CH}_3\text{NCO}) \approx 50$ , which are different from the values we derived for Orion KL (see Table B.1): 400, 15, 10, and 225, 15, 25, in Positions A and B, respectively. The measured difference in the abundance ratio between the two regions again points to a combination of physical and chemical differences based on the evolutionary states of the clouds found in the Galactic centre and outer disk of the Galaxy.

Nothing is known about the formation of methyl isocyanate in the gas phase or on the surface of the grains in molecular clouds. Some gas phase reactions that could form CH<sub>3</sub>NCO have been discussed by Halfen et al. (2015). However, the high abundance for this species presently found in Orion and Sgr B2, together with the fact that it is detected in hot cores and not in cold dark clouds, also point towards a chemistry conducted in the grain mantles. Dedicated laboratory experiments on ices have to be performed in order to learn about the formation processes of CH<sub>3</sub>NCO. In the ices CH<sub>3</sub>NCO could be formed by methylation of HNCO (Goesmann et al. 2015). It is well known that at ambient temperature methyl isocyanate reacts with many substances that contain N–H or O–H groups and with water, which are common in the gas phase of Orion. Hence, the observed differences in molecular abundances between the gas phase and in the comet ice, if the comet surface still keeps pristine dust grains, imply a very rich chemistry in the gas phase for the molecules escaping the ices. Molecular abundances in Orion could result from the chemical history of the ejected material from the grains. It will be of great interest to observe the coma of the comet in order to obtain the abundances of the gas phase species and information on how the COSAC identified molecules survive ejection from the comet surface.

*Acknowledgements.* The Spanish authors thank MINECO for funding support from the CONSOLIDER-Ingenio program “ASTROMOL” CSD 2009-00038, AYA2012-32032, CTQ 2013-40717 P, CTQ 2010-19008, and the ERC synergy grant ERC-2013-Syg-610256-NANOCOSMOS. They also thank Junta de Castilla y León under grants VA070A08 and VA175U13. Z.K. acknowledges a grant from the Polish National Science Centre, decision number DEC/2011/02/A/ST2/00298. J.-C.G. and J.C. thank the ANR-13-BS05-0008-02 IMOLABS. J.-C.G. thanks the Program PCMI (INSU-CNRS) and the Centre National d’Études Spatiales (CNES) for funding support. The OSU authors acknowledge funding from NASA, NSF, and the Army Research Office.

## References

- Alonso, J. L., Lorenzo, F. J., López, J. C., et al. 1997, *Chem. Phys.*, **218**, 267  
 Alonso, E. R., Kolesniková, L., Peña, I., et al. 2015, *J. Mol. Spectr.*, **316**, 84  
 Becklin, E. E., & Neugebauer, G. 1967, *ApJ*, **147**, 799  
 Bell, T., Cernicharo, J., Viti, S., et al. 2014, *A&A*, **218**, 72  
 Belloche, A., Müller, H. P. S., Menten, K. M., et al. 2013, *A&A*, **559**, A47  
 Bermúdez, C., Mata, S., Cabezas, C., & Alonso, J. L. 2014, *Angew. Chem. Int. Ed.*, **53**, 11015  
 Biver, N., Bockelée-Morvan, D., Moreno, R., et al. 2015, *Sci. Adv.*, **1**, 0863  
 Blake, G. A., Sutton, E. C., Masson, C. R., & Phillips, T. G. 1987, *ApJ*, **315**, 621  
 Bockelée-Morvan, D., Lis, D. C., Winket, J. E., et al. 2000, *A&A*, **353**, 1101

- Brändström, A., Lamm, B., & Palmert, I. 1974, *Acta Chem. Scand. B.*, **28**, 699
- Brouillet, N., Despois, D., Lu, X.-H., et al. 2015, *A&A*, **576**, A129
- Brown, G. G., Dian, B. C., Douglass, K. O., et al. 2008, *Rev. Sci. Instr.*, **79**, 053103
- Carvajal, M., Margulès, L., Tercero, B., et al. 2009, *A&A*, **500**, 1109
- Cernicharo, J. 1985, Internal IRAM report (Granada: IRAM)
- Cernicharo, J. 2012, in ECLA-2011: Proc. European Conference on Laboratory Astrophysics, eds. C. Stehl, C. Joblin, & L. d'Hendecourt (Cambridge: Cambridge Univ. Press), *EAS Pub. Ser.*, **58**, 251
- Cernicharo, J., Marcelino, N., Roueff, E., et al. 2012, *ApJ*, **759**, L43
- Cernicharo, J., Tercero, B., Fuente, A., et al. 2013, *ApJ*, **771**, L10
- Coudert, L. H., Drouin, B. J., Tercero, B., et al. 2013, *ApJ*, **779**, 119
- Crovisier, J. 2006, in Asteroids, Comets, Meteors, Proc. 229th IAU Symp., eds. D. Lazzaro, S. Ferraz Mello, & J. L. Fernández (Cambridge Univ. Press), 133
- Curl, R. F., Rao, V. M., Sastry, K. V. L. N., & Hodgeson, J. A. 1963, *J. Chem. Phys.*, **39**, 3335
- Daly, A. M., Bermúdez, C., López, A., et al. 2013, *ApJ*, **768**, 81
- Daly, A. M., Kolesníková, L., Mata, S., & Alonso, J. L. 2014, *J. Mol. Spectr.*, **306**, 11
- Daly, A. M., Bermúdez, C., Kolesníková, L., & Alonso, J. L. 2015, *ApJS*, **218**, 30
- Demyk, K., Mäder, H., Tercero, B., et al. 2007, *A&A*, **466**, 255
- Domenech, J. L., Cueto, M., Herrero, V. J., et al. 2013, *ApJ*, **771**, L11
- Esplugues, G. B., Tercero, B., Cernicharo, J., et al. 2013a, *A&A*, **556**, A143
- Esplugues, G. B., Cernicharo, J., Viti, S., et al. 2013b, *A&A*, **559**, A51
- Favre, C., Wootten, H. A., Remijan, A. J., et al. 2011, *ApJ*, **739**, L12
- Feng, S. Y., Beuther, H., Henning, T., et al. 2015, *A&A*, **581**, A71
- Fortman, S. M., McMillan, J. P., Neese, C. F., et al. 2012, *J. Mol. Spectr.*, **280**, 11
- Friedel, D. N., & Widicus Weaver, S. L. 2012, *ApJS*, **201**, 17
- Genzel, R., & Stutzki, J. 1989, *ARA&A*, **27**, 41
- Gezari, D. Y., Backman, D. E., & Werner, M. W. 1998, *ApJ*, **509**, 283
- Goesmann, F., Rosenbauer, H., Hendrik Bredehöft, J., et al. 2015, *Science*, **6247**, 349
- Goicoechea, J. R., Chavarría, L., Cernicharo, J., et al. 2015, *ApJ*, **799**, 102
- Gómez, L., Rodríguez, L. F., Loinard, L., et al. 2005, *ApJ*, **635**, 1166
- Grabow, J. U., Stahl, W., & Dreizler, H. 1996, *Rev. Sci. Instr.*, **67**, 4072
- Guélin, M., Brouillet, N., Cernicharo, J., Combes, F., & Wooten, A. 2008, *Ap&SS*, **313**, 45
- Halfen, D. T., Ilyushin, V. V., & Ziurys, L. 2015, *ApJ*, **812**, L5
- Haykal, I., Margulès, L., Huet, T. R., et al. 2013, *ApJ*, **777**, 120
- Haykal, I., Carvajal, M., Tercero, B., et al. 2014, *A&A*, **568**, A58
- Herbst, E., & van Dishoeck, E. 2009, *ARA&A*, **47**, 427
- Kisiel, Z. 2001a, in Spectroscopy from Space, eds. J. Demaison et al. (Dordrecht: Kluwer Academic Publishers), 91
- Kisiel, Z. 2001b, PROSPE Programs for ROTational SPectroscopy, [www.ifpan.edu.pl/~kisiel/prospe.htm](http://www.ifpan.edu.pl/~kisiel/prospe.htm)
- Kisiel, Z., Pszczółkowski, L., Medvedev, I. R., et al. 2005, *J. Mol. Spectr.*, **233**, 231
- Kisiel, Z., Fortman, S., Medvedev, I. R., et al. 2010, in 65th Int. Symp. Molecular Spectroscopy, Columbus, Ohio, June 21–25, RC18, [https://molspect.chemistry.ohio-state.edu/symposium\\_65/symposium/Abstracts/p272.pdf](https://molspect.chemistry.ohio-state.edu/symposium_65/symposium/Abstracts/p272.pdf)
- Kisiel, Z., Pszczółkowski, L., Drouin, B. J., et al. 2012, *J. Mol. Spectr.*, **280**, 134
- Kisiel, Z., Kolesníková, L., Alonso, J. L., et al. 2015, 70th Int. Symp. on Molecular Spectroscopy, Champaign-Urbana, Illinois, June 22–26, TG08, [http://isms.illinois.edu/2015/schedule/abstract\\_files/1046.pdf](http://isms.illinois.edu/2015/schedule/abstract_files/1046.pdf)
- Kleinmann, D. E., & Low, F. J. 1967, *ApJ*, **149**, L1
- Kolesníková, L., Daly, A. M., Alonso, J. L., Tercero, B., & Cernicharo, J. 2013, *J. Mol. Spectr.*, **289**, 13
- Kolesníková, L., Tercero, B., Cernicharo, J., et al. 2014, *ApJ*, **784**, L7
- Kolesníková, L., Peña, I., Alonso, J. L., et al. 2015, *577*, A91
- Koput, J. 1984, *J. Mol. Spectr.*, **106**, 12
- Koput, J. 1986, *J. Mol. Spectr.*, **115**, 131
- Koput, J. 1988, *J. Mol. Spectr.*, **127**, 51
- Kasten, W., & Dreizler, H. 1986, *Z. Naturforsch.*, **41a**, 637
- Lett, R. G., & Flygare, W. H. 1967, *J. Chem. Phys.*, **47**, 4730
- López, A., Tercero, B., Kisiel, Z., et al. 2014, *A&A*, **572**, A44
- Marcelino, N., Cernicharo, J., Tercero, B., & Roueff, E. 2009, *ApJ*, **690**, L27
- Margulès, L., Motiyenko, R. A., Demyk, K., et al. 2009, *A&A*, **493**, 565
- Margulès, L., Huet, T. R., Demaison, J., et al. 2010, *ApJ*, **714**, 1120
- Mata, S., Peña, I., Cabezas, C., et al. 2012, *J. Mol. Spectr.*, **280**, 91
- Medvedev, I., Winnewisser, M., De Lucia, F. C., et al. 2004, *J. Mol. Spectr.*, **228**, 314
- Menten, K. M., & Reid, M. J. 1995, *ApJ*, **445**, L157
- Menten, K. M., Reid, M. J., Forbrich, J., & Brunthaler, A. 2007, *A&A*, **474**, 515
- Motiyenko, R. A., Tercero, B., Cernicharo, J., & Margulès, L. 2012, *A&A*, **548**, A71
- Mumma, M. J., & Charnley, S. B. 2011, *ARA&A*, **49**, 471
- Muñoz Caro, G. M., & Dartois, E. 2013, *Chem. Soc. Rev.*, **42**, 2173
- Neill, J. L., Muckle, M. T., Zaleski, D. P., et al. 2012, *ApJ*, **755**, 153
- Neill, J., Crockett, N. R., Bergin, E. A., et al. 2013, *ApJ*, **777**, 85
- O'Dell, C. R. 2001, *ARA&A*, **39**, 99
- Pardo, J. R., Cernicharo, J., Serabyn, E. 2001, *IEEE Trans. Antennas and Propagation*, **49**, 12
- Pasinszki, T., & Westwood, N. P. C. 2001, *J. Phys. Chem. A*, **105**, 1244
- Peng, T.-C., Despois, D., Brouillet, N., Parise, B., & Baudry, A. 2012, *A&A*, **543**, A152
- Peng, T.-C., Despois, D., Brouillet, N., et al. 2013, *A&A*, **554**, A78
- Petkie, D. T., Goyette, T. M., Bettens, R. P. A., et al. 1997, *Rev. Sci. Instr.*, **68**, 1675
- Pickett, H. M. 1991, *J. Mol. Spectr.*, **148**, 371, SPFIT/SPCAT, <http://spec.jpl.nasa.gov>
- Pickett, H. M., Poynter, R. L., Cohenet, E. A., et al. 1998, *J. Quant. Spectr. Rad. Transf.*, **60**, 883
- Pulliam, R. L., McGuire, B. A., & Remijan, A. J. 2012, *ApJ*, **751**, 1
- Remijan, A. J., Hollis, J. M., Lovas, F. J., Plusquellic, D. F., & Jewell, P. R. 2005, *ApJ*, **632**, 333
- Rodríguez, L. F., Zapata, L. A., & Ho, P. T. P. 2009, *ApJ*, **692**, 162
- Schilke, P., Benford, D. J., Hunter, T. R., et al. 2001, *ApJSS*, **132**, 281
- Shuping, R. Y., Morris, M., & Bally, A. 2004, *ApJ*, **128**, 363
- Tercero, B., Cernicharo, J., Pardo, J. R., & Goicoechea, J. R. 2010, *A&A*, **517**, A96
- Tercero, B., Vincent, L., Cernicharo, J., Viti, S., & Marcelino, N. 2011, *A&A*, **528**, A26
- Tercero, B., Margulès, L., Carvajal, M., et al. 2012, *A&A*, **538**, A119
- Tercero, B., Kleiner, I., Cernicharo, J., et al. 2013, *ApJ*, **770**, L13
- Tercero, B., Cernicharo, J., López, A., et al. 2015, *A&A*, **582**, L1
- Watson, J. K. G. 1997, in Vibrational Spectra and Structure, ed. J. R. Durig, (New York/Amsterdam: Elsevier), 6, 1
- Widicus Weaver, S. L., & Friedel, C. N. 2012, *ApJS*, **201**, 16
- Winnewisser, M., Pearson, E. F., Galica, J., & Winnewisser, B. P. 1982, *J. Mol. Spectr.*, **91**, 255
- Winnewisser, B. P., Reinstädler, J., Yamada, K. M. T., & Behrend, J. 1989, *J. Mol. Spectr.*, **136**, 12
- Wynn-Williams, C. G., Genzel, R., Becklin, E. E., & Downes, D. 1984, *ApJ*, **281**, 172
- Wu, Y., Liu, T., & Qin, S.-L. 2014, *ApJ*, **791**, 123
- Zapata, L. A., Schmid-Burgk, J., & Menten, K. M. 2011, *A&A*, **529**, A24

## Appendix A: Spectroscopy of CH<sub>3</sub>NCO

Thorough analysis of the rotational spectrum of a target molecule is a crucial step that enables astrophysical detection. In the case of CH<sub>3</sub>NCO the understanding of the rotational spectrum, and thus delivery of suitable line lists for astrophysical use has been considerably delayed by the complications arising from the presence of two large amplitude internal motions in this molecule. The first laboratory studies were carried out around half a century ago (Curl et al. 1963; Lett et al. 1967) when it was found that the molecule has a very low barrier to internal rotation of the methyl group and also a low-frequency bending mode. In the 1980s those studies were greatly extended by Koput (1984, 1986, 1988). His use of Stark spectroscopy allowed the unambiguous assignment of transitions for different values of  $K$ . The use of a semi-rigid rotor Hamiltonian and relative intensity considerations allowed the assignment of the vibrational quantum numbers  $m$  and  $v_b$ . In this way a very self-consistent picture of the complex vibrational energy structure was reached, as already described in connection with Fig. 1. In an investigation contemporary with that of Koput, the electric dipole moment of CH<sub>3</sub>NCO was also precisely determined:  $\mu_a = 2.882(8)$  D (Kasten & Dreizler 1986).

Further progress in the investigation of the rotational spectrum of methyl isocyanate was achieved as part of this work. In a first stage a practically continuous 117–364 GHz of the molecule was recorded by means of the Fast Scanning Submillimeter Spectroscopic Technique (FASSST) developed at The Ohio State University (Petkie et al. 1997; Medvedev et al. 2004). The spectrum was recorded at room-temperature using a commercially available sample. Although the Koput (1986) analysis was very successful in accounting for the consequences of the large amplitude motions on the rotational spectrum of this molecule, the deviation of the fit to 210 transitions up to  $J = 4 \leftarrow 3$  was 3 MHz, which was well in excess of the 0.05 MHz frequency measurement precision of his spectrometer. Furthermore, even a cursory inspection of the FASSST spectrum (see Fig. 1) revealed that it was devoid of easily discernible spectral patterns and that progress in its traditional interpretation would be difficult. We have, therefore, decided to pursue a pragmatic approach to the characterization of this spectrum based on the generic property of rotational spectra, in that evolution of the frequencies of rotational transitions of a given set of quantum numbers can be described by a smooth function in the  $J$  quantum number. It was eventually possible to identify over 220 such line sequences and to fit each sequence to within experimental accuracy with a linear rotor-type model using a power series expansion in  $J(J+1)$ , as discussed in a preliminary report in 2010 (Kisiel et al. 2010). The separate line sequences were still without a confident  $K$ ,  $m$ , and  $v_b$  quantum number assignment. An initial attempt to transfer such assignments from the Koput work by linking sequences in the FASSST region with those below 40 GHz revealed many ambiguities, due to a still considerable region of missing experimental coverage of the rotational spectrum of CH<sub>3</sub>NCO.

For this reason, in a second stage of the laboratory part of the present work, the missing 40–117 GHz region of the spectrum was covered in Valladolid by using two complementary spectrometers. The 50–117 GHz segment of the spectrum was recorded with a harmonic generation spectrometer based on the multiplication of the synthesizer frequency of up to 20 GHz and employing source modulation detection (Daly et al. 2014). The  $J = 5 \leftarrow 4$  transition at 41–45 GHz was measured with a Stark modulation spectrometer (Daly et al. 2015) at a mod-

ulation voltage of 430 V. The sample was synthesized using the method described by Brändström et al. (1974) and in both spectrometers was kept at room temperature and a pressure of 20  $\mu$ bar. As a result of the combined effort from the participating laboratories we were able to achieve complete room temperature experimental coverage of the rotational spectrum of methyl isocyanate from the lowest  $J = 1 \leftarrow 0$  transition up to the  $J = 41 \leftarrow 40$  transition centred near 358 GHz. The analysis procedure first involved creating a single spectrum by combining all available experimental spectra. The intensities for the lines measured by Koput are not available so that the <40 GHz spectral segment was simulated by assuming equal intensity transitions at the reported frequencies. Measurements on this spectrum were then performed with the AABS package for Assignment and Analysis of Broadband Spectra (Kisiel et al. 2005, 2012), which is freely available from the PROSPE website (Kisiel 2001a,b). The fits and predictions were made with Pickett’s SPCAT/SPFIT program suite (Pickett 1991) and each line sequence required its own dedicated set of analysis files. In the case of explicit asymmetric rotor fits Watson’s  $A$ -reduced asymmetric rotor Hamiltonian (Watson 1977) was used. The Loomis-Wood type mode for displaying the rotational spectrum (as pioneered for rotational spectroscopy by Winniewisser et al. 1989 and built into the AABS package) was used for graphical assignment of transitions in specific line sequences. Some preliminary results were reported in the middle of last year (Kisiel et al. 2015) and Loomis-Wood plots for several sample transition sequences are reproduced in Fig. A.1. These plots allow the transfer of the Koput assignment to the higher frequency spectrum. We also consider the Koput assignment to be reliable since it was reached using variable voltage Stark modulation spectroscopy, which provides good discrimination between transitions with different values of  $K$  according to their different line profiles. Each of these identified line sequences is reproduced by a suitable  $J(J+1)$  power series expansion for the rotational energies

$$E_{\text{rot}} = BJ(J+1) - D_J J^2(J+1)^2 + H_J J^3(J+1)^3 \\ + L_J J^4(J+1)^4 + P_J J^5(J+1)^5 + P_{12} J^6(J+1)^6 \\ + P_{14} J^7(J+1)^7 + P_{16} J^8(J+1)^8 + P_{18} J^9(J+1)^9 \quad (\text{A.1})$$

where the length of the expansion and the magnitudes of the expansion parameters  $B$ ,  $D_J$ ,  $H_J$ , etc., are determined by the interactions and also by the asymmetry contributions affecting the energy levels in question. The required length of the expansion ranges from only three terms to being insufficient even if all nine terms in Eq. (A.1) are used. In several rare cases two power expansions were needed to model a line sequence with a particularly complex  $J$  dependence, by splitting the sequence into two parts. The results of such fits for the key assigned transition sequences used in the present astrophysical identifications are listed in Table A.1. In labelling the sequences we conform, as closely as possible, to the notation of Koput (1986) in order to ensure traceability. There are only two differences where the original notation was ambiguous and was modified. In the case of the ground state,  $v_b = 0$ ,  $m = 0$ , for which asymmetric rotor notation would normally be more appropriate, we modified Koput’s notation to  $K = 1L, 1U$ , etc., to distinguish between lower and upper frequency sequences for the same value of  $K_a$ . Similarly, we used the notation  $m = 3L$  and  $3U$  in order to distinguish between those of the two nearly degenerate  $m = 3$  sub-states which give rise to lower and upper frequency rotational transition sequences.

**Table A.1.** Parameters of the linear rotor-type,  $J(J + 1)$  power series fitted to the assigned line sequences.

$K_a$	Name <sup>b</sup>	$I_{rel}$ <sup>c</sup>	$N_{in}$ <sup>d</sup>	$N_{rej}$ <sup>e</sup>	$s^f$ (MHz)	$B^g$ (MHz)	$D_J$ (kHz)	$H_J$ (Hz)	$L_J$ (mHz)	$P_J$ ( $\mu$ Hz)	$P_{12}$ (nHz)	$P_{14}$ (pHz)	$P_{16}$ (fHz)	$P_{18}$ (aHz)
<b><math>v_b = 0, m = 0</math> (gs): <math>E_{vib} = 0 \text{ cm}^{-1}</math></b>														
0	V093:	0.885	41	1	0.046	4335.6996 (13)	8.4815 (43)	0.1971 (58)	0.0728 (33)	-0.00909 (69)				
1L	V126:	0.842	38	2	0.048	4297.6203 (10)	3.3744 (21)	0.1133 (16)	-0.00393 (41)					
1U	V131:	0.819	38	2	0.062	4376.1857 (14)	4.2752 (30)	-0.0053 (24)	0.00245 (67)					
2L	V089:	0.833	38	1	0.055	4339.69609 (82)	3.28715 (94)	0.03891 (31)						
2U	V006:	0.901	38	1	0.052	4339.6811 (16)	-2.8764 (56)	-0.1690 (77)	-0.0676 (47)	0.0079 (10)				
3L	V096:	0.727	35	4	0.063	4324.6816 (20)	5.1755 (65)	-0.2787 (86)	0.1698 (50)	-0.0156 (10)				
3U	V097:	0.726	35	4	0.054	4324.6762 (18)	5.1686 (55)	-0.1769 (74)	0.1479 (43)	-0.01455 (89)				
<b><math>v_b = 0, m = 1</math> E: <math>E_{vib} = 8.4 \text{ cm}^{-1}</math></b>														
0a	V107:	0.808	22	0	0.051	4357.5774 (71)	132.34 (14)	86.4 (14)	226.1 (67)	-665. (17)	719. (21)	-298. (11)		
0b	X107:	0.808	20	0	0.056	4348.7 (10)	116.2 (37)	146.2 (74)	-125.4 (87)	71.4 (65)	-25.9 (29)	5.39 (74)	-0.493 (81)	
-1	V101:	0.836	39	1	0.050	4282.7615 (32)	-3.118 (26)	9.39 (10)	-10.67 (19)	6.64 (21)	-2.59 (13)	0.590 (44)	-0.0593 (59)	
1	V098:	0.846	36	5	0.048	4284.5720 (42)	-35.940 (44)	-45.38 (21)	49.98 (57)	-45.27 (87)	29.62 (81)	-12.71 (44)	3.16 (12)	-0.342 (15)
-2	not assigned													
2	V010:	0.660	31	2	0.042	4350.3415 (23)	-2.325 (15)	-0.065 (46)	-0.290 (64)	0.284 (43)	-0.109 (11)			
-3	V005:	0.800	36	2	0.058	4343.3487 (25)	0.096 (11)	0.288 (25)	-0.381 (25)	0.202 (12)	-0.0848 (22)			
3	V012:	0.642	34	3	0.049	4356.1489 (11)	1.6845 (24)	-0.0204 (19)	0.00189 (52)					
<b><math>v_b = 0, m = -2</math> E: <math>E_{vib} = 36.8 \text{ cm}^{-1}</math></b>														
0	V119:	0.774	36	1	0.050	4356.2099 (29)	2.431 (15)	0.837 (33)	-2.676 (29)					
-1	V008:	0.708	38	2	0.062	4353.2529 (11)	1.0831 (14)	0.0	0.00928 (84)	-0.00378 (31)				
1	V180:	0.807	40	0	0.188	4350.771 (14)	-40.79 (16)	-39.36 (81)	-24.5 (22)	74.5 (34)	-69.5 (32)	34.7 (17)	-9.27 (54)	1.045 (69)
-2	not assigned													
2	V100:	0.805	39	0	0.084	4276.5950 (66)	-51.195 (68)	-64.24 (33)	63.79 (84)	-50.5 (12)	29.3 (11)	-11.35 (59)	2.60 (17)	-0.262 (20)
-3	V024:	0.473	35	3	0.055	4366.9265 (12)	1.9129 (27)	-0.0098 (22)	0.00672 (61)					
3a	V106:	0.523	21	0	0.043	4373.6038 (50)	110.306 (69)	93.71 (41)	-32.2 (12)	-11.7 (16)	10.81 (88)			
3b	X106:	0.884	18	0	0.052	4370.20 (59)	103.8 (16)	95.6 (24)	-55.9 (22)	20.9 (11)	-4.49 (32)	0.438 (38)		
<b><math>v_b = 0, m = 3L</math> (<math>K = 0, J = 0, 1 = A_1, A_2</math>): <math>E_{vib} = 80.3 \text{ cm}^{-1}</math></b>														
0	V017:	0.556	38	2	0.061	4361.0342 (19)	0.6664 (66)	0.0255 (94)	0.0843 (57)	-0.0269 (12)				
-1	V137:	0.654	37	2	0.093	4376.0833 (78)	-11.011 (83)	3.34 (41)	-25.5 (11)	21.8 (17)	-17.3 (16)	11.56 (91)	-4.15 (27)	0.576 (34)
1	V082:	0.485	39	0	0.070	4362.15134 (58)	1.68176 (26)							
-2	not assigned													
2	V030:	0.399	35	3	0.067	4369.5669 (10)	1.9458 (12)	-0.00228 (41)						
3	V040:	0.634	33	2	0.064	4378.65685 (60)	2.06406 (30)							
<b><math>v_b = 0, m = 3U</math> (<math>K = 0, J = 1, 0 = A_2, A_1</math>): <math>E_{vib} = 79.7 \text{ cm}^{-1}</math></b>														
0	V018:	0.540	39	2	0.046	4361.4499 (14)	0.5247 (49)	0.0221 (69)	0.0949 (42)	-0.02898 (93)				
1	V020:	0.491	36	3	0.044	4363.55034 (68)	1.72074 (80)	-0.00110 (27)						
-1	not assigned													
2	V029:	0.424	34	4	0.057	4369.57115 (94)	1.9779 (10)	0.00072 (36)						
-2	not assigned													
3	very strongly perturbed													
<b><math>v_b = 0, m = 4</math> E: <math>E_{vib} = 140.6 \text{ cm}^{-1}</math></b>														
0	V025:	0.416	37	3	0.052	4368.7341 (11)	1.5662 (25)	0.0039 (21)	0.00218 (57)					
<b><math>v_b = 0, m = -5</math> E: <math>E_{vib} = 217.5 \text{ cm}^{-1}</math></b>														
0	V142:	0.297	38	1	0.049	4377.7029 (11)	1.8930 (23)	-0.0136 (19)	0.00256 (51)					
<b><math>v_b = 1, m = 0</math> : <math>E_{vib} = 182.2 \text{ cm}^{-1}</math></b>														
0	V094:	0.391	41	0	0.050	4335.3010 (15)	7.8017 (47)	0.2011 (63)	0.0443 (37)	-0.00561 (76)				
1L	V127:	0.373	38	2	0.052	4297.1113 (11)	3.2544 (22)	0.0971 (17)	-0.00294 (44)					
1U	V132:	0.365	36	3	0.048	4377.6225 (11)	4.2356 (24)	0.0116 (19)	0.00223 (53)					

**Notes.** <sup>(a)</sup> The value of the  $K_a$  or  $K$  quantum number following, where possible, the notation of Koput (1986) and described further in the text following Eq. (A.1). <sup>(b)</sup> The identifier of the line sequence, identifiers Vnnn and Xnnn for the same “nnn” denote a two part sequence (Vnnn lower, Xnnn higher frequency part). <sup>(c)</sup> Intensity of the sequence relative to the strongest sequence in the spectrum. <sup>(d)</sup> The number of lines in the linear fit. <sup>(e)</sup> The number of confidently assigned lines that were perturbed and were rejected from the fit. <sup>(f)</sup> The standard deviation of the linear fit. <sup>(g)</sup> The values of the parameters required in the linear fit.

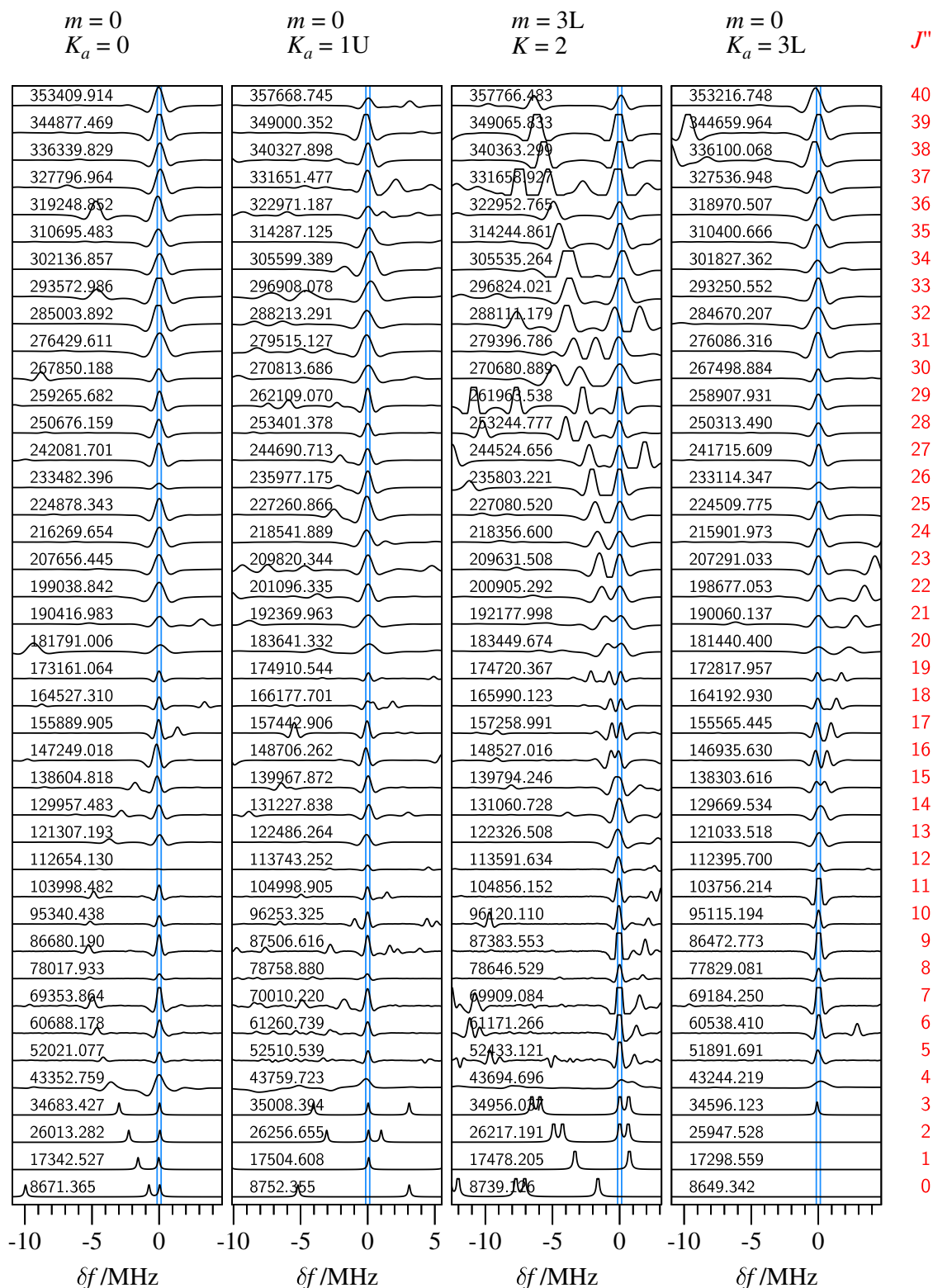


**Fig. A.1.** Sample Loomis-Wood type plots of the rotational spectrum of  $\text{CH}_3\text{NCO}$  for several assigned line sequences for  $\nu_b = 0$  where sections of the experimental spectrum are plotted around the indicated centre frequencies from the linear-type fits. The plots illustrate how the assignments reached with Stark spectroscopy at  $J'' \leq 3$  could be unambiguously transferred to the millimetre wave region. The blue lines mark the estimated frequency uncertainty.

The series fits and the Loomis-Wood displays were an invaluable aid to the analysis that allowed the identification of sequences of lines, extending up from the lowest  $J$  rotational transitions. It should be stated, however, that the transition

frequencies for  $\text{CH}_3\text{NCO}$  reported in the line lists below are actual experimental frequencies. The power expansion fits were used to interpolate between the measured lines only in several cases of transitions missing in the spectrum for technical

reasons. It is anticipated that these expansions may have useful predictive properties outside the present data region, but only for those series for which the expansion containing a moderate number of expansion terms is sufficient.

### A.1. Spectroscopic constants and the partition function

The line lists for astrophysical detection require not only reliable line frequencies, but also line intensities that ultimately have a bearing on the derived column densities. Calculation of line intensities is crucially dependent on the rotational partition function,  $Q_{\text{rot}}$ , and  $\text{CH}_3\text{NCO}$  also poses a considerable inconvenience in this respect. For asymmetric rotor molecules with vibrational modes at relatively high frequencies the ground vibrational state rotational partition function can be usefully approximated with

$$Q_{\text{rot}} = 5.3311 \times 10^6 (T^3 / (ABC))^{1/2}, \quad (\text{A.2})$$

where  $A$ ,  $B$ , and  $C$  are the rotational constants for the molecule (in MHz) and  $T$  is the temperature (in K). Assumption of the rotational partition function for just the ground state of the molecule as the total partition function and neglect of population in excited vibrational states is normally associated with a relatively small underestimate, especially for low-temperature environments. For  $\text{CH}_3\text{NCO}$  this is not the case owing to the plethora of low-lying internal rotation substates, and it is necessary to consider the vibration-rotation partition function,  $Q_{\text{vr}}$ , explicitly. Furthermore, the difficulties in fitting more than a relatively small subset of measured transitions affect even the determination of the rotational constants. We summarize the situation in Table A.2, which demonstrates that even with a considerable reduction in the range of  $K_a$  values for the fitted transitions, the fit is less satisfactory than is usually the case with rotational spectra. Inclusion of measured transitions for all measured values of  $J$  requires the use of a rather large number of centrifugal distortion constants and values of some of these constants are also of considerable magnitude. This points to the very effective nature of such constants and to the considerable vibration-rotation interactions in the  $\text{CH}_3\text{NCO}$  molecule. The deviation of fit is also somewhat greater than the experimental accuracy. With these reservations in mind, we find rather good agreement between rotational constants resulting from the two fits based on very different subsets of the current data (the two central columns of Table A.2). We therefore use the combined fit of the indicated limited data (the rightmost column of Table A.2) as the source of rotational constants for evaluation of the partition function. The complete results of that fit are reported in Table A.3.

The second issue affecting the evaluation of the partition function is the summation over the energy levels. We used the SPCAT program to carry out this summation numerically, and the results are summarized in Table A.4. The nearly free internal rotor levels  $m = 1, 2, 4, 5$  are closer in character to the symmetric top case so that we used rotational constants  $A$  and  $(B + C)/2$  in the partition function calculation, while for the remaining sub-levels ( $m = 0$  and  $m$  being a multiple of 3) we used separate values of  $A$ ,  $B$ , and  $C$  (all from the final column of Table A.2). It can be seen in Table A.4a that at room-temperature and at a specimen astrophysical temperature of 120 K the partition function  $Q_{\text{vr}}$  increases significantly on addition of successive vibrational substates. It is only upon reaching vibrational energy of  $400 \text{ cm}^{-1}$  above the ground state that a moderate saturation of the value of  $Q_{\text{vr}}$  becomes apparent. This corresponds to the consideration of energy levels in the ground state and the 17 vibrational substates immediately above it.

Table A.4b further illustrates some technical aspects associated with the evaluation of  $Q_{\text{vr}}$  such as the necessity of using sufficiently broad limits on the values of the  $J$  and  $K$  quantum numbers. It turns out that the large values of centrifugal distortion constants from the effective fit for  $K \leq 2$  lead to unphysical compression of energy levels at the highest values of  $J$  and  $K$ , as highlighted by specific diagnostics from the SPCAT program. At the same time, the details of the summation have little effect on the estimate of the low temperature partition function. For this reason we settle on the “recommended” conditions, which pass the test that the value from the numerical summation for just the ground state is close to that from the analytical formula in Eq. (A.2).

The final result of these considerations is that at room-temperature it is necessary to use a partition function value that is almost 8 times greater than that for just the ground state, while at 120 K this ratio is closer to 4. It is clear that a reliable estimate of the partition function to use for the calculation of transition intensities will have a direct bearing on the derived astrophysical abundances of  $\text{CH}_3\text{NCO}$ .

### A.2. Line lists

The final results of the analysis of the laboratory rotational spectrum of  $\text{CH}_3\text{NCO}$  for use in astrophysical applications are presented in Tables A.5 and A.6. The experimental frequencies for 27 rotational transition sequences with the lowest vibrational energy are listed in Table A.5. Five more specimen transition sequences corresponding to higher vibrational energies and presenting a challenge to confident astrophysical detection are also included. This line list is also given in Table A.6 in the standard format of the JPL catalog (Pickett et al. 1998). Table A.6 contains line intensities and lower state energies so that it can be easily converted to a different temperature. Table A.6 constitutes the main tool for astrophysical detection and characterization of  $\text{CH}_3\text{NCO}$ , and we summarize the key parameters used in its evaluation:  $\mu = \mu_a = 2.882 \text{ D}$ ,  $T = 300 \text{ K}$ , and  $Q_{\text{vr}} = 138\,369$  calculated by summing over rotational levels limited by  $K < 11$  and  $J < 100$  for all vibrational states up to  $402.5 \text{ cm}^{-1}$  above the ground state.

We have already commented above on the key discrepancies between the experimental frequencies reported in Halfen et al. (2015) and those in this work as summarized in Table A.7. We further note that if we replace our frequencies in the fit for the ground state reported in Table A.3 by the three problematic  $m = 0$  lines at 60 160.932, 68 753.890, and 70 009.179 MHz (see Table A.7), then those lines are incompatible with this fit at obs.-calc. frequencies of near  $-1.1 \text{ MHz}$ . Our frequencies for these transitions have obs.-calc. values of less than  $0.03 \text{ MHz}$ , in a fit encompassing 201 pure rotational transition frequencies. In fact, the discrepancy of  $1 \text{ MHz}$  from a line sequence comprising around 40 lines and consisting of both Koput (1986) and our mm-wave lines would be immediately visible. This is clearly apparent in Fig. A.1 (second column from the left), where the 70010.208 MHz line is in good agreement with the sequence defined by a low order  $J(J + 1)$ -type fit, whereas a frequency of 70 009.179 MHz is clearly incompatible.

Finally, we note that the quantization used in Halfen et al. (2015) for the  $m = 0$ ,  $K_a = 1$  transitions deviates from standard practice. While the quantization for the  $m > 0$  lines is somewhat arbitrary and largely dependent on the fitting program, the quantization for the ground state is well established. In the case when the splitting between the two  $a$ -dipole  $\Delta J = 1$ ,  $K_a = 1$  transitions for a given value of  $J''$  is dominated by the asymmetry

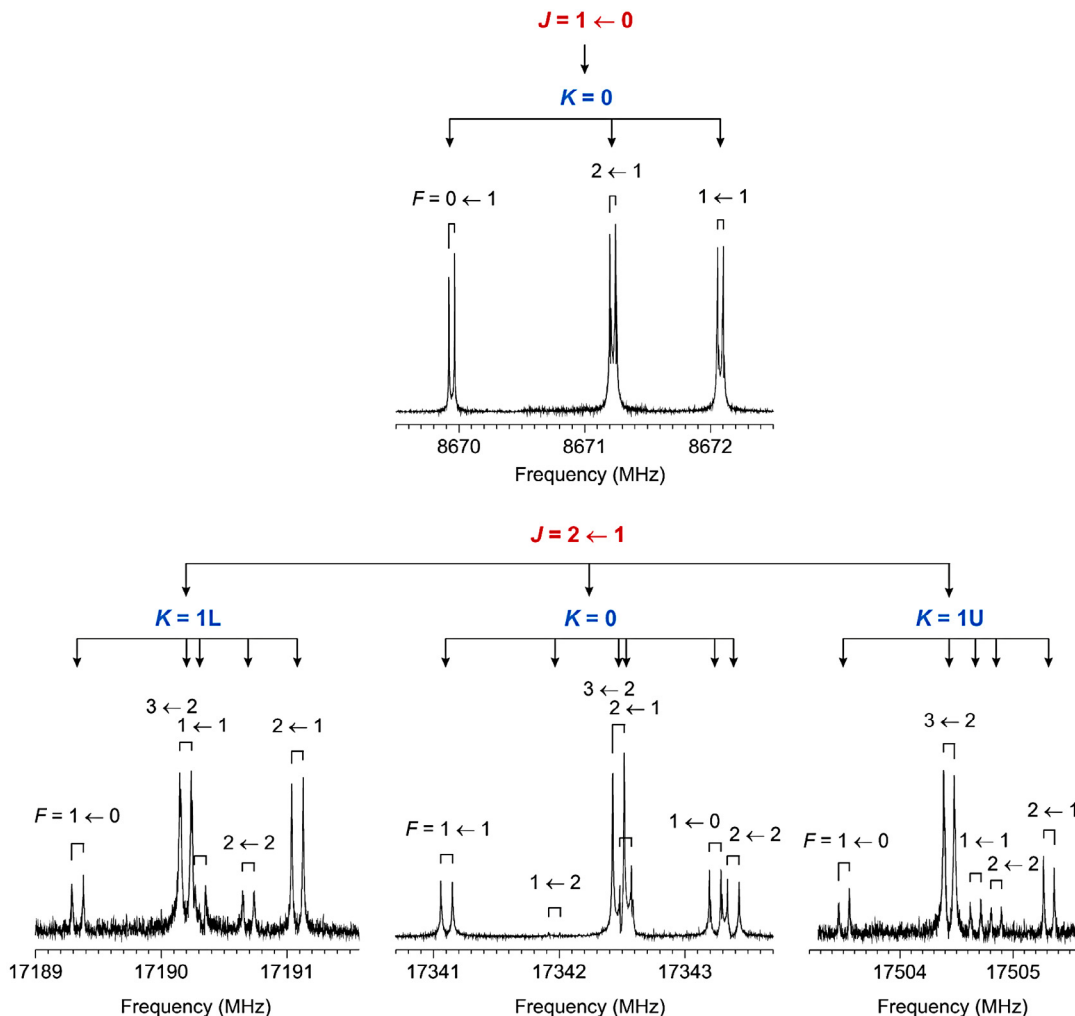


**Fig. A.2.** Splitting patterns in the lowest- $J$  rotational transitions in the ground state ( $v_b = 0, m = 0$ ) of  $\text{CH}_3\text{NCO}$ . The splitting is due to the interaction of the nuclear quadrupole of the  $^{14}\text{N}$  nucleus with molecular rotation and is characterized by the total angular momentum quantum number  $F$ . Each component is doubled by the Doppler doubling, which is an instrumental effect specific to the FP-FTMW spectrometer. The splitting is completely resolved at the supersonic expansion conditions ( $T_{\text{tot}} = 2$  K) of the FP-FTMW spectrometer. Nevertheless, the magnitude, and thus the relevance of the splitting, decreases rapidly with increasing  $J$ .

term in the rotational Hamiltonian (as is the case for  $\text{CH}_3\text{NCO}$ ) it is the  $K_a = 1$  transition with the *higher* value of  $K_c$  that is at *lower* frequency, and the one with *lower* value of  $K_c$  that is at *higher* frequency. This quantization leads to the moderately successful effective fit for the ground ( $m = 0$ ) state reported by us in Table A.3. On the other hand, in Halfen et al. (2015) the  $K_c$  quantization for  $m = 0, K_a = 1$  transitions is systematically reversed.

### A.3. Nuclear quadrupole hyperfine splitting

It should be noted that the lowest- $J$  rotational transitions of  $\text{CH}_3\text{NCO}$  are subject to nuclear quadrupole hyperfine splitting, and that the line lists discussed above provide in such cases only the average, hyperfine-free frequencies. The hyperfine splitting arising from the presence of the  $^{14}\text{N}$  nucleus in the  $\text{CH}_3\text{NCO}$  molecule was studied in previous works (Kasten & Dreizler 1986; Curl et al. 1963; Lett et al. 1967). We have now, for the first time, observed such lines at the very low temperature of supersonic expansion using two spectroscopic techniques.  $\text{CH}_3\text{NCO}$  was first investigated by broadband chirped-pulse Fourier transform microwave (CP-FTMW) spectroscopy (Brown et al. 2008)

in two different frequency ranges: 6–18 and 25–26 GHz (Mata et al. 2012). A gas mixture containing 0.3% of  $\text{CH}_3\text{NCO}$  in neon at the backing pressure of 3 bar was used for the pulsed jet expansion. These scans allowed explicit confirmation of the assignment of the ground state ( $v_b = 0, m = 0$ ) lines since these lines (and some of the lowest  $v_b = 0, m = 1$  substate lines) are the only lines expected to be visible at these conditions. In order to resolve the nuclear quadrupole hyperfine structure, further measurements were performed by supersonic expansion, Fabry-Perot cavity, and Fourier transform microwave (FP-FTMW) spectroscopy (Grabow et al. 1996) using two different configurations covering the frequency range from 4 to 18 GHz (Alonso et al. 1997; Bermúdez et al. 2014). Figure A.2 shows the experimentally recorded hyperfine patterns for the first two lowest- $J$  transitions of  $\text{CH}_3\text{NCO}$  and it is clear that at sub-MHz resolution consideration of such splitting is important. Table A.8 lists hyperfine component frequencies for all  $K \leq 2$  rotational transitions up to 80 GHz. This prediction has an estimated accuracy of around 5 kHz and was made by using the rightmost set of spectroscopic constants from Table A.2. It is apparent that the central  $\Delta F = +1$  components quickly coalesce, while the outer  $\Delta F = 0$  components rapidly lose intensity.

**Table A.2.** Spectroscopic constants determined for the ground state of CH<sub>3</sub>NCO ( $v_b = 0, m = 0$ ).

Constant	Koput (1986)	Hyperfine resolved $J \leq 2, K_a \leq 1$	Hyperfine unresolved $J \leq 42, K_a \leq 2$	All data
$A''$ (MHz)	73 849.2	128 356.(7623) <sup>b</sup>	128 435.(19)	128 402.(13)
$B$ (MHz)	4392.22	4414.2478(12)	4414.6182(93)	4414.6287(75)
$C$ (MHz)	4256.66	4257.1309(12)	4256.7490(85)	4256.7452(71)
$\Delta_J$ (kHz)		2.45(40)	2.3209(11)	2.32319(98)
$\Delta_{JK}$ (kHz)		-1202.3(23)	-1274.0(13)	-1271.46(73)
$\delta_J$ (kHz)			0.4042(14)	0.4038(14)
$\delta_K$ (kHz)			183.1(43)	187.4(35)
$\Phi_J$ (Hz)			-0.00191(47)	-0.00142(45)
$\Phi_{JK}$ (Hz)			-5.39(24)	-5.64(18)
$\Phi_{KJ}$ (Hz)			-68478.(285)	-67991.(167)
$\phi_{JK}$ (Hz)			-47.6(14)	-47.7(14)
$\chi_{aa}$ (MHz)	2.8358(75)	2.8461(18)		2.8441(49)
$\chi_{bb}$ (MHz)	-1.288(21)	-1.2981(30)		-1.2962(67)
$\chi_{cc}$ (MHz)	-1.548(21)	-1.5481(30)		-1.5478(67)
$N_{\text{lines}}^c$	13	32	201	233
$\sigma_{\text{fit}}^d$ (kHz)	6	3	94.6	91.2
$\sigma_{\text{rms}}^e$	0.842	0.674	1.89	1.87

**Notes.** <sup>(a)</sup>  $A$ ,  $B$ , and  $C$  are rotational constants;  $\Delta_J, \dots, \phi_{JK}$  are centrifugal distortion constants in Watson's  $A$ -reduced asymmetric rotor Hamiltonian; and  $\chi_{aa}, \chi_{bb}, \chi_{cc}$  are nuclear quadrupole hyperfine splitting constants for the <sup>14</sup>N nucleus. <sup>(b)</sup> Errors in parentheses are standard errors in units of the last digit. <sup>(c)</sup> The number of fitted lines. <sup>(d)</sup> Standard deviation of the fit. <sup>(e)</sup> Unitless (weighted) deviation of the fit.

**Table A.3.** Results of fitting the spectroscopic constants of Table A.2 for CH<sub>3</sub>NCO ground state ( $m = 0$ ).

J' Ka' Kc' F' J'' Ka'' Kc'' F''	obs. (MHz)	o.-c. (MHz)	error (MHz)	J' Ka' Kc' F' J'' Ka'' Kc'' F''	obs. (MHz)	o.-c. (MHz)	error (MHz)
Valladolid supersonic expansion, cavity FTMW (small splitting in some components averaged)				18 0 18	17 0 17	155889.8670	-0.0382 0.050
				19 0 19	18 0 18	164527.3080	-0.0074 0.050
				20 0 20	19 0 19	173161.0610	-0.0158 0.050
1 0 1 0	8669.9439	0.0013	0.003	21 0 21	20 0 20	181791.1040	0.0759 0.050
1 0 1 2	8671.2271	0.0047	0.005	22 0 22	21 0 21	190417.0240	0.0104 0.050
1 0 1 1	8672.0809	0.0053	0.005	23 0 23	22 0 22	199038.8460	-0.0381 0.050
				24 0 24	23 0 23	207656.4340	-0.0633 0.050
2 0 2 1	17341.1048	0.0012	0.003	25 0 25	24 0 24	216269.6740	-0.0442 0.050
2 0 2 1	17341.9591	0.0023	0.003	26 0 26	25 0 25	224878.3540	-0.0656 0.050
2 0 2 3	17342.4705	0.0059	0.003	27 0 27	26 0 26	233482.3920	-0.0910 0.050
2 0 2 2	17342.5315	0.0059	0.005	28 0 28	27 0 27	242081.6800	-0.1184 0.050
2 0 2 1	17343.2442	0.0076	0.005	29 0 29	28 0 28	250676.1400	-0.1257 0.050
2 0 2 2	17343.3848	0.0059	0.003	30 0 30	29 0 29	259265.7080	-0.0864 0.050
				31 0 31	30 0 30	267850.1630	-0.1414 0.050
2 1 2 1	17189.3349	0.0021	0.003	32 0 32	31 0 31	276429.6520	-0.0742 0.050
2 1 2 3	17190.1971	0.0046	0.005	33 0 33	32 0 32	285003.8410	-0.1606 0.050
2 1 2 1	17190.3077	0.0027	0.003	34 0 34	33 0 33	293572.9900	-0.0933 0.050
2 1 2 2	17190.6905	0.0005	0.003	35 0 35	34 0 34	302136.8980	-0.0380 0.050
2 1 2 2	17191.0845	0.0056	0.003	36 0 36	35 0 35	310695.4270	-0.1085 0.050
				37 0 37	36 0 36	319248.7530	-0.1168 0.050
2 1 1 1	17503.5055	-0.0029	0.003	38 0 38	37 0 37	327797.0500	0.1116 0.050
2 1 1 3	17504.4327	-0.0037	0.003	39 0 39	38 0 38	336339.8860	0.1341 0.050
2 1 1 1	17504.6671	-0.0022	0.003	40 0 40	39 0 39	344877.4680	0.1351 0.050
2 1 1 2	17504.8506	-0.0025	0.003	41 0 41	40 0 40	353409.8830	0.1685 0.050
2 1 1 2	17505.3161	-0.0013	0.003	42 0 42	41 0 41	361937.2030	0.2623 0.050
Kasten + Dreizler				2 1 2	1 1 1	17190.6700	0.3022 0.050
				3 1 3	2 1 2	25785.4100	0.0606 0.050
1 0 1 0	8669.9540	0.0114	0.005	4 1 4	3 1 3	34380.1400	0.0516 0.050
1 0 1 2	8671.2240	0.0016	0.005	5 1 5	4 1 4	42974.4300	-0.0743 0.050
1 0 1 1	8672.0790	0.0033	0.005	6 1 6	5 1 5	51568.5290	0.0117 0.050
				7 1 7	6 1 6	60162.0760	0.0288 0.050
2 0 2 3	17342.4670	0.0023	0.005	8 1 8	7 1 7	68755.0250	0.0099 0.050
2 0 2 2	17342.5360	0.0104	0.005	9 1 9	8 1 8	77347.4250	0.0828 0.050
2 0 2 1	17343.2340	-0.0025	0.005	10 1 10	9 1 9	85938.9620	0.0115 0.050
2 0 2 2	17343.3790	0.0001	0.005	11 1 11	10 1 10	94529.7610	-0.0016 0.050
				12 1 12	11 1 11	103119.7030	0.0008 0.050
2 1 2 1	17189.3380	0.0052	0.005	13 1 13	12 1 12	111708.7070	0.0135 0.050
2 1 2 3	17190.1970	0.0046	0.005	14 1 14	13 1 13	120296.6300	-0.0318 0.050
2 1 2 2	17191.0820	0.0031	0.005	15 1 15	14 1 14	128883.6440	0.1105 0.050
				16 1 16	15 1 15	137469.2870	0.0511 0.050
2 1 1 1	17503.5090	0.0005	0.005	17 1 17	16 1 16	146053.5740	-0.1234 0.050
2 1 1 3	17504.4390	0.0026	0.005	18 1 18	17 1 17	154636.8670	0.0190 0.050
2 1 1 2	17505.3220	0.0045	0.005	19 1 19	18 1 18	163218.6020	-0.0162 0.050
				20 1 20	19 1 19	171798.9900	0.0492 0.050
Hyperfine-free lines: Koput + MMW Valladolid + FASSST				21 1 21	20 1 20	180377.7680	0.0191 0.050
				22 1 22	21 1 21	188955.1000	0.1222 0.050
1 0 1	8671.4100	0.0454	0.050	23 1 23	22 1 22	197530.5550	-0.0088 0.050
2 0 2	17342.5000	-0.0255	0.050	24 1 24	23 1 23	206104.4470	0.0019 0.050
3 0 3	26013.3400	0.0604	0.050	25 1 25	24 1 24	214676.5300	-0.0308 0.050
4 0 4	34683.4600	0.0365	0.050	26 1 26	25 1 25	223246.8260	-0.0262 0.050
5 0 5	43352.7630	0.0083	0.050	27 1 27	26 1 26	231815.2500	-0.0118 0.050
6 0 6	52021.1060	0.0350	0.050	28 1 28	27 1 27	240381.6640	-0.0699 0.050
7 0 7	60688.2100	0.0387	0.050	29 1 29	28 1 28	248946.1500	-0.0642 0.050
8 0 8	69353.8800	0.0247	0.050	30 1 30	29 1 29	257508.6010	-0.0494 0.050
9 0 9	78017.9530	0.0292	0.050	31 1 31	30 1 30	266068.9260	-0.0654 0.050
10 0 10	86680.1900	0.0106	0.050	32 1 32	31 1 31	274627.1410	-0.0472 0.050
11 0 11	95340.4430	0.0172	0.050	33 1 33	32 1 32	283183.2160	0.0227 0.050
12 0 12	103998.4810	0.0120	0.050	34 1 34	33 1 33	291736.8910	-0.0696 0.050
13 0 13	112654.0590	-0.0580	0.050	35 1 35	34 1 34	300288.3190	-0.1272 0.050
14 0 14	121307.2370	0.0565	0.050	36 1 36	35 1 35	308837.5260	-0.0814 0.050
15 0 15	129957.4710	-0.0016	0.050	37 1 37	36 1 36	317384.4490	0.0455 0.050
16 0 16	138604.6700	-0.1401	0.050	38 1 38	37 1 37	325928.8020	0.0070 0.050
17 0 17	147248.8260	-0.1869	0.050	39 1 39	38 1 38	334470.6160	-0.1282 0.050

Table A.3. continued.

J' Ka' Kc' F'	J'' Ka'' Kc'' F''	obs. (MHz)	o.-c. (MHz)	error (MHz)	J' Ka' Kc' F'	J'' Ka'' Kc'' F''	obs. (MHz)	o.-c. (MHz)	error (MHz)
40 1 40	39 1 39	343010.1490	-0.0662	0.050	27 2 26	26 2 25	234088.1250	0.0727	0.050
41 1 41	40 1 40	351547.2590	0.0855	0.050	28 2 27	27 2 26	242738.3090	0.0422	0.050
42 1 42	41 1 41	360081.6650	0.0791	0.050	29 2 28	28 2 27	251386.4480	0.0707	0.050
					30 2 29	29 2 28	260032.3910	0.0742	0.050
2 1 1	1 1 0	17504.6800	0.0736	0.050	31 2 30	30 2 29	268676.1360	0.1167	0.050
3 1 2	2 1 1	26256.7100	0.0570	0.050	32 2 31	31 2 30	277317.4920	0.0724	0.050
4 1 3	3 1 2	35008.4300	0.0383	0.050	33 2 32	32 2 31	285956.5910	0.1375	0.050
5 1 4	4 1 3	43759.6000	-0.1197	0.050	34 2 33	33 2 32	294593.2450	0.1876	0.050
6 1 5	5 1 4	52510.5630	0.0283	0.050	35 2 34	34 2 33	303227.2980	0.1288	0.050
7 1 6	6 1 5	61260.7340	0.0003	0.050	36 2 35	35 2 34	311858.7810	0.0538	0.050
8 1 7	7 1 6	70010.2080	-0.0061	0.050	37 2 36	36 2 35	320487.6960	0.0250	0.050
9 1 8	8 1 7	78758.8490	-0.0242	0.050	38 2 37	37 2 36	329113.8250	-0.1161	0.050
10 1 9	9 1 8	87506.6070	-0.0014	0.050	39 2 38	38 2 37	337737.4330	-0.0463	0.050
11 1 10	10 1 9	96253.3180	0.0010	0.050	40 2 39	39 2 38	346358.1370	-0.0911	0.050
12 1 11	11 1 10	104998.8860	-0.0099	0.050	41 2 40	40 2 39	354975.8680	-0.2633	0.050
13 1 12	12 1 11	113743.2410	-0.0017	0.050					
14 1 13	13 1 12	122486.1730	-0.0815	0.050	3 2 1	2 2 0	26038.2000	-0.2472	0.050
15 1 14	14 1 13	131227.9270	0.0983	0.050	4 2 2	3 2 1	34718.1100	-0.1397	0.050
16 1 15	15 1 14	139967.9030	0.0408	0.050	5 2 3	4 2 2	43398.2650	-0.0609	0.050
17 1 16	16 1 15	148706.1240	-0.1284	0.050	6 2 4	5 2 3	52078.6310	-0.1122	0.050
18 1 17	17 1 16	157442.8620	-0.0346	0.050	7 2 5	6 2 4	60759.4890	-0.0795	0.050
19 1 18	18 1 17	166177.7250	0.0329	0.050	8 2 6	7 2 5	69440.7720	-0.0958	0.050
20 1 19	19 1 18	174910.5960	0.0600	0.050	9 2 7	8 2 6	78122.5870	-0.1191	0.050
21 1 20	20 1 19	183641.4610	0.1354	0.050	10 2 8	9 2 7	86805.0270	-0.1203	0.050
22 1 21	21 1 20	192370.0130	0.0546	0.050	11 2 9	10 2 8	95488.1310	-0.1230	0.050
23 1 22	22 1 21	201096.3660	0.0342	0.050	12 2 10	11 2 9	104171.9620	-0.1249	0.050
24 1 23	23 1 22	209820.3630	0.0198	0.050	13 2 11	12 2 10	112856.5850	-0.1202	0.050
25 1 24	24 1 23	218541.8030	-0.0873	0.050	14 2 12	13 2 11	121542.1130	-0.0526	0.050
26 1 25	25 1 24	227260.7990	-0.0719	0.050	15 2 13	14 2 12	130228.4190	-0.1035	0.050
27 1 26	26 1 25	235977.1810	-0.0017	0.050	16 2 14	15 2 13	138915.6030	-0.2246	0.050
28 1 27	27 1 26	244690.7010	-0.0229	0.050	17 2 15	16 2 14	147603.9630	-0.1665	0.050
29 1 28	28 1 27	253401.3880	-0.0047	0.050	18 2 16	17 2 15	156293.3170	-0.1560	0.050
30 1 29	29 1 28	262109.0720	-0.0154	0.050	19 2 17	18 2 16	164983.8810	-0.0181	0.050
31 1 30	30 1 29	270813.7400	0.0330	0.050	20 2 18	19 2 17	173675.3920	-0.0527	0.050
32 1 31	31 1 30	279515.0450	-0.1052	0.050	21 2 19	20 2 18	182368.2180	0.0764	0.050
33 1 32	32 1 31	288213.2250	-0.0916	0.050	22 2 20	21 2 19	191062.0290	0.0127	0.050
34 1 33	33 1 32	296908.3040	0.1980	0.050	23 2 21	22 2 20	199757.0680	-0.0215	0.050
35 1 34	34 1 33	305599.5880	0.1696	0.050	24 2 22	23 2 21	208453.3650	-0.0110	0.050
36 1 35	35 1 34	314287.2370	0.0824	0.050	25 2 23	24 2 22	217150.9320	0.0484	0.050
37 1 36	36 1 35	322971.2260	0.0103	0.050	26 2 24	25 2 23	225849.6710	0.0584	0.050
38 1 37	37 1 36	331651.4570	-0.0465	0.050	27 2 25	26 2 24	234549.6360	0.0803	0.050
39 1 38	38 1 37	340327.9230	0.0023	0.050	28 2 26	27 2 25	243250.7340	0.0367	0.050
40 1 39	39 1 38	349000.2270	-0.1433	0.050	29 2 27	28 2 26	251953.1080	0.0948	0.050
41 1 40	40 1 39	357668.8020	0.0454	0.050	30 2 28	29 2 27	260656.5870	0.1172	0.050
					31 2 29	30 2 28	269361.1960	0.1722	0.050
3 2 2	2 2 1	26038.2000	0.3438	0.050	32 2 30	31 2 29	278066.7380	0.1158	0.050
4 2 3	3 2 2	34716.9100	0.1374	0.050	33 2 31	32 2 30	286773.1780	-0.0233	0.050
5 2 4	4 2 3	43395.5400	0.1671	0.050	34 2 32	33 2 31	295480.8970	0.2095	0.050
6 2 5	5 2 4	52073.4700	-0.1083	0.050	35 2 33	34 2 32	304189.1200	0.1243	0.050
7 2 6	6 2 5	60751.2420	-0.0683	0.050	36 2 34	35 2 33	312898.1990	0.1688	0.050
8 2 7	7 2 6	69428.4030	-0.0873	0.050	37 2 35	36 2 34	321607.6950	0.0104	0.050
9 2 8	8 2 7	78104.9430	-0.0972	0.050	38 2 36	37 2 35	330317.8260	-0.0153	0.050
10 2 9	9 2 8	86780.7780	-0.1038	0.050	39 2 37	38 2 36	339028.2350	-0.1373	0.050
11 2 10	10 2 9	95455.8140	-0.1235	0.050	40 2 38	39 2 37	347738.9940	-0.1447	0.050
12 2 11	11 2 10	104130.0100	-0.1199	0.050	41 2 39	40 2 38	356449.7320	-0.2598	0.050
13 2 12	12 2 11	112803.2580	-0.1239	0.050					
14 2 13	13 2 12	121475.4960	-0.1208	0.050					
15 2 14	14 2 13	130146.7990	0.0408	0.050					
16 2 15	15 2 14	138816.7390	0.0087	0.050					
17 2 16	16 2 15	147485.3600	-0.0974	0.050					
18 2 17	17 2 16	156152.7430	-0.1219	0.050					
19 2 18	18 2 17	164818.8450	-0.0332	0.050					
20 2 19	19 2 18	173483.4660	0.0426	0.050					
21 2 20	20 2 19	182146.4730	0.0458	0.050					
22 2 21	21 2 20	190807.8310	0.0143	0.050					
23 2 22	22 2 21	199467.5590	0.0390	0.050					
24 2 23	23 2 22	208125.4910	0.0254	0.050					
25 2 24	24 2 23	216781.6210	0.0382	0.050					
26 2 25	25 2 24	225435.8490	0.0476	0.050					

**Table A.4.** Determination of the partition function for transition intensity calculations.

(a) Evolution of the value of $Q_{\text{vr}}$ on addition of successive vibrational states to the summation					(b) Sensitivity of the value of $Q_{\text{vr}}$ to quantum number limits used in the numerical summation					
$J_{\text{lim}} = 50, K_{\text{lim}} = 15$		$E_{\text{vib}} \text{ (cm}^{-1}\text{)}$	$Q_{\text{vr}} \text{ (300 K)}$	$Q_{\text{vr}} \text{ (120 K)}$		$J_{\text{lim}}$	$K_{\text{lim}}$	$Q_{\text{vr}} \text{ (300 K)}$	$Q_{\text{vr}} \text{ (120 K)}$	
	$v_b = 0$	$m = 0$	0.0	15 055	4474	all <sup>a</sup>	50	10	113 660	18 021
+		$m = 1$	8.4	29 292	8509	all	70	10	132 301	18 223
+		$m = 2$	36.8	41 716	11 379	all	100	10	136 409	18 225
+		$m = 3\text{L}$	80.3	51 802	13 083	all	50	15	117 404	18 035
+		$m = 3\text{U}$	79.7	61 916	14 799	all	70	15	136 815	18 237
+		$m = 4$	140.6	69 468	15 626	all	100	15 <sup>b</sup>	141 159	18 240
+		$m = 5$	217.5	74 691	15 955					
+		$m = 6\text{a}$	311.1	78 025	16 062					
+		$m = 6\text{b}$	311.1	81 359	16 169					
	$v_b = 1$	$m = 0$	182.2	87 546	16 671	<u>Recommended:</u>				
		$m = 1$	191.4	93 465	17 121					
		$m = 2$	222.3	98 569	17 431		100	11		
		$m = 3\text{a}$	268.3	102 663	17 610	all			138 369	18 235
		$m = 3\text{b}$	268.9	106 745	17 788	only $v_b, m = 0, 0$			17 744	4524
		$m = 4$	333.4	109 741	17 870	only $v_b, m = 0, 0$	analytical		17 831	4511
+	$v_b = 2$	$m = 0$	357.9	112 405	17 931					
		$m = 1$	368.6	114 935	17 984					
		$m = 2$	402.5	117 404	18 035					

**Notes.** <sup>(a)</sup> Summation over all vibrational states up to  $402.5 \text{ cm}^{-1}$  ( $v_b = 2, m = 2$ ). <sup>(b)</sup> Energy level compression problems at highest  $K$  and  $J$  due to large values of some centrifugal distortion constants in the effective fit.

**Table A.5.** Line list of rotational transitions for CH<sub>3</sub>NCO compiled from experimental frequencies (MHz) for line sequences assigned on the basis of continuity from the assignment reached for  $J'' \leq 3$ .(a)  $v_b = 0$ ,  $m = 0$  (ground state),  $E_{\text{vib}} = 0 \text{ cm}^{-1}$ .

$K^a =$		0	1L	1U	2L	2U	3L	3U
$J'$	$J''$							
1	0	8 671.410 <sup>b</sup>						
2	1	17 342.500	17 190.670	17 504.680				
3	2	26 013.340	25 785.410	26 256.710	26 038.200	26 038.200		
4	3	34 683.460	34 380.140	35 008.430	34 716.910	34 718.110	34 596.030	34 596.030
5	4	43 352.763	42 974.430	43 759.600	43 395.540	43 398.265	43 244.392	43 244.392
6	5	52 021.106	51 568.529	52 510.563	52 073.470	52 078.631	51 891.662	51 891.662
7	6	60 688.210	60 162.076	61 260.734	60 751.242	60 759.489	60 538.443	60 538.443
8	7	69 353.880	68 755.025	70 010.208	69 428.403	69 440.772	69 184.277	69 184.277
9	8	78 017.953	77 347.425	78 758.849	78 104.943	78 122.587	77 829.107	77 829.107
10	9	86 680.190	85 938.962	87 506.607	86 780.778	86 805.027	86 472.805	86 472.805
11	10	95 340.443	94 529.761	96 253.318	95 455.814	95 488.131	95 115.214	95 115.214
12	11	103 998.481	103 119.703	104 998.886	104 130.010	104 171.962	103 756.254	103 756.254
13	12	112 654.059	111 708.707	113 743.241	112 803.258	112 856.585	112 395.756	112 395.756
14	13	121 307.237	120 296.630	122 486.173	121 475.496	121 542.113	121 033.586	121 033.586
15	14	129 957.471	128 883.644	131 227.927	130 146.799	130 228.419	129 669.703	129 669.703
16	15	138 604.670	137 469.287	139 967.903	138 816.739	138 915.603	138 303.496	138 304.065
17	16	147 248.826	146 053.574	148 706.124	147 485.360	147 603.963	146 935.424	146 936.284
18	17	155 889.867	154 636.867	157 442.862	156 152.743	156 293.317	155 565.312	155 566.394
19	18	164 527.308	163 218.602	166 177.725	164 818.845	164 983.881	164 192.884	164 194.278
20	19	173 161.061	171 798.990	174 910.596	173 483.466	173 675.392	172 817.892	172 819.679
21	20	181 791.104	180 377.768 <sup>c</sup>	183 641.461	182 146.473	182 368.218	181 440.422	181 442.696
22	21	190 417.024	188 955.100	192 370.013	190 807.831	191 062.029	190 060.149	190 062.937
23	22	199 038.846	197 530.555	201 096.366	199 467.559	199 757.068	198 677.070	198 680.500
24	23	207 656.434	206 104.447	209 820.363	208 125.491	208 453.365	207 291.046	207 295.249
25	24	216 269.674	214 676.530	218 541.803	216 781.621	217 150.932	215 902.003	215 907.102
26	25	224 878.354	223 246.826	227 260.799	225 435.849	225 849.671	224 509.835	224 515.940
27	26	233 482.392	231 815.250	235 977.181	234 088.125	234 549.636	233 114.404	233 121.696
28	27	242 081.680	240 381.664	244 690.701	242 738.309	243 250.734	241 715.637	241 724.217
29	28	250 676.140	248 946.150	253 401.388	251 386.448	251 953.108	250 313.498	250 323.521
30	29	259 265.708	257 508.601	262 109.072	260 032.391	260 656.587	258 907.935	258 919.578
31	30	267 850.163	266 068.926	270 813.740	268 676.136	269 361.196	267 498.881	267 512.332
32	31	276 429.652	274 627.141	279 515.045	277 317.492	278 066.738	276 086.286	276 101.741
33	32	285 003.841	283 183.216	288 213.225	285 956.591	286 773.178	284 670.169	284 687.756
34	33	293 572.990	291 736.891	296 908.304	294 593.245	295 480.897	293 250.547	293 270.510
35	34	302 136.898	300 288.319	305 599.588	303 227.298	304 189.120	301 827.305	301 849.816
36	35	310 695.427	308 837.526	314 287.237	311 858.781	312 898.199	310 400.543	310 425.797
37	36	319 248.753	317 384.449	322 971.226	320 487.696	321 607.695	318 970.615	318 998.776
38	37	327 797.050	325 928.802	331 651.457	329 113.825	330 317.826	327 536.993	327 568.310
39	38	336 339.886	334 470.616	340 327.923	337 737.433	339 028.235	336 099.791	336 134.374
40	39	344 877.468	343 010.149	349 000.227	346 358.137	347 738.994	344 659.995	344 698.049
41	40	353 409.883	351 547.259	357 668.802	354 975.868	356 449.732	353 216.538	353 258.418
42	41	361 937.203	360 081.665				361 770.522	361 816.048
sequence		V093	V126	V131	V089	V006	V096	V097

**Notes.** <sup>(a)</sup> The  $K$  quantum number notation is defined in the text below Eq. (A.1). <sup>(b)</sup> All frequencies for  $J'' > 3$  (unless otherwise marked) are experimental measurements with estimated uncertainty of 0.05 MHz. The frequencies for  $J'' = 0$  to 3 are hyperfine removed frequencies evaluated by Koput. <sup>(c)</sup> Calculated from a  $J(J+1)$  power series fit to the sequence.

Table A.5. continued.

(b)  $v_b = 0$ ,  $m=1$ ,  $E_{\text{vib}} = 8.4 \text{ cm}^{-1}$ .

$K =$		0	-1	1	2	-3	3
$J'$	$J''$						
1	0	8714.599					
2	1	17 426.089	17 131.350	17 139.540			
3	2	26 131.320	25 696.960	25 711.200	26 102.200		
4	3	34 827.319	34 262.960	34 285.420	34 803.370	34 746.730	34 848.720
5	4	43 511.298	42 829.348	42 862.701	43 504.452	43 433.533	43 560.652
6	5	52 181.118	51 396.202	51 443.858	52 206.120	52 119.989	52 272.360
7	6	60 834.588	59 963.808	60 029.019	60 907.932	60 806.734	60 694.881
8	7	69 470.354	68 532.241	68 618.612	69 610.243	69 493.349	69 405.765
9	8	78 087.660	77 101.788	77 212.768	78 312.951	78 180.079	78 116.220
10	9	86 686.556	85 672.565	85 811.546	87 016.078	86 866.748	86 826.264
11	10	95 267.825	94 244.905	94 414.872	95 719.797	95 553.457	95 535.872
12	11	103 832.990	102 819.142	103 022.546	104 424.130	104 240.089	104 245.010
13	12	112 384.189	111 395.453	111 634.362	113 129.051	112 926.739	112 953.658
14	13	120 923.957	119 974.084	120 250.061	121 834.685	121 613.360	121 661.691
15	14	129 455.041	128 555.310	128 869.183	130 541.066	130 300.215	130 369.066
16	15	137 980.105	137 139.779	137 491.243	139 248.143	138 986.740	138 975.687
17	16	146 501.448	145 726.977	146 115.877	147 956.022	147 673.312	147 781.803
18	17	155 021.205	154 317.714	154 742.833	156 664.792	156 360.035	156 487.174
19	18	163 541.133	162 911.754	163 371.518	165 374.452	165 046.706	165 191.731
20	19	172 061.977	171 509.498	172 001.511	174 085.007	173 733.277	173 895.436
21	20	180 584.517 <sup>a</sup>	180 110.821 <sup>a</sup>	180 632.418	182 796.656	182 419.917	182 598.170
22	21	189 109.455	188 715.886	189 263.550	191 508.907	191 106.420	191 300.118
23	22	197 636.492	197 324.512	197 894.577	200 222.279	199 792.672	200 001.126
24	23	206 165.981	205 936.596	206 525.339	208 936.733	208 478.868	208 701.086
25	24	214 697.618	214 552.442	215 155.261	217 652.088	217 164.881	217 400.016
26	25	223 231.128	223 171.503	223 783.952	226 368.543	225 850.618	225 997.875
27	26	231 766.341	231 793.783	232 411.044	235 085.938	234 535.866	234 794.484
28	27	240 302.835	240 418.979	241 036.217	243 804.350	243 220.575	243 490.045
29	28	248 840.351	249 047.052	249 659.091	252 523.689	251 904.576	252 184.367
30	29	257 378.635	257 677.673	258 279.428	261 243.934	260 587.611	260 877.354
31	30	265 917.341	266 310.654	266 896.862	269 964.935	269 269.306	269 569.028
32	31	274 456.286	274 945.807	275 511.130	278 686.471	277 949.280	278 259.016
33	32	282 995.138	283 582.597	284 122.057	287 408.067	286 626.968	286 948.943
34	33	291 533.591	292 221.402	292 729.120	296 130.228	295 302.132	295 636.157
35	34	300 071.437	300 861.390	301 332.036	304 850.123	303 973.342	304 322.215
36	35	308 608.768	309 502.679	309 930.935	<i>b</i>	312 639.870	312 006.608
37	36	317 145.274	318 145.064	318 525.546	<i>b</i>	321 299.883	320 689.686
38	37	325 680.738	326 788.371	327 115.335	<i>b</i>	329 952.435	329 370.491
39	38	334 214.702	335 432.305	335 700.385	<i>b</i>	338 594.440	338 050.671
40	39	342 747.571	344 077.189	344 280.710	<i>b</i>	347 223.487	346 728.558
41	40	351 278.907	352 722.522	352 855.727	<i>b</i>	355 835.853	
42	41	359 808.783	361 368.607	361 425.535	<i>b</i>		
sequence		V107+X107	V101	V098	V010	V005	V012

Notes. <sup>(a)</sup> Calculated from a  $J(J+1)$  power series fit to the sequence. <sup>(b)</sup> Sequence too perturbed for confident assignment.

Table A.5. continued.

(c)  $v_b = 0$ ,  $m = -2$ ,  $E_{\text{vib}} = 36.8 \text{ cm}^{-1}$ .

$K =$		0	-1	1	2	-3	3
$J'$	$J''$						
1	0	8712.440					
2	1	17 424.730	17 413.270	17 404.820			
3	2	26 137.030	26 119.520	26 109.160	25 664.890		
4	3	34 849.040	34 825.770	34 816.500	34 225.420	34 934.900	34 961.090
5	4	43 560.897 <sup>a,b</sup>	43 532.117	43 527.498	42 790.309	43 668.171	43 682.672
6	5	52 272.451 <sup>a,b</sup>	52 238.073	52 242.597	51 360.437	52 401.386	52 392.272
7	6	60 983.669 <sup>a,b</sup>	60 944.058	60 962.565	59 936.461	61 134.338	61 088.422
8	7	69 694.485	69 649.804	69 687.625	68 518.731	69 866.924	69 769.729
9	8	78 404.856	78 355.412	78 417.926	77 107.514	78 599.133	78 435.325
10	9	87 114.738	87 060.710	87 153.379	85 702.751	87 330.888	87 084.556
11	10	95 824.056	95 765.763	95 893.514	94 304.411	96 062.185	95 717.491
12	11	104 532.714	104 470.566	104 637.665	102 912.045	104 793.013	104 334.474
13	12	113 240.653	113 175.049	113 384.876	111 525.320	113 523.228	112 936.205
14	13	121 947.700	121 879.231	122 134.022	120 143.754	122 252.995	121 523.853
15	14	130 653.851	130 583.038	130 883.320	128 766.726	130 982.052	130 098.915
16	15	139 358.532	139 286.363	139 631.255	137 393.143	139 710.254	138 663.325
17	16	148 061.901	147 989.218	148 376.092	146 022.743	148 437.799	147 218.459
18	17	156 763.754	156 691.751	157 116.399	154 654.800	157 164.567	155 766.873
19	18	165 463.564	165 393.941	165 850.049	163 288.573	165 890.628	164 310.386
20	19	174 161.002	174 095.570	174 575.538	171 923.201	174 615.757	172 850.953
21	20	182 855.593	182 796.656	183 291.443	180 558.028 <sup>a</sup>	183 339.996	181 390.412
22	21	191 546.894	191 497.178	191 996.548	189 192.720	192 063.146	189 930.316
23	22	200 234.301	200 197.129	200 690.051	197 826.437	200 785.291	198 472.093
24	23	208 917.318	208 896.491	209 371.092	206 458.663	209 506.446	207 017.068
25	24	217 595.174	217 595.174	218 039.456	215 089.004	218 226.496	215 566.166
26	25	226 267.092	226 293.413	226 694.967	223 717.009	226 945.439	224 120.207
27	26	234 932.492 <sup>a</sup>	234 990.914	235 337.649	232 342.227	235 663.096	232 679.828
28	27	243 590.630	243 687.653	243 967.818	240 964.280	244 379.611	241 245.454
29	28	252 240.796	252 383.755	252 585.612	249 582.840	253 094.867	249 817.533
30	29	260 882.339	261 079.084	261 192.583	258 197.662	261 808.735	258 396.339
31	30	269 514.732	269 773.683	269 788.424	266 808.428	270 521.346	266 982.150
32	31	278 137.623	278 467.359	278 374.254	275 414.952	279 232.105	275 575.274
33	32	286 750.691	287 160.285	286 951.163	284 016.740	287 942.047	284 176.013
34	33	295 354.251	295 852.776	295 520.181	292 614.021	296 650.575	292 784.604
35	34	303 947.944	304 543.877	304 081.558	301 205.925	305 357.256	301 401.555
36	35	312 532.293	313 234.118	312 636.900	309 792.917	314 062.421	310 027.841
37	36	321 107.766	321 923.326	321 186.461	318 374.616	322 765.830	318 664.379
38	37	329 675.596	330 611.777	329 732.148	326 950.804	331 468.033	327 312.231
39	38	338 235.598	339 298.928	338 273.907	335 521.348	340 168.379	335 973.272
40	39	346 789.247	347 985.229	346 813.067	344 086.535	348 867.181	344 650.251
41	40	355 337.165	356 670.230	355 350.283	352 645.714	357 564.298	353 345.626
42	41				361 199.462		362 063.629
sequence		V119	V008	V180	V100	V024	V106+X106

Notes. <sup>(a)</sup> Calculated from a  $J(J+1)$  power series fit to the sequence. <sup>(b)</sup> Not measured since blended with another sequence.

Table A.5. continued.

(d)  $v_b = 0$ ,  $m = 3L$ ,  $E_{\text{vib}} = 80.3 \text{ cm}^{-1}$ .

$K =$		0	-1	1	2	3
$J'$	$J''$					
1	0	8722.070				
2	1	17 444.100	17 504.680	17 448.710		
3	2	26 166.190	26 257.660	26 172.870	26 217.200	
4	3	34 888.140	35 011.480	34 896.830	34 956.060	35 028.630
5	4	43 609.928	43 766.214	43 620.571	43 694.834	43 785.654
6	5	52 331.868	52 522.551	52 344.346	52 433.136	52 542.085
7	6	61 053.565	61 280.451 <sup>a</sup>	61 067.774	61 171.238	61 298.342
8	7	69 775.192	70 040.195	69 790.946	69 909.074	70 054.280
9	8	78 496.665	78 801.997	78 513.797	78 646.527	78 809.809
10	9	87 218.054	87 565.977	87 236.266	87 383.509	87 564.879
11	10	95 939.244	96 332.237	95 958.329	96 120.050	96 319.430
12	11	104 660.269	105 100.806	104 679.971	104 856.074	105 073.483
13	12	113 381.115	113 871.438	113 401.139	113 591.533	113 826.888
14	13	122 101.880	122 644.153	122 121.912	122 326.370	122 579.897
15	14	130 822.366	131 418.379	130 841.787	131 060.695	131 331.907
16	15	139 542.464	140 193.007	139 561.260	139 794.246 <sup>a</sup>	140 083.196
17	16	148 262.442	148 967.780	148 280.088	148 526.918	148 833.657
18	17	156 982.205	157 741.459	156 998.138	157 259.087	157 583.442
19	18	165 701.855	166 512.305	165 715.596	165 990.220	166 332.231
20	19	174 421.255	175 278.820	174 432.265	174 720.445	175 080.257
21	20	183 140.586	184 038.905	183 148.090	183 449.784	183 827.235
22	21	191 859.411	192 789.989	191 863.107	192 178.078	192 573.044
23	22	200 577.940 <sup>a</sup>	201 529.781	200 577.113 <sup>a</sup>	200 905.313	201 317.746
24	23	209 296.343	210 255.519	209 290.275	209 631.511	210 061.385
25	24	218 014.630	218 964.185	218 002.461	218 356.609	218 803.854
26	25	226 732.746	227 652.903	226 713.682	227 080.543	227 544.975
27	26	235 450.617	236 318.690	235 423.772	235 803.211	236 284.963
28	27	244 168.331	244 958.968	244 132.818	244 524.636	245 023.577
29	28	252 885.887	253 571.479	252 840.703	253 244.748	253 760.717
30	29	261 603.311	262 154.856	261 547.430	261 963.534	262 496.451
31	30	270 320.529	270 708.260	270 253.052	270 680.897	271 231.791
32	31	279 037.620	279 232.105	278 957.203	279 396.720	279 962.773
33	32	287 754.622	287 727.766	287 660.097	288 110.813	288 694.607
34	33	296 471.734	296 199.254	296 361.967	296 824.183	297 424.153
35	34	305 188.310	304 649.763	305 062.223	305 535.487	306 152.116
36	35	313 904.998	313 084.650	313 760.953	314 244.899	314 878.144
37	36	322 621.009	321 509.320	322 458.384	322 952.760	323 602.325
38	37	331 337.282	329 929.323	331 154.531	331 658.794	332 324.862
39	38	340 052.790	338 348.803	339 848.777	340 363.324	<sup>b</sup>
40	39	348 767.954	346 771.793	348 541.475	349 065.775	<sup>b</sup>
41	40	357 482.199	355 200.745	357 232.817	357 766.597	<sup>b</sup>
42	41					
sequence		V017	V137	V082	V030	V040

Notes. <sup>(a)</sup> Calculated from a  $J(J+1)$  power series fit to the sequence. <sup>(b)</sup> Not measured owing to the appearance of additional small doubling and blending with another sequence.

Table A.5. continued.

		(e) $v_b = 0, m = 3U, E_{\text{vib}} = 79.7 \text{ cm}^{-1}$			$v_b = 0, m = 4,$ $140.6 \text{ cm}^{-1}$	$v_b = 0, m = -5,$ $217.5 \text{ cm}^{-1}$ .
$K =$		0	-1	2	0	0
$J'$	$J''$					
1	0	8722.930			8737.510	8755.450
2	1	17 445.790	17 454.140		17 474.880	17 510.750
3	2	26 168.670	26 181.160	26 217.200	26 212.280	26 265.930
4	3	34 891.510	34 907.990	34 956.060	34 949.500	35 021.170
5	4	43 614.169	43 634.803	43 694.834	43 686.558	43 776.052
6	5	52 337.008	52 361.126	52 433.136	52 423.467	52 530.822
7	6	61 059.598	61 087.316	61 171.238	61 160.109	61 285.235
8	7	69 782.154	69 813.257	69 909.074	69 896.532	70 039.333
9	8	78 504.575	78 538.859	78 646.527	78 632.611	78 793.106
10	9	87 226.921	87 264.103	87 383.509	87 368.415	87 546.486
11	10	95 949.108	95 988.904	96 120.050	96 103.815	96 299.372
12	11	104 671.232	104 713.296	104 856.074	104 838.731	105 051.763
13	12	113 393.159	113 437.179	113 591.533	113 573.462	113 803.590
14	13	122 115.041	122 160.503	122 326.370	122 307.385	122 554.987
15	14	130 836.609	130 883.320	131 060.695	131 040.907	131 305.539
16	15	139 558.099	139 605.335	139 793.874 <sup>a</sup>	139 773.828	140 055.353
17	16	148 279.376	148 326.896	148 526.393	148 506.076	148 804.383
18	17	157 000.493	157 047.593	157 258.419	157 237.942	157 552.953
19	18	165 721.632	165 767.724	165 989.446	165 969.028	166 300.585
20	19	174 442.476	174 486.974	174 719.575	174 699.344	175 047.384
21	20	183 163.236	183 205.461	183 448.801	183 429.044	183 793.009
22	21	191 883.717	191 922.912	192 176.926	192 157.781	192 537.886
23	22	200 604.112	200 639.521	200 903.965	200 885.786	201 281.751 <sup>a,b</sup>
24	23	209 324.337	209 355.240	209 630.000	209 612.881	210 024.510 <sup>a,b</sup>
25	24	218 044.534	218 069.900	218 354.946	218 339.144	218 766.186
26	25	226 764.650	226 783.590	227 078.696	227 064.506	227 506.674
27	26	235 484.635	235 496.154	235 801.163	235 788.832	236 245.972
28	27	244 204.559	244 207.596	244 522.386	244 512.199	244 984.016
29	28	252 924.508	252 917.912	253 242.286	253 234.561	253 720.771
30	29	261 644.369	261 626.983	261 960.792	261 955.843	262 456.197
31	30	270 364.327	270 334.789	270 677.907	270 676.015	271 190.307
32	31	279 084.315	279 041.258	279 393.357	279 395.008	279 922.741
33	32	287 804.144	287 746.709 <sup>a</sup>	288 107.240	288 112.677	288 653.970
34	33	296 524.473	296 450.663	296 820.277	296 829.834	297 383.564
35	34	305 244.523	305 153.091	305 531.426	305 545.340	306 111.655
36	35	313 964.548	313 854.002	314 240.338	314 259.408	314 838.069
37	36	322 684.235	322 553.329	322 947.835	322 972.358	323 562.679
38	37	331 404.493	331 251.686	331 653.583	331 683.823	332 285.799
39	38	340 124.133	339 947.987	340 357.652	340 394.140	341 007.079
40	39	348 843.625	348 642.878	349 059.672	349 102.921	349 726.678
41	40	357 562.542	357 335.976	357 760.089	357 810.572	358 444.316
42	41					
sequence		V018	V020	V029	V025	V142

Notes. <sup>(a)</sup> Calculated from a  $J(J+1)$  power series fit to the sequence. <sup>(b)</sup> Not measured owing to blending with another sequence.

Table A.5. continued.

(f)  $v_b = 0$ ,  $m = 0$ ,  $E_{\text{vib}} = 182.2 \text{ cm}^{-1}$ .

$K =$		0	1L	1U
$J'$	$J''$			
1	0	8670.610		
2	1	17 340.960	17 188.670	17 510.450
3	2	26 011.020	25 782.370	26 265.980
4	3	34 680.440	34 376.120	35 019.950
5	4	43 349.173	42 969.421	43 774.035
6	5	52 016.906	51 562.541	52 527.823
7	6	60 683.541	60 155.123	61 280.888
8	7	69 348.900	68 747.151	70 033.282
9	8	78 012.766	77 338.547	78 784.866
10	9	86 674.929	85 929.270	87 535.510
11	10	95 335.299	94 519.235	96 285.169
12	11	103 993.608	103 108.301	105 033.678
13	12	112 649.673	111 696.508	113 781.001
14	13	121 303.479	120 283.613	122 526.957
15	14	129 954.672	128 870.034	131 271.662
16	15	138 603.026	137 454.881	140 014.495
17	16	147 248.768 <sup>a</sup>	146 038.531	148 755.988
18	17	155 891.279	154 621.245	157 495.713
19	18	164 530.700	163 202.325	166 233.670
20	19	173 166.705	171 782.207	174 969.640
21	20	181 799.215	180 360.456 <sup>a</sup>	183 703.515
22	21	190 428.000	188 937.343	192 435.609
23	22	199 053.039	197 512.392	201 165.038
24	23	207 674.136	206 085.904	209 892.319
25	24	216 291.199	214 657.696	218 617.180
26	25	224 904.062	223 227.702	227 339.566
27	26	233 512.629	231 795.913	236 059.320
28	27	242 116.760	240 362.160	244 776.394
29	28	250 716.407	248 926.484	253 490.700
30	29	259 311.510	257 488.850	262 201.998
31	30	267 901.799	266 049.115	270 910.320
32	31	276 487.436	274 607.275	279 615.511
33	32	285 068.035	283 163.366	288 317.636
34	33	293 644.004	291 717.164	297 016.541
35	34	302 214.882	300 268.707	305 712.236
36	35	310 780.705	308 817.997	314 404.000
37	36	319 341.519	317 365.129	323 092.435
38	37	327 897.500	325 909.693	331 777.190 <sup>a</sup>
39	38	336 448.316	334 451.713	340 458.290
40	39	344 993.807	342 991.511	349 135.442
41	40	353 534.354	351 528.890	357 808.901
42	41	362 069.899	360 063.601	
sequence		V094	V127	V132

Notes. <sup>(a)</sup> Calculated from a  $J(J + 1)$  power series fit to the sequence.

**Table A.6.** Line list for CH<sub>3</sub>NCO.

Frequency (MHz)	Error (MHz)	Log(Int) <sup>a</sup>	DR <sup>b</sup>	$E_{\text{low}}$ cm <sup>-1</sup>	$g_{\text{upp}}$ <sup>c</sup>	TAG <sup>d</sup>	QNFMT <sup>e</sup>	QN' <sup>f</sup>				QN'' <sup>g</sup>			
60 688.210	0.0500	-5.0017	3	6.0737	15	01	404	7	0	7	0	6	0	6	0
69 353.880	0.0500	-4.8323	3	8.0980	17	01	404	8	0	8	0	7	0	7	0
78 017.953	0.0500	-4.6840	3	10.4114	19	01	404	9	0	9	0	8	0	8	0
86 680.190	0.0500	-4.5525	3	13.0138	21	01	404	10	0	10	0	9	0	9	0
95 340.443	0.0500	-4.4348	3	15.9051	23	01	404	11	0	11	0	10	0	10	0
103 998.481	0.0500	-4.3284	3	19.0854	25	01	404	12	0	12	0	11	0	11	0
112 654.059	0.0500	-4.2317	3	22.5544	27	01	404	13	0	13	0	12	0	12	0
121 307.237	0.0500	-4.1434	3	26.3121	29	01	404	14	0	14	0	13	0	13	0

**Notes.** Table following the format of the JPL catalog (see Sect. A.2). <sup>(a)</sup> Base 10 logarithm of the integrated intensity in units of nm<sup>2</sup> MHz at 300 K. <sup>(b)</sup> Degrees of freedom in the rotational partition function. <sup>(c)</sup> Upper state degeneracy. <sup>(d)</sup> Species tag or molecular identifier. <sup>(e)</sup> Format of the quantum numbers. <sup>(f)</sup> Quantum numbers for the upper state. <sup>(g)</sup> Quantum numbers for the lower state. This table is available in its entirety at the CDS. A portion is shown here for guidance regarding its form and content.

**Table A.7.** Comparison of rotational transition frequencies for CH<sub>3</sub>NCO between those reported in Halfen et al. (2015) and in this work.

$J'$	$K'_a$	$K'_c$	$J''$	$K''_a$	$K''_c$	Symm.	$m$	Halfen et al. (2015)	This work	Difference
<b>measured</b>										
7	-1	7	6	-1	6	E	1	60 029.044	60 029.019	0.025
7	1	6	6	1	5	A	0	60 160.932	60 162.076	-1.144 <sup>a</sup>
7	0	7	6	0	6	A	0	60 688.191	60 688.210	-0.019
7	0	7	6	0	6	E	1	60 833.422	60 834.588	-1.166 <sup>a</sup>
7	1	7	6	1	6	A	0	61 260.729	61 260.734	-0.001
8	-1	8	7	-1	7	E	1	68 617.550	68 618.612	-1.062 <sup>a</sup>
8	1	7	7	1	6	A	0	68 753.890	68 755.025	-1.135 <sup>a</sup>
8	0	8	7	0	7	A	0	69 353.888	69 353.880	0.008
8	0	8	7	0	7	E	1	69 469.196	69 470.354	-1.154 <sup>a</sup>
8	1	8	7	1	7	A	0	70 009.179	70 010.208	-1.029 <sup>a</sup>
9	1	8	8	1	7	E	1	77 107.478 <sup>b</sup>	77 101.788	5.690
9	-1	9	8	-1	8	E	1	77 211.707	77 212.768	-1.061 <sup>a</sup>
9	1	8	8	1	7	A	0	77 347.355	77 347.425	-0.070
9	0	9	8	0	8	A	0	78 017.932	78 017.953	-0.021
9	0	9	8	0	8	E	1	78 087.673	78 087.660	0.013
9	1	9	8	1	8	A	0	78 758.868	78 758.849	0.019
10	-1	10	9	-1	9	E	1	85 811.557	85 811.546	0.011
10	1	9	9	1	8	A	0	85 938.967	85 938.962	0.005
10	0	10	9	0	9	A	0	86 680.195	86 680.190	0.005
10	0	10	9	0	9	E	1	86 686.575	86 686.556	0.019
10	1	10	9	1	9	A	0	87 506.605	87 506.607	-0.002
<b>calculated</b>										
8	1	7	7	1	6	E	1	68 536.76 <sup>c</sup>	68 532.241	4.519
10	1	9	9	1	8	E	1	85 679.63 <sup>c</sup>	85 672.565	7.065
11	1	10	10	1	9	E	1	94 253.49 <sup>c</sup>	94 244.905	8.585
12	1	11	11	1	10	E	1	102 829.92 <sup>c</sup>	102 819.142	10.778

**Notes.** <sup>(a)</sup> One of seven lines from Halfen et al. (2015) showing  $a \geq 1$  MHz frequency shift relative to the present work. Other lines in the same transition sequences measured in Halfen et al. (2015) do not seem to be affected. <sup>(b)</sup> This is a bona fide line in our experimental spectrum but our assignment is  $m = -2$ ,  $K = 2$  with measured frequency of 77 107.514 MHz. <sup>(c)</sup> Prediction in Halfen et al. (2015) based on the misassigned 77 107.478 MHz line. There are no lines in our experimental spectrum at these frequencies, and the actual  $K = +1$ ,  $m = 1$  lines are at significantly lower frequencies.

**Table A.8.** Calculated frequencies and relative intensities of nuclear quadrupole splitting components for the  $K_a = 0,1,2$  ground state ( $v_b = 0$ ,  $m = 0$ ) rotational transitions of CH<sub>3</sub>NCO.

$K = 0$			$K = 1L$			$K = 1U$			$K = 2L$			$K = 2U$		
$F'-F''$	$\nu^a$ / MHz	$I_{rel}^b$	$F'-F''$	$\nu$ / MHz	$I_{rel}$	$F'-F''$	$\nu$ / MHz	$I_{rel}$	$F'-F''$	$\nu$ / MHz	$I_{rel}$	$F'-F''$	$\nu$ / MHz	$I_{rel}$
<b><math>J = 1-0</math></b>														
0-1	8669.943	0.1111												
2-1	8671.222	0.5555												
1-1	8672.076	0.3334												
<b><math>J = 2-1</math></b>														
1-1	17 341.104	0.0833	1-0	17 189.333	0.1111	1-0	17 503.509	0.1111						
1-2	17 341.957	0.0056	1-2	17 189.916	0.0056	1-2	17 504.205	0.0056						
3-2	17 342.465	0.4667	3-2	17 190.192	0.4667	3-2	17 504.436	0.4667						
2-1	17 342.526	0.2500	1-1	17 190.305	0.0833	1-1	17 504.669	0.0833						
1-0	17 343.237	0.1111	2-2	17 190.690	0.0833	2-2	17 504.853	0.0833						
2-2	17 343.379	0.0833	2-1	17 191.079	0.2500	2-1	17 505.317	0.2500						
<b><math>J = 3-2</math></b>														
2-2	26 012.000	0.0370	2-2	25 784.511	0.0370	2-2	26 255.928	0.0370	2-1	26 037.145	0.2000	2-1	26 037.736	0.2000
2-3	26 012.914	0.0011	2-3	25 785.008	0.0011	2-3	26 256.344	0.0011	3-3	26 037.653	0.0370	3-3	26 038.244	0.0370
4-3	26 013.246	0.4286	4-3	25 785.272	0.4286	2-1	26 256.576	0.2000	4-3	26 037.653	0.4286	4-3	26 038.244	0.4286
3-2	26 013.280	0.2963	2-1	25 785.285	0.2000	4-3	26 256.578	0.4286	2-3	26 037.653	0.0011	2-3	26 038.244	0.0011
2-1	26 013.422	0.2000	3-2	25 785.527	0.2963	3-2	26 256.831	0.2963	2-2	26 038.567	0.0370	3-2	26 039.158	0.2963
3-3	26 014.194	0.0370	3-3	25 786.025	0.0370	3-3	26 257.247	0.0370	3-2	26 038.567	0.2963	2-2	26 039.158	0.0370
<b><math>J = 4-3</math></b>														
3-3	34 682.204	0.0208	3-3			3-3			3-3	34 716.569	0.0208	3-3	34 718.047	0.0003
3-4	34 683.153	0.0003	3-4	34 379.823	0.0003	3-4	35 008.150	0.0003	3-3	34 716.569	0.0003	3-4	34 718.047	0.0208
5-4	34 683.402	0.4074	5-4	34 380.045	0.4074	5-4	35 008.351	0.4074	3-4	34 716.669	0.4074	5-4	34 718.146	0.4074
4-3	34 683.424	0.3125	3-2	34 380.086	0.2381	3-2	35 008.384	0.2381	5-4	34 716.669	0.4074	5-4	34 718.146	0.4074
3-2	34 683.484	0.2381	4-3	34 380.160	0.3125	4-3	35 008.463	0.3125	4-3	34 717.057	0.3125	4-3	34 718.534	0.0208
4-4	34 684.372	0.0208	4-4	34 380.912	0.0208	4-4	35 009.132	0.0208	4-4	34 717.057	0.0208	4-4	34 718.534	0.3125
<b><math>J = 5-4</math></b>														
4-4	43 351.569	0.0133	4-4	42 973.421	0.0133	4-4	43 758.741	0.0133	4-4	43 394.804	0.0133	4-4	43 397.758	0.0133
4-5	43 352.539	0.0001	4-5	42 974.288	0.0001	4-5	43 759.523	0.0001	4-5	43 395.192	0.0001	4-5	43 398.145	0.0001
6-5	43 352.740	0.3939	6-5	42 974.477	0.3939	6-5	43 759.694	0.3939	4-3	43 395.292	0.2593	4-3	43 398.245	0.2593
5-4	43 352.755	0.3200	4-3	42 974.511	0.2593	4-3	43 759.723	0.2593	6-5	43 395.312	0.3939	6-5	43 398.265	0.3939
4-3	43 352.788	0.2593	5-4	42 974.540	0.3200	5-4	43 759.755	0.3200	5-4	43 395.515	0.3200	5-4	43 398.466	0.3200
5-5	43 353.725	0.0133	5-5	42 975.407	0.0133	5-5	43 760.537	0.0133	5-5	43 395.903	0.0133	5-5	43 398.856	0.0133
<b><math>J = 6-5</math></b>														
5-5	52 019.907	0.0093	5-5	51 567.406	0.0093	5-5	52 509.526	0.0093	5-5	52 072.829	0.0093	5-5	52 077.994	0.0093
5-6	52 020.892	0.0001	5-6	51 568.335	0.0001	5-6	52 510.369	0.0001	5-6	52 073.419	0.0001	5-6	52 078.584	0.0001
7-6	52 021.060	0.3846	7-6	51 568.499	0.3846	7-6	52 510.517	0.3846	7-6	52 073.539	0.3846	7-6	52 078.704	0.3846
6-5	52 021.071	0.3241	5-4	51 568.525	0.2727	5-4	52 510.540	0.2727	5-4	52 073.540	0.2727	5-4	52 078.705	0.2727
5-4	52 021.092	0.2727	6-5	51 568.538	0.3241	6-5	52 510.555	0.3241	6-5	52 073.660	0.3241	6-5	52 078.824	0.3241
6-6	52 022.056	0.0093	6-6	51 569.467	0.0093	6-6	52 511.398	0.0093	6-6	52 074.250	0.0093	6-6	52 079.415	0.0093
<b><math>J = 7-6</math></b>														
6-6	60 687.022	0.0068	6-6	60 160.922	0.0068	6-6	61 259.710	0.0068	6-6	60 750.459	0.0068	6-6	60 758.718	0.0068
6-7	60 688.018	0.0000	6-7	60 161.890	0.0000	6-7	61 260.590	0.0000	6-7	60 751.170	0.0000	6-7	60 759.428	0.0000
8-7	60 688.163	0.3778	8-7	60 162.034	0.3778	8-7	61 260.721	0.3778	8-7	60 751.284	0.3778	8-7	60 759.542	0.3778
7-6	60 688.171	0.3265	6-5	60 162.054	0.2820	6-5	61 260.739	0.2821	6-5	60 751.290	0.2821	6-5	60 759.548	0.2821
6-5	60 688.186	0.2821	7-6	60 162.060	0.3265	7-6	61 260.746	0.3265	7-6	60 751.361	0.3265	7-6	60 759.619	0.3265
7-7	60 689.167	0.0068	7-7	60 163.028	0.0068	7-7	61 261.627	0.0068	7-7	60 752.072	0.0068	7-7	60 760.330	0.0068
<b><math>J = 8-7</math></b>														
7-7	69 352.717	0.0052	7-7	68 753.883	0.0052	7-7	70 009.183	0.0052	7-7	69 427.576	0.0052	7-7	69 439.955	0.0052
7-8	69 353.721	0.0000	7-8	68 754.877	0.0000	7-8	70 010.088	0.0000	7-8	69 428.365	0.0000	7-8	69 440.743	0.0000
9-8	69 353.849	0.3725	9-8	68 755.005	0.3725	9-8	70 010.205	0.3726	9-8	69 428.471	0.3726	9-8	69 440.848	0.3725
8-7	69 353.855	0.3281	7-6	68 755.021	0.2889	7-6	70 010.219	0.2889	7-6	69 428.479	0.2889	7-6	69 440.856	0.2889
7-6	69 353.866	0.2889	8-7	68 755.024	0.3281	8-7	70 010.223	0.3281	8-7	69 428.524	0.3281	8-7	69 440.902	0.3281
8-8	69 354.860	0.0052	8-8	68 756.018	0.0052	8-8	70 011.128	0.0052	8-8	69 429.313	0.0052	8-8	69 441.690	0.0052
<b><math>J = 9-8</math></b>														
8-8	78 016.793	0.0041	8-8	77 346.206	0.0041	8-8	78 757.837	0.0041	8-8	78 104.085	0.0041	8-8	78 121.752	0.0041
8-9	78 017.805	0.0000	8-9	77 347.220	0.0000	8-9	78 758.761	0.0000	8-9	78 104.927	0.0000	8-9	78 122.593	0.0000
10-9	78 017.918	0.3684	10-9	77 347.334	0.3684	10-9	78 758.866	0.3684	10-9	78 105.026	0.3684	10-9	78 122.692	0.3685
8-7	78 017.924	0.3292	8-7	77 347.347	0.2941	8-7	78 758.877	0.2941	8-7	78 105.033	0.2941	8-7	78 122.699	0.2941
9-8	78 017.932	0.2941	9-8	77 347.348	0.3292	9-8	78 758.879	0.3292	9-8	78 105.064	0.3292	9-8	78 122.730	0.3292
9-9	78 018.935	0.0041	9-9	77 348.361	0.0041	9-9	78 759.803	0.0041	9-9	78 105.906	0.0041	9-9	78 123.571	0.0041

**Notes.** <sup>(a)</sup> Calculated frequency with uncertainty estimated at 5 kHz. <sup>(b)</sup> Relative intensity of a given hyperfine component such that the sum over all components for this rotational transition is unity.

## Appendix B: Astrophysical methods

### B.1. The Orion BN/KL region

Orion BN/KL (Becklin-Neugebauer/Kleinmann-Low; Becklin & Neugebauer 1967; Kleinmann & Low 1967) is the closest (about 414 pc; Menten et al. 2007) region exhibiting several processes related to young stellar objects (YSOs) and high-mass star formation (Genzel & Stutzki 1989). This region is located at the core of the Orion molecular cloud 1 (OMC1) which lies behind the Orion Nebula cluster (O'Dell 2001). Infrared facilities and radio telescopes can observe inside dusty regions where the formation of stars or their associated violent phenomena take place, providing very useful information about these processes. Near- and mid-IR subarcsecond resolution imaging and (sub)millimetre interferometric observations have identified the main sources of luminosity, heating, and dynamics in the region. At first, IRc2 was proposed as the main source of luminosity, heating, and dynamics within the region (Wynn-Williams et al. 1984). However, the detection of two radio continuum sources, *B* (coincident with the *BN* object which was resolved with high spatial resolution at 7 mm; Rodríguez et al. 2009) and *I* (centroid of the SiO masers and located 0.5'' south of IRc2; Menten & Reid 1995) revealed that the intrinsic IR luminosity of IRc2 ( $L \sim 1000 L_{\odot}$ ) is only a fraction of the luminosity of the entire system ( $1 \times 10^5 L_{\odot}$ ; Gezari et al. 1998). The radio continuum emission of the IR source *n* was also identified by Menten & Reid (1995) (3'' south-west from source *I*), suggesting this source as another precursor of the large-scale phenomena. In addition, several IR and millimetre continuum sources have been identified (Shuping et al. 2004; Wu et al. 2014). Thus, the core of Orion KL contains at least three self-luminous objects (protostars), the compact HII regions *I*, *n* (see Figs. 3 and B.3), and *BN*; these sources are within a region of  $\sim 10''$  ( $\sim 0.02$  pc). Their proper motions reveal that they run away from a common region (Gómez et al. 2005). Different scenarios, as well as the formation of high-mass stars, have been proposed to explain the complexity of this source. An explosion of a multistar system (sources *I*, *n*, and *BN*) that took place  $\sim 500$  years ago has been proposed as the main factor responsible for most of the Orion KL gas components (Zapata et al. 2011).

The different gas components show distinct physical and chemical properties, which can be identified even with single-dish telescopes by a characteristic systemic velocity (Blake et al. 1987; Schilke et al. 2001; Tercero et al. 2010). Classically, these components have been called *Hot Core*, a hot,  $\sim 200$ – $300$  K, and dense clump rich in complex organic saturated *N*-bearing species such as  $\text{CH}_3\text{CH}_2\text{CN}$ , characterized by  $\Delta v_{\text{FWHM}} \sim 5$ – $15 \text{ km s}^{-1}$  and  $v_{\text{LSR}} \sim 5$ – $7 \text{ km s}^{-1}$ ; *Extended Ridge*, the host, quiescent, and relatively cold,  $\sim 60$  K ambient cloud rich in simple species such as CS or HCN, emitting lines with  $\Delta v_{\text{FWHM}} \sim 3$ – $4 \text{ km s}^{-1}$  and  $v_{\text{LSR}} \sim 8$ – $9 \text{ km s}^{-1}$ ; *Compact Ridge*, a warm,  $\sim 150$  K, and compact clump rich in organic saturated O-rich species such as  $\text{CH}_3\text{OCOH}$  or  $\text{CH}_3\text{OCH}_3$ , whose spectral features are characterized by  $\Delta v_{\text{FWHM}} \sim 2$ – $3 \text{ km s}^{-1}$  and  $v_{\text{LSR}} \sim 7$ – $8 \text{ km s}^{-1}$ ; and *Plateau*, molecular outflows presenting typical shock chemistry with molecules such as SO or SiO (Goicoechea et al. 2015); the low velocity flow (oriented along the SW-NE direction and probably driven by source *I*) is characterized by lines with  $\Delta v_{\text{FWHM}} \sim 20 \text{ km s}^{-1}$  and  $v_{\text{LSR}} \sim 5$ – $6 \text{ km s}^{-1}$ , whereas the high-velocity flow (oriented along the SE-NW direction and whose origin could be the explosive event caused by the dynamical decay of a multi-star system briefly described above) presents lines with  $\Delta v_{\text{FWHM}}$  as wide as  $150 \text{ km s}^{-1}$  and  $v_{\text{LSR}} \sim 10 \text{ km s}^{-1}$ . Interferometric observations

have shown other cloud components inside Orion BN/KL such as the millimetre continuum sources MM2, MM4 (which corresponds approximately to Position B, see Figs. 3 and B.3), MM5, and MM6 (Wu et al. 2014). In addition, these latter observations reveal the hot core to be a collection of very dense and hot clumps presenting different chemistry and radial velocities (Favre et al. 2011; Tercero et al. 2015). Position A of Figs. 3 and B.3 is located in the middle of the hot core clumpy structure.

### B.2. Observations

#### B.2.1. IRAM 30 m

We performed a sensitive, fully single side band reduced, line survey towards Orion IRc2 with the IRAM 30 m telescope over broad frequency ranges (total frequency coverage of  $\sim 168$  GHz; Tercero et al. 2010). Our main goal was to obtain a deep insight into the molecular content and chemistry of Orion BN/KL and to improve our knowledge of its prevailing physical conditions. It also allows us to search for new molecular species and new isotopologues, as well as the rotational emission of vibrationally excited states of molecules already known to exist in this source (see Sect. B.3 and main text).

The line survey was performed over three millimetre-wave windows (3, 2, and 1.3 mm, covering frequency ranges 80–115.5 GHz, 130–178 GHz, and 197–281 GHz, respectively) with the IRAM 30 m telescope. The observations were carried out between September 2004 and January 2007 pointing toward the IRc2 source at  $\alpha_{2000.0} = 5^{\text{h}}35^{\text{m}}14^{\text{s}}.5$ ,  $\delta_{2000.0} = -5^{\circ}22'30''.0$ . Four SiS receivers were used simultaneously, with image sideband rejections within  $\sim 13$  dB (1.3 mm receivers), 12–16 dB (2 mm receivers), and 20–27 dB (3 mm receivers). The observations were performed using the wobbler switching mode with a beam throw in azimuth of  $\pm 120''$ . No contamination from the off position affected our observations, except for a marginal amount at the lowest elevations ( $25^{\circ}$ ) for molecules showing low-*J* emission along the ambient molecular cloud. System temperatures were in the range of 100–800 K from the lowest to the highest frequencies. For the spectra between 172–178 GHz, the system temperature was significantly higher, 1000–4000 K, owing to proximity of the atmospheric water line at 183.31 GHz. The intensity scale was calibrated using the atmospheric transmission model (ATM; Pardo et al. 2001; Cernicharo 1985). Focus and pointing were checked every 1–2 hours on planets or nearby quasars. Backends provided a spectral resolution of 1–1.25 MHz. The half power beam width (HPBW) of the 30m telescope ranged from 31'' to 9'' from 80 to 280 GHz ( $\text{HPBW}[\text{arcsec}] = 2460/\text{Freq.}[\text{GHz}]$ ). The data were reduced using the GILDAS package<sup>1</sup> checking for image sideband contamination and fitting and removing 0–1 order baselines. Figures using these data are shown in main beam temperature ( $T_{\text{MB}}$ ).

#### B.2.2. ALMA SV

The ALMA Science Verification (SV) data were taken in January 2012 towards the IRc2 region in Orion. The observations were carried out with 16 antennas of 12 m in the frequency range from 213.715 to 246.627 GHz (Band 6). The primary beam was  $\sim 27''$ . Spectral resolution was 0.488 MHz

<sup>1</sup> <http://www.iram.fr/IRAMFR/GILDAS>

( $\sim 0.64 \text{ km s}^{-1}$  in the observed frequency range). The observations were centred on coordinates:  $\alpha_{J2000} = 05^{\text{h}}35^{\text{m}}14^{\text{s}}.35$ ,  $\delta_{J2000} = -05^{\circ}22'35''00$ . The CASA software<sup>2</sup> was used for initial processing, and then the visibilities were exported to the GILDAS package for further analysis. The synthesized beam ranged from  $2''.00 \times 1''.48$  with a PA of  $176^{\circ}$  at 214.0 GHz to  $1''.75 \times 1''.29$  with a PA of  $164^{\circ}$  at 246.4 GHz. The brightness temperature to flux density conversion factor is 9 K for 1 Jy per beam. The continuum emission was subtracted in the maps by carefully selecting line-free channels.

### B.3. Astronomical model

#### B.3.1. Orion KL

Frequency predictions and intensities reported in this work were implemented in MADEX (Cernicharo 2012) to model the emission of  $\text{CH}_3\text{NCO}$  and to search for it toward Orion KL. MADEX is an excitation and radiative transfer code which includes more than 5200 molecular species with accurate spectroscopy. To derive the physical parameters shown in Table B.1, we performed a model that reproduces more line profiles more accurately from transitions covering a wide energy range within a  $\sim 30\%$  of the uncertainty in line intensity (red lines in Figs. 2 and B.1).

Owing to the lack of collisional rates for this molecule, we used LTE approximation. Nevertheless, taking into account the physical conditions of the considered components of the cloud (see Table B.2), we expect that this approximation works reasonably well (see e.g. Fortman et al. 2012). For each spectral component, we assume uniform physical conditions of the cloud (line width, radial velocity, and source size with uniform brightness temperature and optical depth over this size), which we choose by taking into account the parameters obtained from Gaussian fits of the line profiles and the emission shown by the ALMA maps. To fit the IRAM 30 m lines, we also considered the beam coupling effects adding the offset position with respect to IRc2 (the pointing position). Corrections for beam dilution are also applied for each line depending on the different beam sizes at different frequencies. Therefore, we fixed all of the above parameters leaving only the rotational temperature and the column density as free parameters for each component. In order to determine the uncertainty of the values of column density and of temperature, we ran several models varying only the values for these parameters and fixing the rest. To fit the ALMA data we extracted the averaged spectrum over  $5 \times 5$  pixels ( $\sim 1'' \times 1''$ ) around Position A and Position B (see Figs. 3 and B.3). To derive the column densities and relative abundances of the species shown in Table B.1, we adopted the same model of  $\text{CH}_3\text{NCO}$  for each position varying the column density for each one of the species of Table B.1. In Fig. B.1, a model containing all species already studied in the IRAM 30 m survey is included (cyan line). The molecules considered in the models and references to their modelling and analysis are given in Table B.3. This table also summarizes the works performed to date based on the 30 m data and devoted to mitigating the number of unidentified lines in the IRAM 30 m survey of Orion (especially those in collaboration with spectroscopy laboratories), to searching for new molecular species in interstellar clouds, and to improving the knowledge of the physical-chemical properties of Orion KL.

#### B.3.2. Sgr B2(N)

We have searched in published line surveys of Sgr B2 and W51 for  $\text{CH}_3\text{NCO}$ . We find that 21 unidentified features above  $13\sigma$  found in Sgr B2 by Belloche et al. (2013) can be unambiguously assigned to  $\text{CH}_3\text{NCO}$ . However, in the PRIMOS data (Neill et al. 2012) of the same source the assignment is not obvious.  $\text{CH}_3\text{NCO}$  was also reported in Sgr B2 during the submission process of this work (Halfen et al. 2015). We used MADEX and the public data of Sgr B2(N) provided by Belloche et al. (2013) to derive the rotational temperature and column density of methyl isocyanate in this source (see Fig. B.2, red line). We find that the two hot ( $T_{\text{rot}} = 200 \text{ K}$ ) and compact ( $d_{\text{sou}} \approx 2''$ ) components derived by Belloche et al. (2013) for HNC0 are enough to reproduce all lines that appear at 3 mm. We derive column densities of  $N = 5 \times 10^{17} \text{ cm}^{-2}$  for the  $63 \text{ km s}^{-1}$  component and  $3 \times 10^{17} \text{ cm}^{-2}$  for the second component at  $73 \text{ km s}^{-1}$  (assuming  $\Delta v_{\text{FWHM}} = 7 \text{ km s}^{-1}$ , see Belloche et al. 2013).

In W51 (Pulliam et al. 2012), another well-known hot core with similar molecular content than Orion, we do not find an obvious detection in the data, because the lines are weaker owing to the higher distance of W51 compared to Orion.

Methyl isocyanate turns out to be one of the prominent molecules in hot cores and it is surprising to realize that it is present in many line surveys. It was only the lack of suitable laboratory data delayed its discovery. In the present work it is the close collaboration between astronomers and molecular physicists that has made such detailed characterization of this new molecular species possible.

#### B.4. Spatial distribution in Orion

The spatial distribution of several molecules detected in Orion KL is shown in Figs. 3 and B.3. Despite the lack of short spacing data required for completion of the possible extended emission of some of these species (see e.g.  $\text{CH}_3\text{OH}$  or  $\text{DCN}$ ), we can obtain an overview of the main cores that host these species. Moreover, the discussion has to address the large differences in energies of the upper level for the transitions involved in those maps (it is not possible to find transitions with similar energies of, for instance,  $\text{DCN}$  and  $\text{HC}_3\text{N } v_7 = 1$  between 213.7–247.5 GHz, the coverage of the ALMA SV data). In addition, owing to the extreme complexity of Orion KL, it is not straightforward to find lines free of blending with other species in the whole region: many lines of a large variety of molecules that appear unblended in some cores, overlap with lines of other species in the average spectrum of the region. This makes it more difficult to derive maps of lines involving transitions with uniform upper level energies. Nevertheless, by taking these restrictions into account, the discussion can be focused on the main differences/similarities found for the different “families” of molecules.

As we have pointed out in the main text, we note a similar spatial distribution for  $\text{CH}_3\text{NCO}$ ,  $\text{NH}_2\text{CHO}$ , and HNC0. The main differences of these maps are a larger extension of HNC0 due to its higher abundance and the lack of the clump in the NW of Position B for  $\text{NH}_2\text{CHO}$ ; in addition,  $\text{CH}_3\text{NCO}$  does not emit in this region, whereas HNC0 and  $\text{NH}_2\text{CHO}$  show some emission at the position of the compact ridge. It is worth noting that these species are the only three detected in Orion KL containing nitrogen, oxygen, carbon, and hydrogen together.

Following with the compact ridge, this component is the main host of  $\text{CH}_3\text{OCH}_3$ ,  $\text{CH}_3\text{OCOH}$ , and  $\text{CH}_2\text{OCH}_2$ , all of them

<sup>2</sup> <http://casa.nrao.edu>

**Table B.1.** Molecular abundances in Orion and in Comet 67P/Churyumov-Gerasimenko.

Species	Comet	Orion Position A		Orion Position B	
	Abundance rel. to H <sub>2</sub> O	Column density (cm <sup>-2</sup> )	Abundance rel. to H <sub>2</sub> O (× 100)	Column density (cm <sup>-2</sup> )	Abundance rel. to H <sub>2</sub> O (× 100)
H <sub>2</sub> O <sup>a</sup>	100	$(3 \pm 1) \times 10^{19}$	100	$(2.0 \pm 0.6) \times 10^{19}$	100
HCN <sup>a</sup>	0.9	$(4 \pm 1) \times 10^{17}$	1.3	$(2.0 \pm 0.6) \times 10^{17}$	1.0
CO <sup>b</sup>	1.2	$(4 \pm 1) \times 10^{19}$	130	$(1.0 \pm 0.3) \times 10^{19}$	50
CH <sub>3</sub> NH <sub>2</sub>	0.6	$\leq(4 \pm 1) \times 10^{15}$	$\leq 0.01$	$(4 \pm 1) \times 10^{15}$	0.02
CH <sub>3</sub> CN <sup>c</sup>	0.3	$(7 \pm 3) \times 10^{16}$	0.2	$(1.0 \pm 0.3) \times 10^{17}$	0.5
HNCO	0.3	$(1.0 \pm 0.3) \times 10^{17}$	0.3	$(7 \pm 3) \times 10^{16}$	0.35
CH <sub>3</sub> CHO	0.5	$(1.6 \pm 0.5) \times 10^{15}$	0.005	$(1.4 \pm 0.3) \times 10^{15}$	0.0075
HCONH <sub>2</sub>	1.8	$(4 \pm 1) \times 10^{15}$	0.01	$(7 \pm 3) \times 10^{14}$	0.0035
CH <sub>3</sub> CH <sub>2</sub> NH <sub>2</sub> <sup>d</sup>	0.3	$\leq(4 \pm 1) \times 10^{14}$	$\leq 0.001$	$\leq(2 \pm 1) \times 10^{14}$	$\leq 0.001$
CH <sub>3</sub> NCO	1.3	$(7 \pm 3) \times 10^{15}$	0.02	$(4 \pm 1) \times 10^{15}$	0.02
CH <sub>3</sub> COCH <sub>3</sub>	0.3	$(1.4 \pm 0.4) \times 10^{16}$	0.04	$(1.1 \pm 0.3) \times 10^{16}$	0.055
CH <sub>3</sub> CH <sub>2</sub> CHO <sup>d</sup>	0.1	$\leq(1.0 \pm 0.3) \times 10^{15}$	$\leq 0.003$	$\leq(1.0 \pm 0.3) \times 10^{15}$	$\leq 0.005$
CH <sub>3</sub> CONH <sub>2</sub>	0.7	$(1.2 \pm 0.4) \times 10^{15}$	0.004	$\leq(3 \pm 1) \times 10^{14}$	$\leq 0.0015$
CH <sub>2</sub> OHCHO	0.4	$(7 \pm 3) \times 10^{14}$	0.002	$\leq(4 \pm 1) \times 10^{14}$	$\leq 0.002$
OHCH <sub>2</sub> CH <sub>2</sub> OH	0.2	$(9 \pm 3) \times 10^{15}$	0.03	$\leq(1.0 \pm 0.3) \times 10^{15}$	$\leq 0.005$
CH <sub>3</sub> OH		$(3 \pm 1) \times 10^{18}$	10	$(9 \pm 3) \times 10^{17}$	4.5
CH <sub>3</sub> OCOH		$(9 \pm 3) \times 10^{16}$	0.3	$(6 \pm 2) \times 10^{16}$	0.3
CH <sub>3</sub> COOH		$(1.0 \pm 0.3) \times 10^{16}$	0.03	$\leq(3 \pm 1) \times 10^{15}$	$\leq 0.015$
CH <sub>3</sub> CH <sub>2</sub> CN		$(3 \pm 1) \times 10^{16}$	0.1	$(3 \pm 1) \times 10^{16}$	0.15

**Notes.** <sup>(a)</sup> [D]/[H] = 0.003; from [HDO]/[H<sub>2</sub>O] (Neill et al. 2013); <sup>(b)</sup> [<sup>16</sup>O]/[<sup>18</sup>O] = 250; from [<sup>16</sup>OCS]/[<sup>18</sup>OCS] (Tercero et al. 2010); <sup>(c)</sup> [<sup>12</sup>C]/[<sup>13</sup>C] = 45 (Tercero et al. 2010); <sup>(d)</sup> Only the lowest energy conformer, *trans* for CH<sub>3</sub>CH<sub>2</sub>NH<sub>2</sub> and *cis* for CH<sub>3</sub>CH<sub>2</sub>CHO.

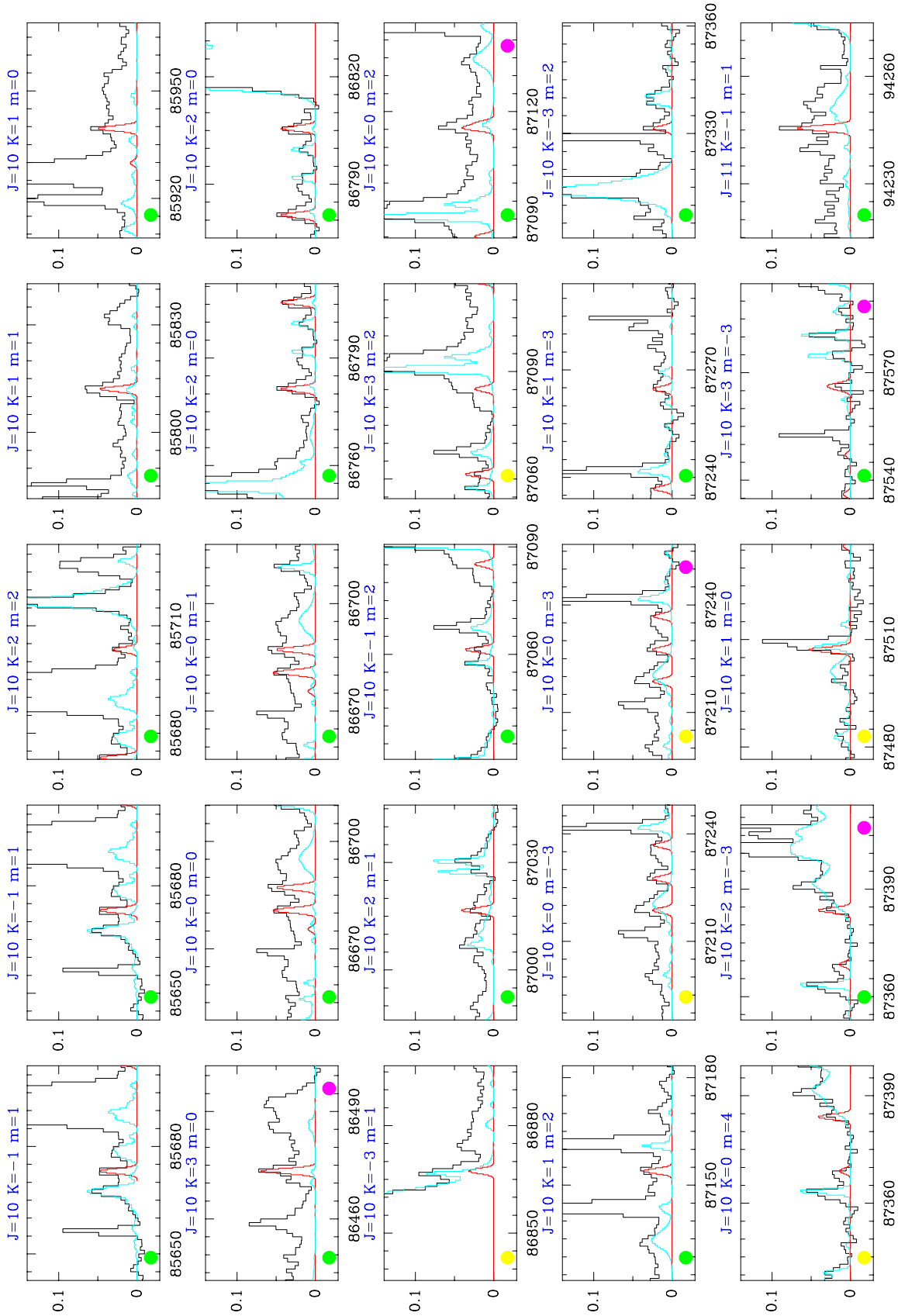
**Table B.2.** Physical parameters of the considered Orion KL cores.

	IRAM 30 m	ALMA SV			
		Position A		Position B	
		Comp. 1	Comp. 2	Comp. 1	Comp. 2
$v_{\text{LSR}}$ (km s <sup>-1</sup> )	7	8	6	8	5
$\Delta v_{\text{FWHM}}$ (km s <sup>-1</sup> )	5	3	8	3	3
$d_{\text{sou}}$ (")	8	3	3	3	3
<i>offset</i> (")	5	...	...	...	...
$T_{\text{rot}}$ (K)	150 ± 50	150 ± 50	150 ± 50	150 ± 50	150 ± 50
$N(\text{CH}_3\text{NCO})$ (cm <sup>-2</sup> )	$(5 \pm 2) \times 10^{15}$	$(5 \pm 2) \times 10^{15}$	$(2.5 \pm 0.7) \times 10^{15}$	$(2.5 \pm 0.7) \times 10^{15}$	$(1.7 \pm 0.5) \times 10^{15}$

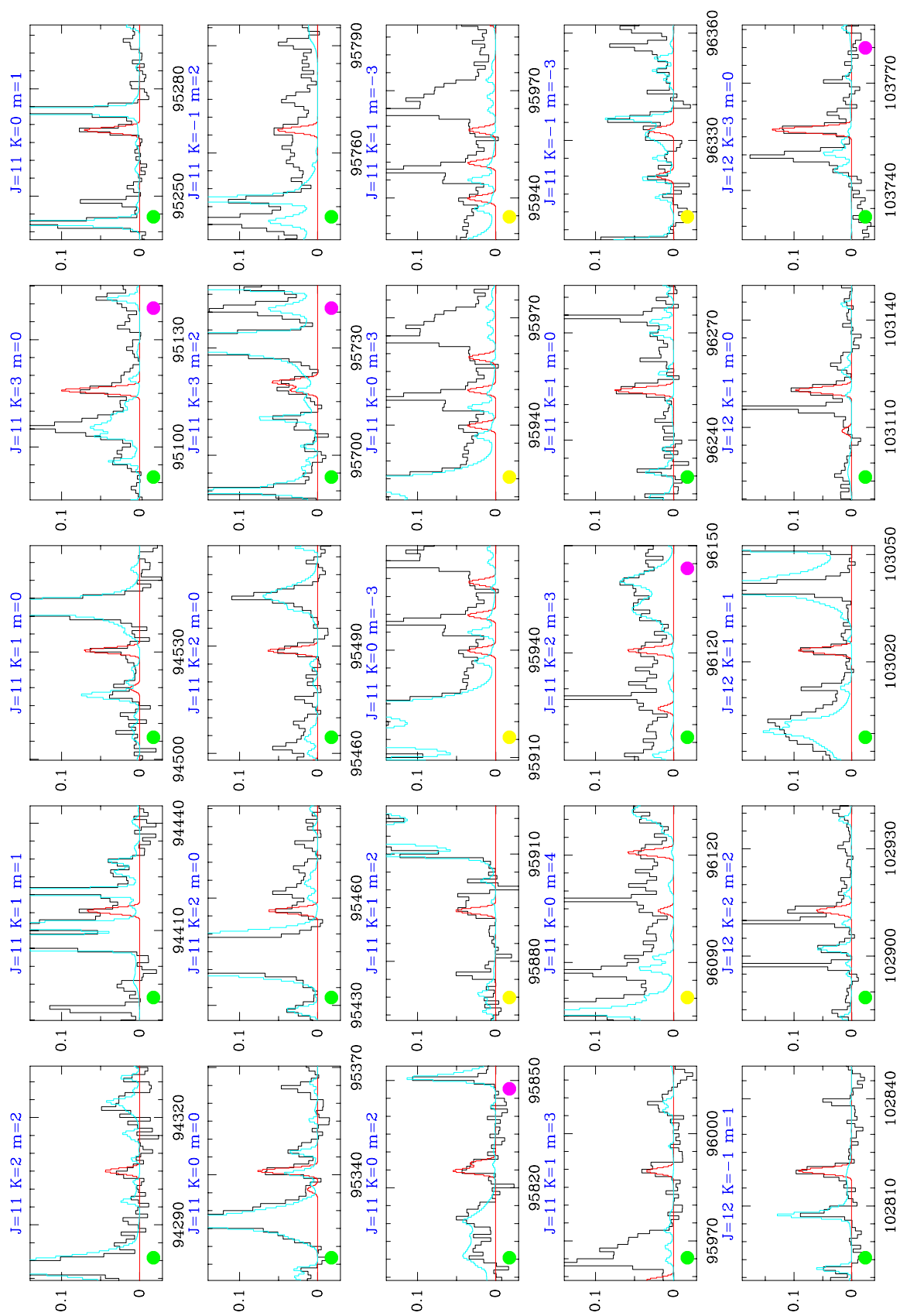
organic compounds containing oxygen. Molecules that we could naively think that are related with them, such as CH<sub>3</sub>CH<sub>2</sub>OH, CH<sub>3</sub>COCH<sub>3</sub>, CH<sub>3</sub>COOH, OHCH<sub>2</sub>CH<sub>2</sub>OH, and CH<sub>2</sub>OHCHO, present a completely different spatial distribution (Guélin et al. 2008; Peng et al. 2012, 2013; Widicus Weaver & Friedel 2012; Friedel & Widicus Weaver 2012; Brouillet et al. 2015; Feng et al. 2015; Tercero et al. 2015). Although there are some remarkable differences in the emission of the latter species, we observe the main core located at the SE of source *n* (at the middle-south of the hot core). Abundant species in the region such as DCN, HDO, and CH<sub>3</sub>CN do not show significant emission at the compact ridge.

On the other hand, complex species with nitrogen such as CH<sub>3</sub>CH<sub>2</sub>CN, CH<sub>2</sub>CHCN, and HC<sub>3</sub>N, present their emission at the north of the hot core. In addition, emission at the NE of source *l* is more prominent for these species (Guélin et al. 2008; Widicus Weaver & Friedel 2012; Friedel & Widicus Weaver 2012).

Finally, although we do not discuss the emission peaks of CH<sub>3</sub>OH (methanol, one of the most abundant species), because they could be affected by opacity effects, we note that methanol is ubiquitous in the region.



**Fig. B.1.** Lines of CH<sub>3</sub>NCO (here and the next 15 plots) observed with the IRAM 30 m telescope and with ALMA (black filled circle in the middle bottom of each panel). The lines are ordered by frequency. The red lines correspond to the CH<sub>3</sub>NCO model simulation for both sets of data (see text). The cyan lines correspond to the emission of all modelled molecules to date for the 30m data (see Table B.3). Green filled circles at the bottom left of each panel identify unblended lines, while yellow ones mark lines blended with similar intensity lines from other species. Nevertheless, in the latter case each line profile can be still fitted with a Gaussian profile providing a frequency and intensity for the observed component. Violet filled circles at the bottom right of each panel identify unresolved doublets. The quantum numbers follow the labelling of Table A.5 except for  $m = 0$  for which  $K_c$  is not provided (many of these lines are unresolved doublets). The complete set of quantum numbers for  $m = 0$  is provided in Table A.6. The units for the intensity scale are Jy/beam for the ALMA data and main beam antenna temperature for the IRAM 30 m telescope. A  $v_{t,SR}$  of  $+9.0 \text{ km s}^{-1}$  is assumed.



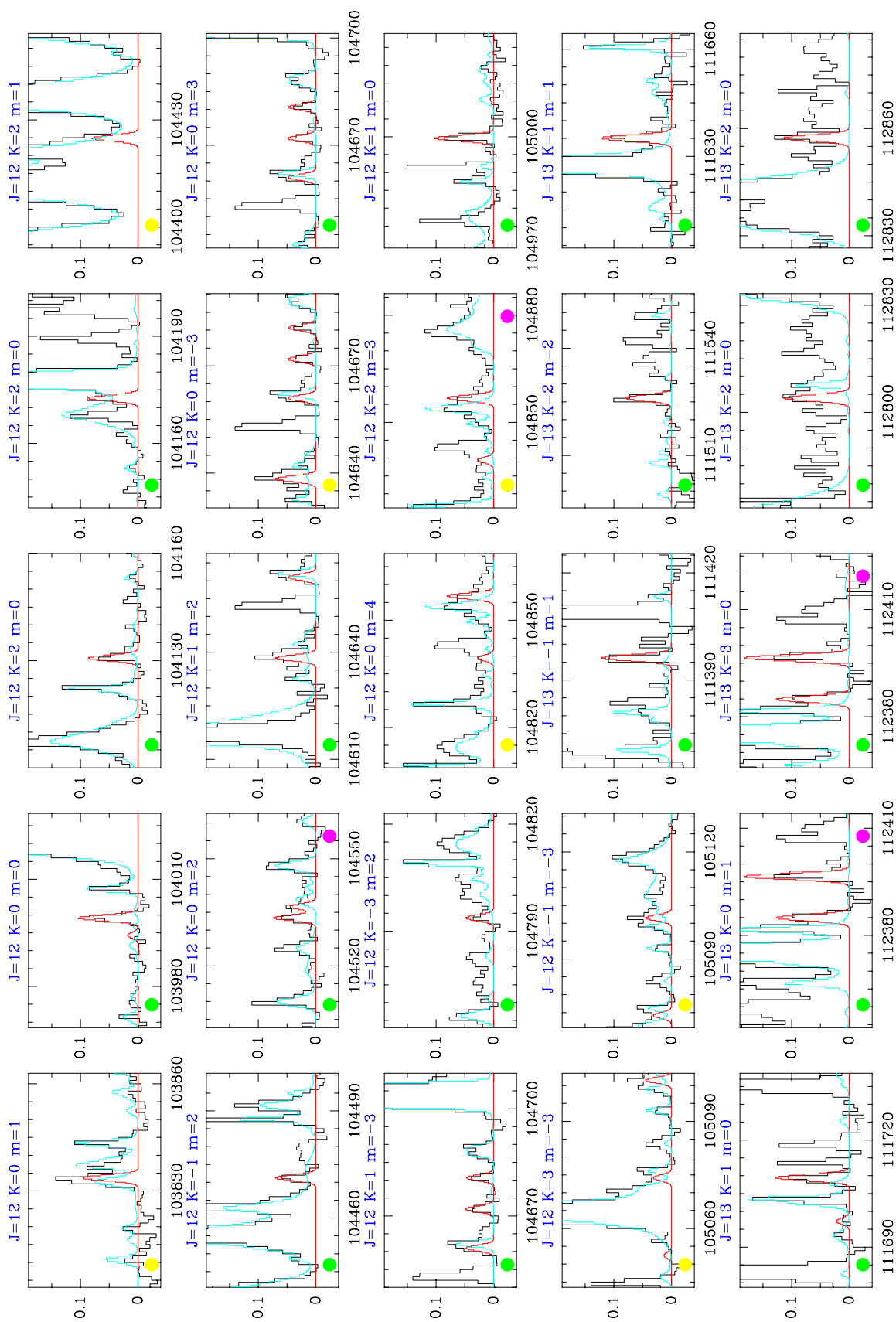


Fig. B.1. continued.

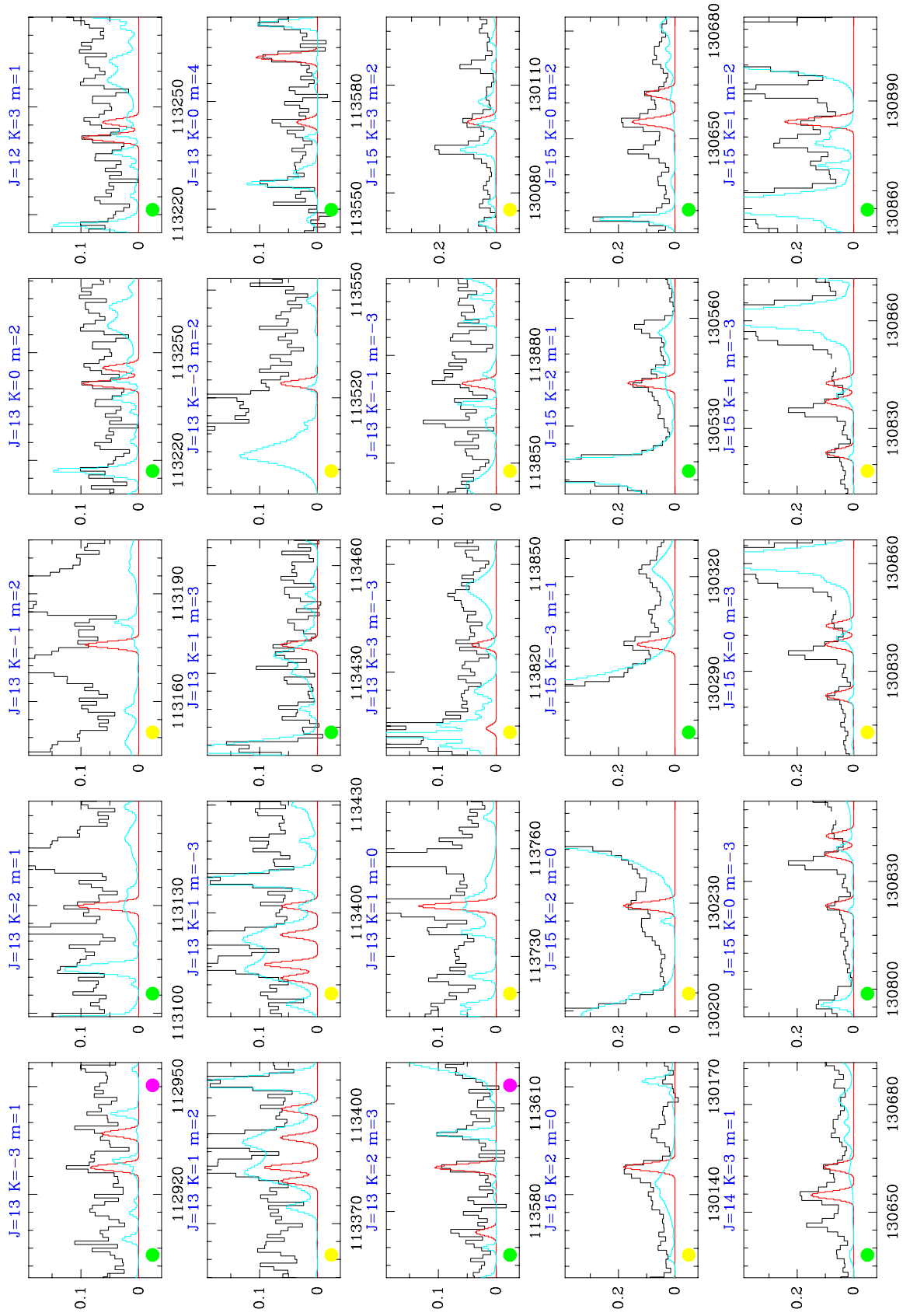


Fig. B.1. continued.

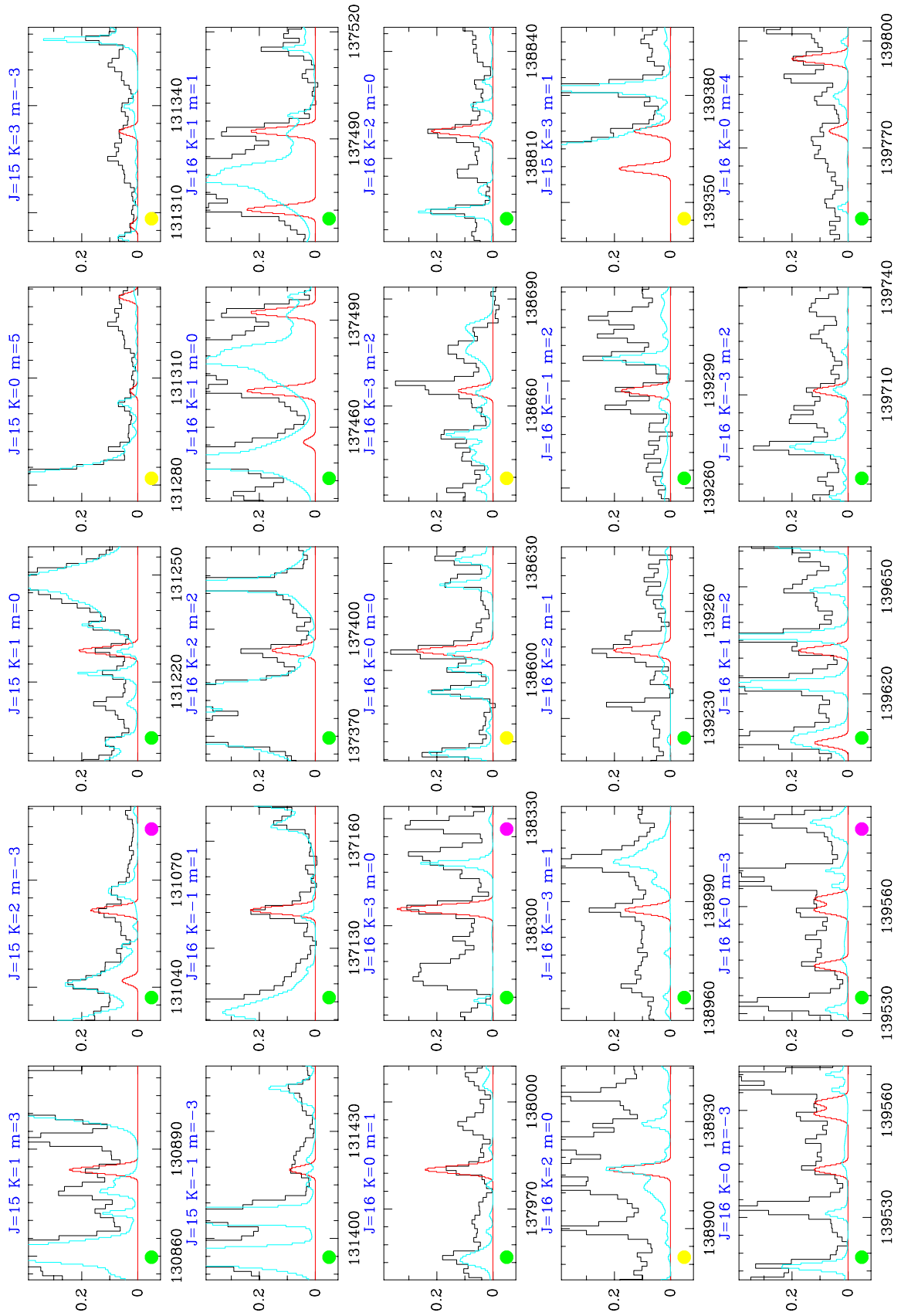


Fig. B.1. continued.

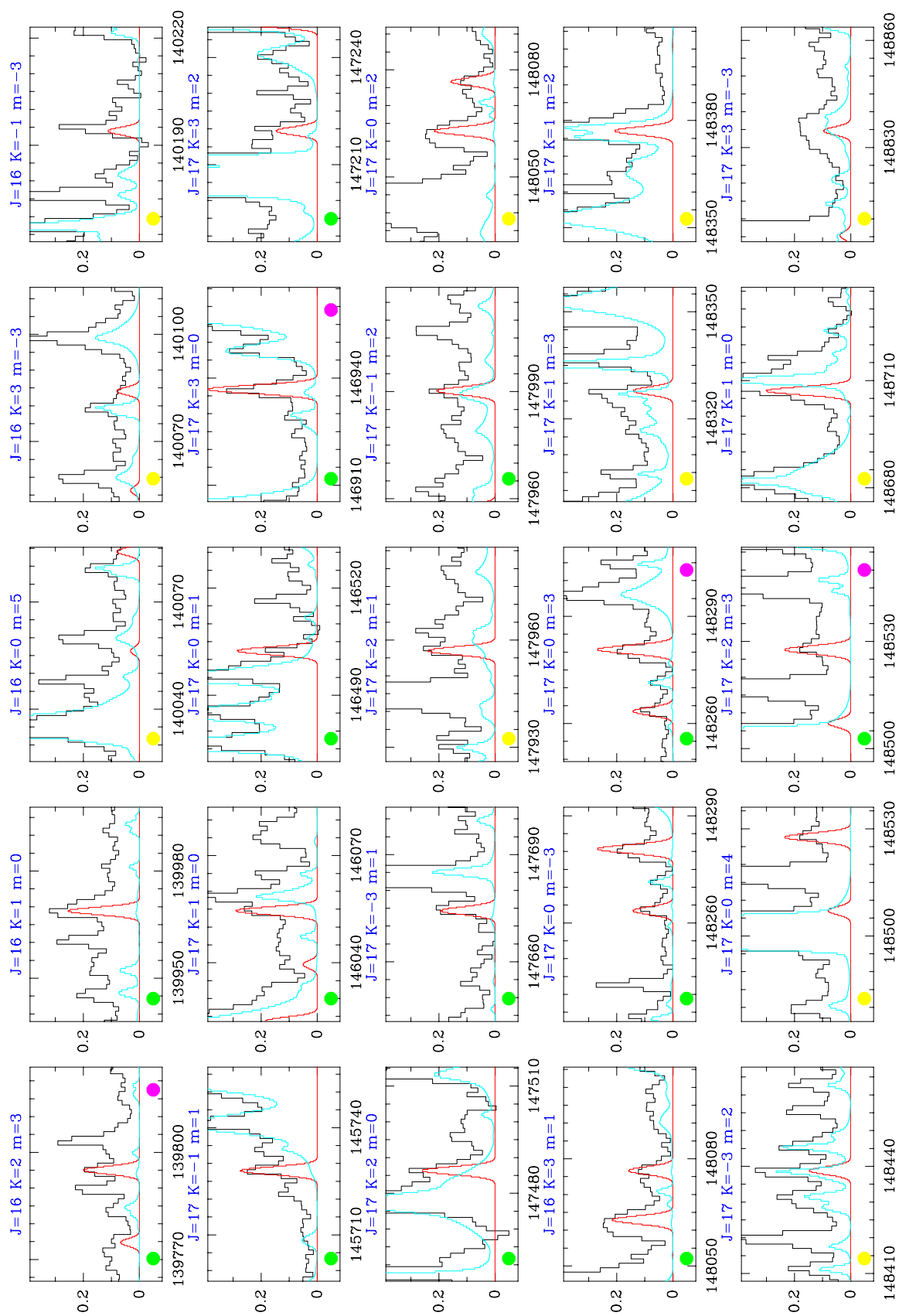


Fig. B.1. continued.

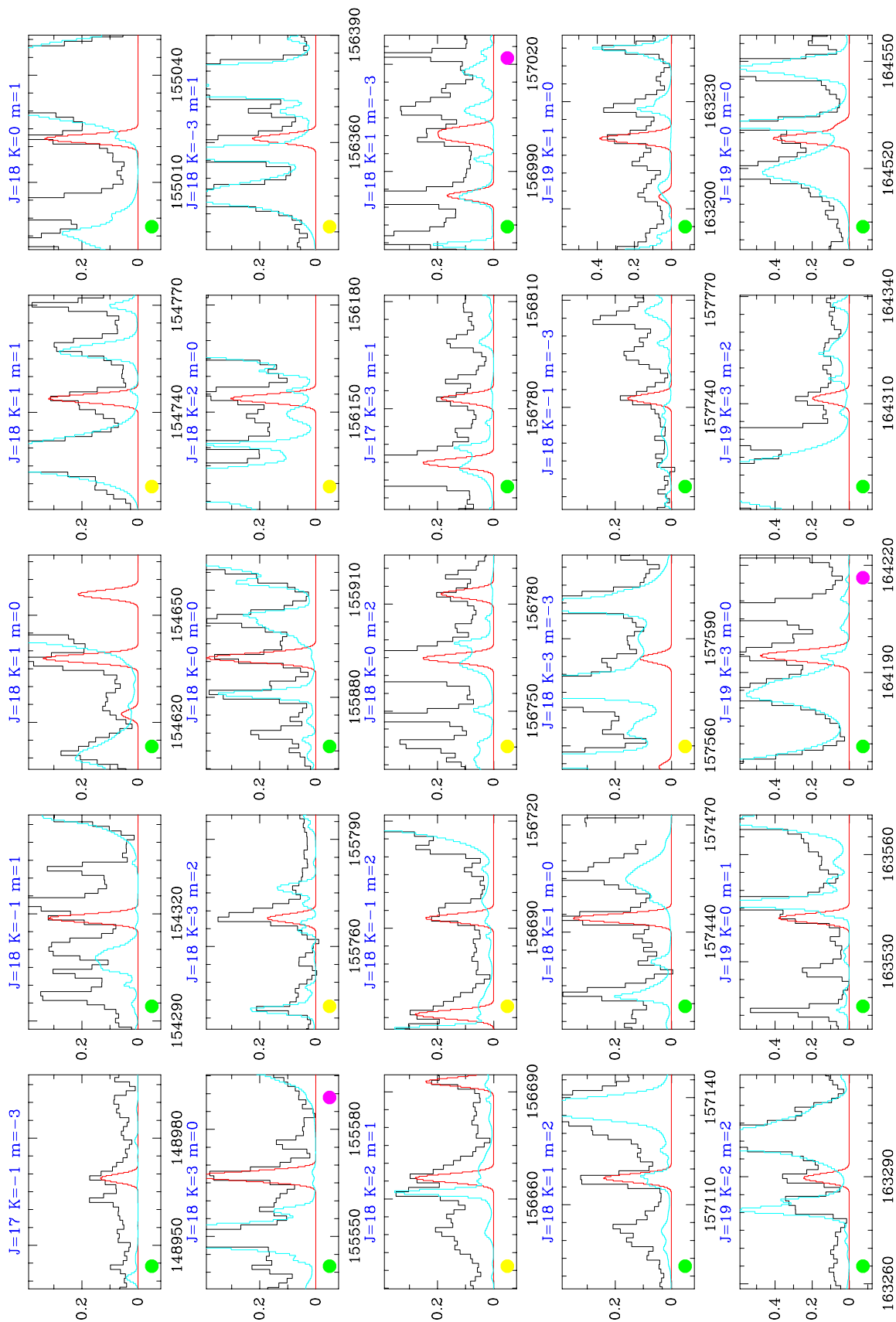


Fig. B.1. continued.

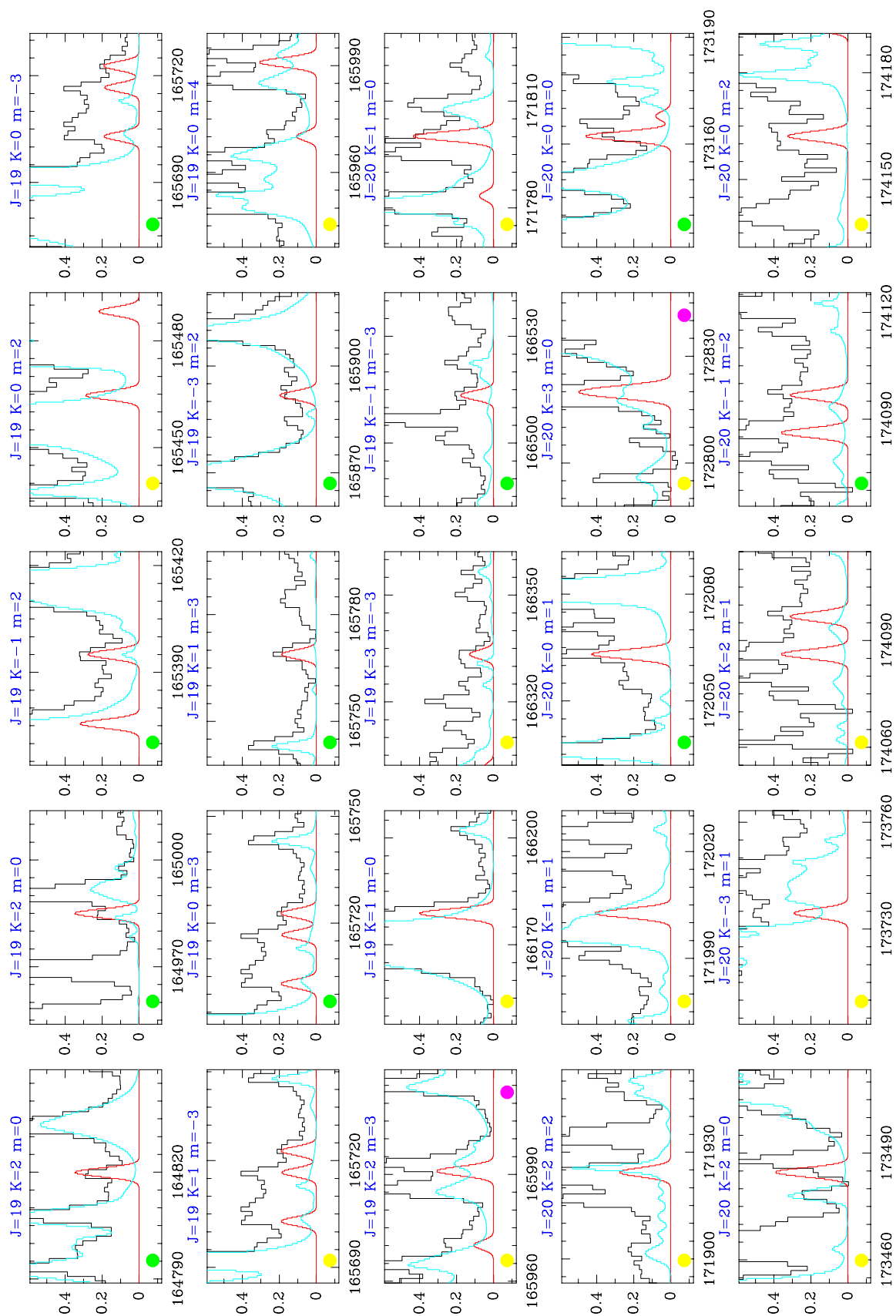


Fig. B.1. continued.

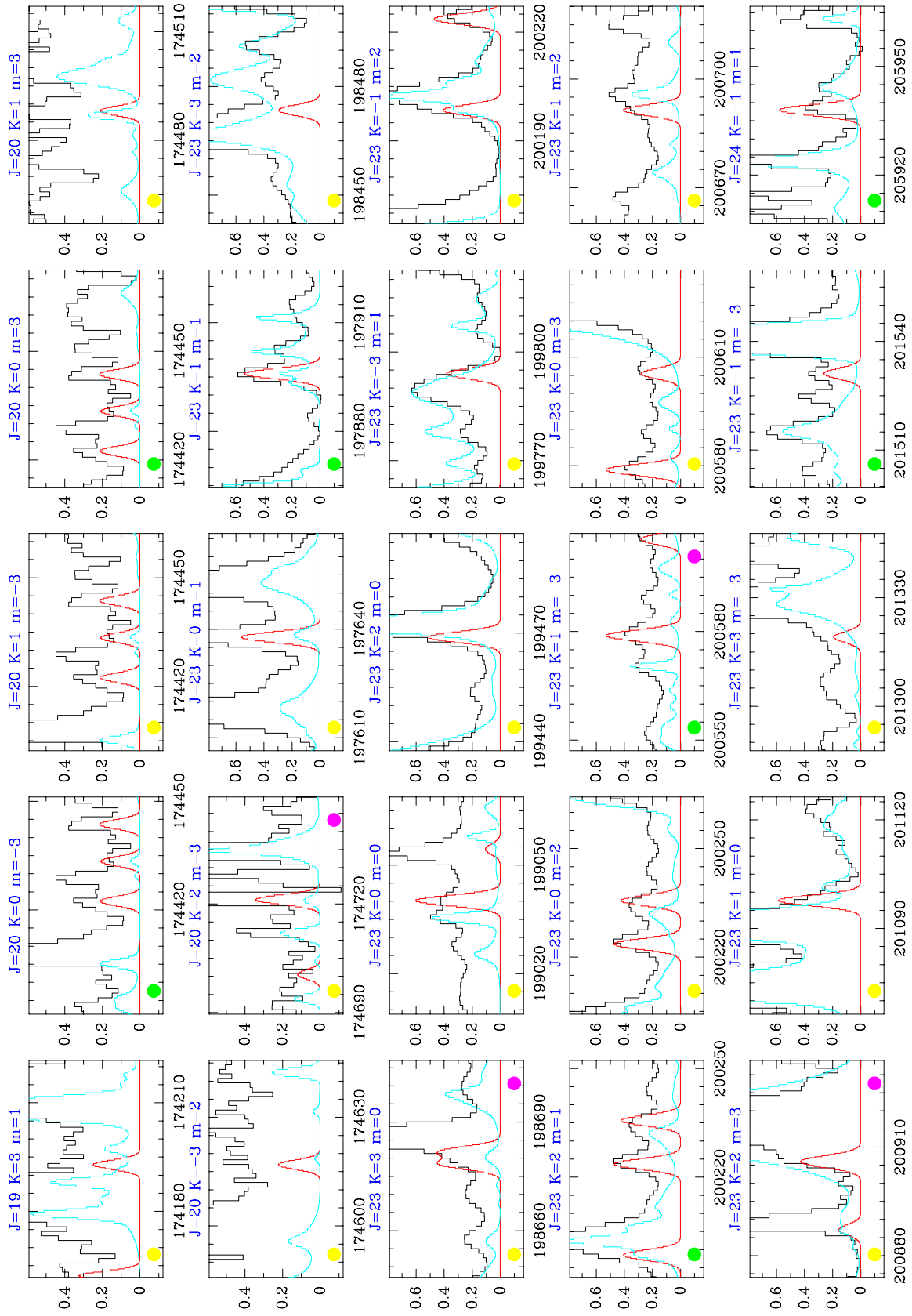


Fig. B.1. continued.

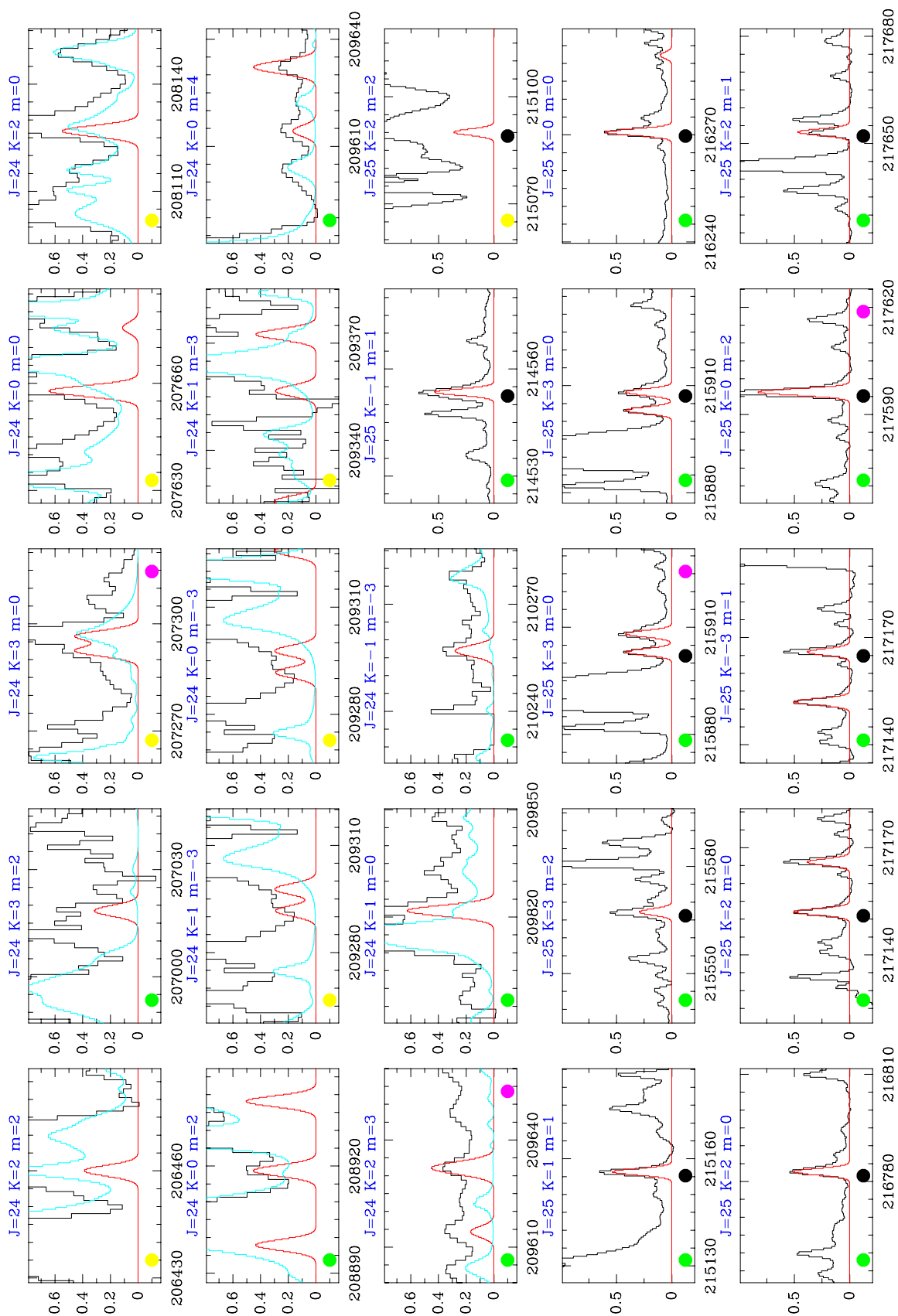


Fig. B.1. continued.

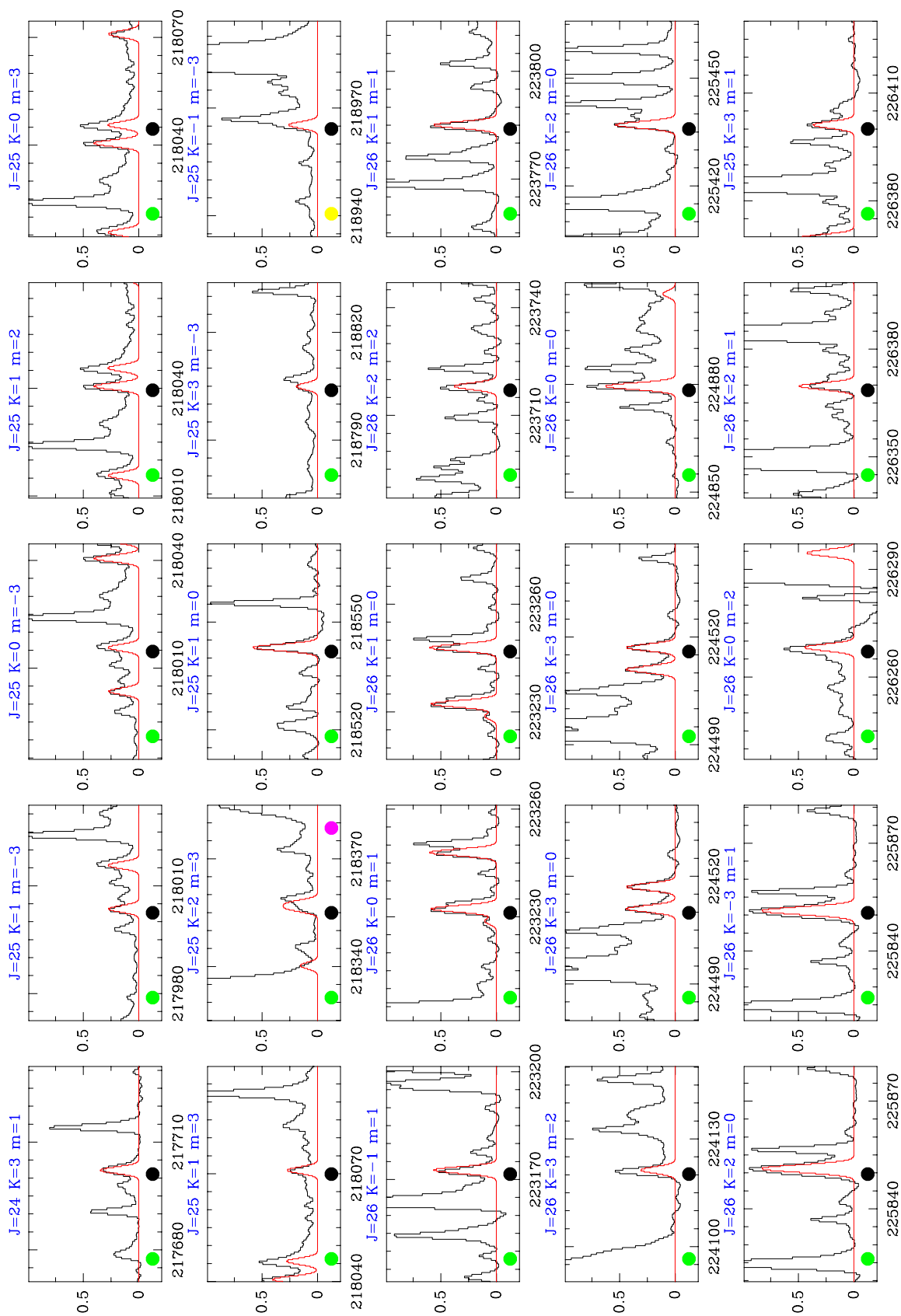


Fig. B.1. continued.

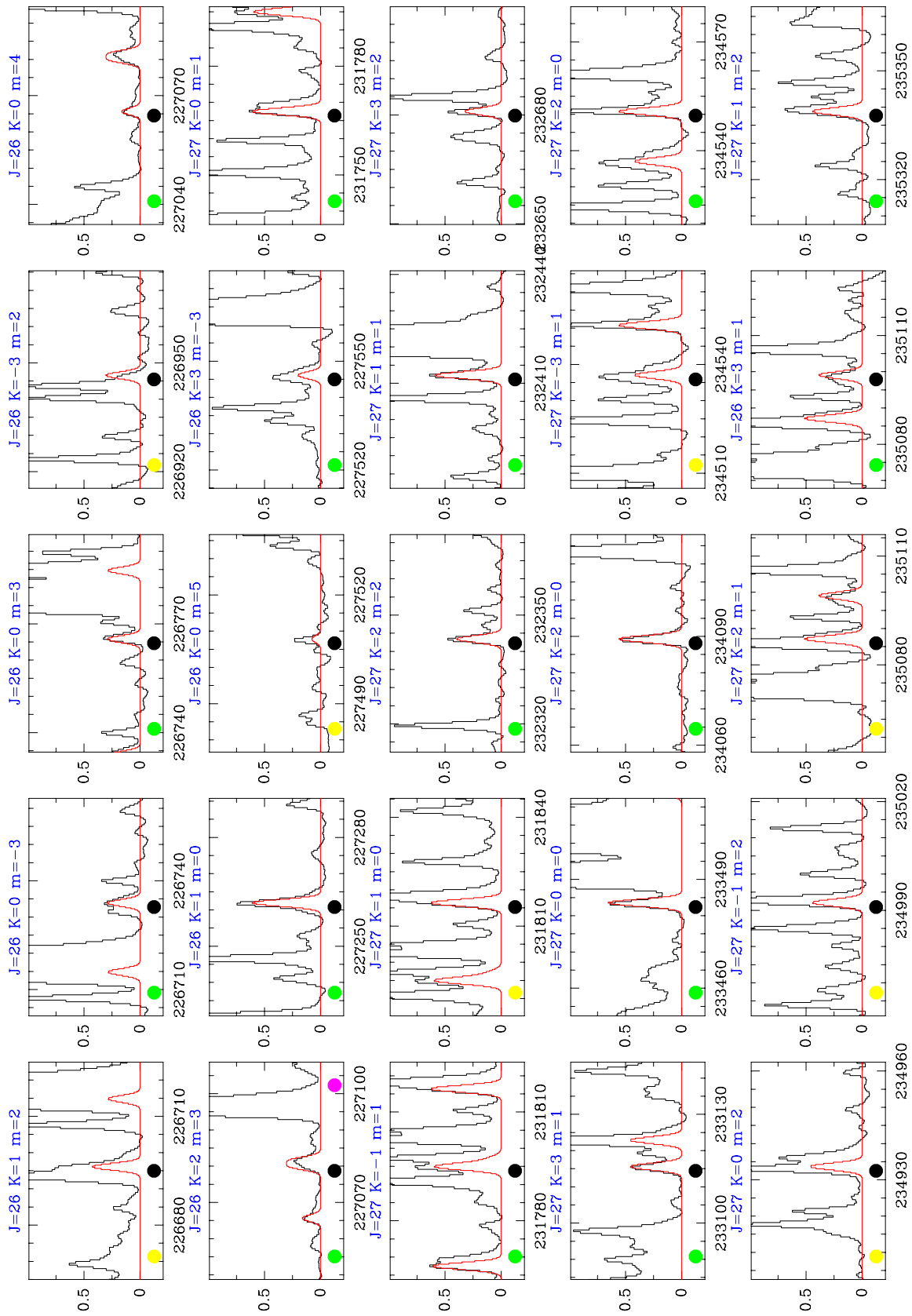


Fig. B.1. continued.

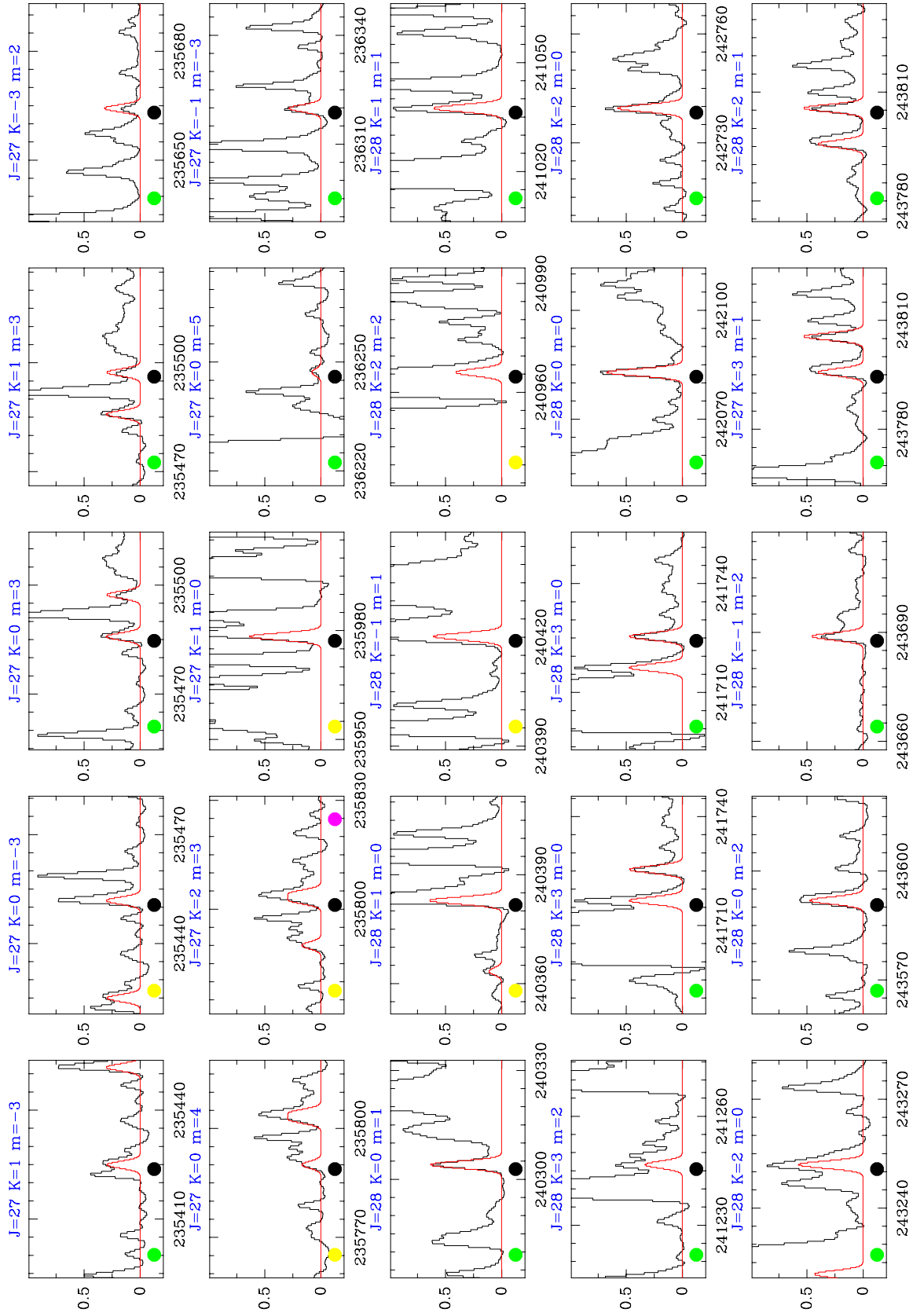


Fig. B.1. continued.

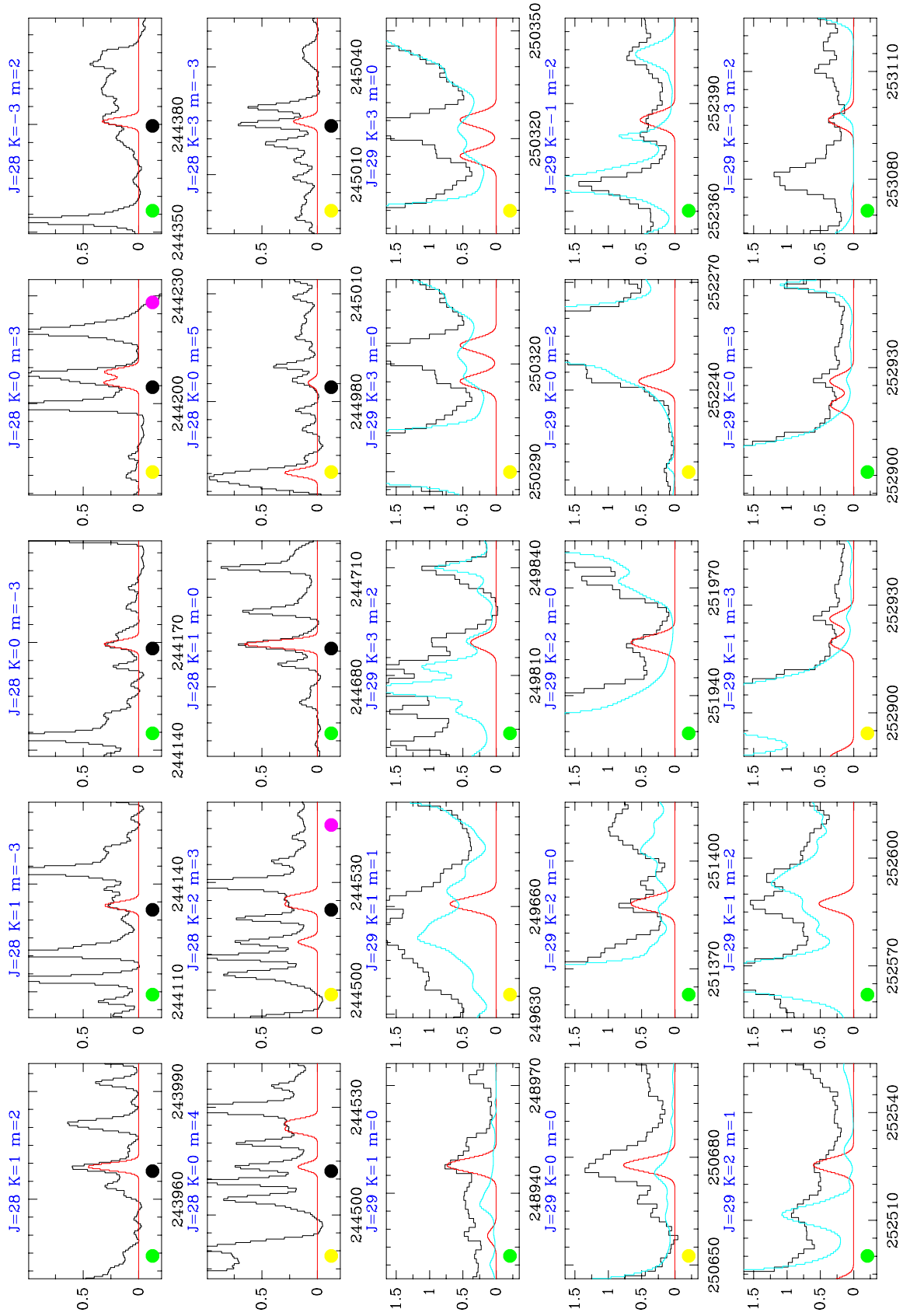


Fig. B.1. continued.

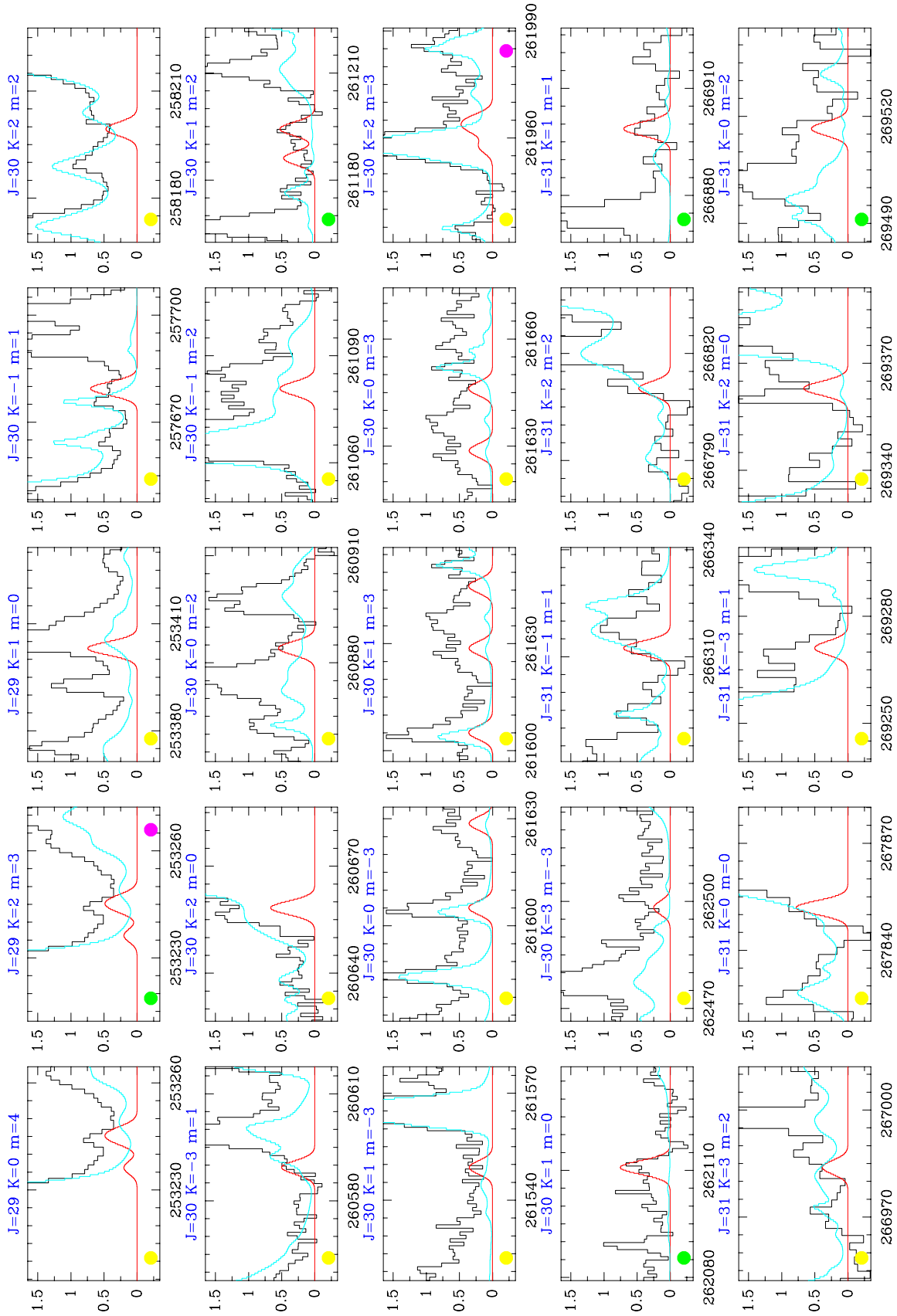


Fig. B.1. continued.

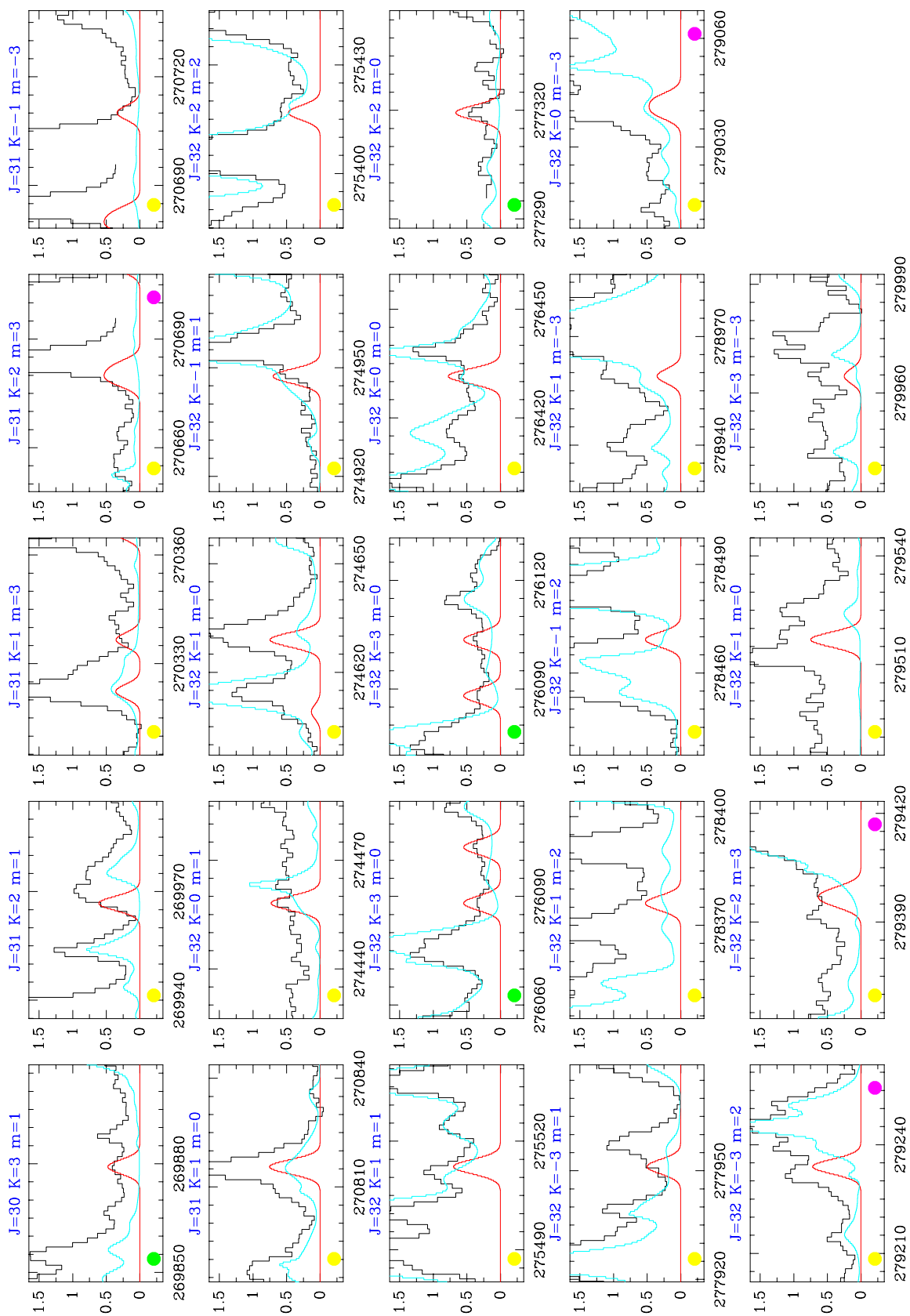
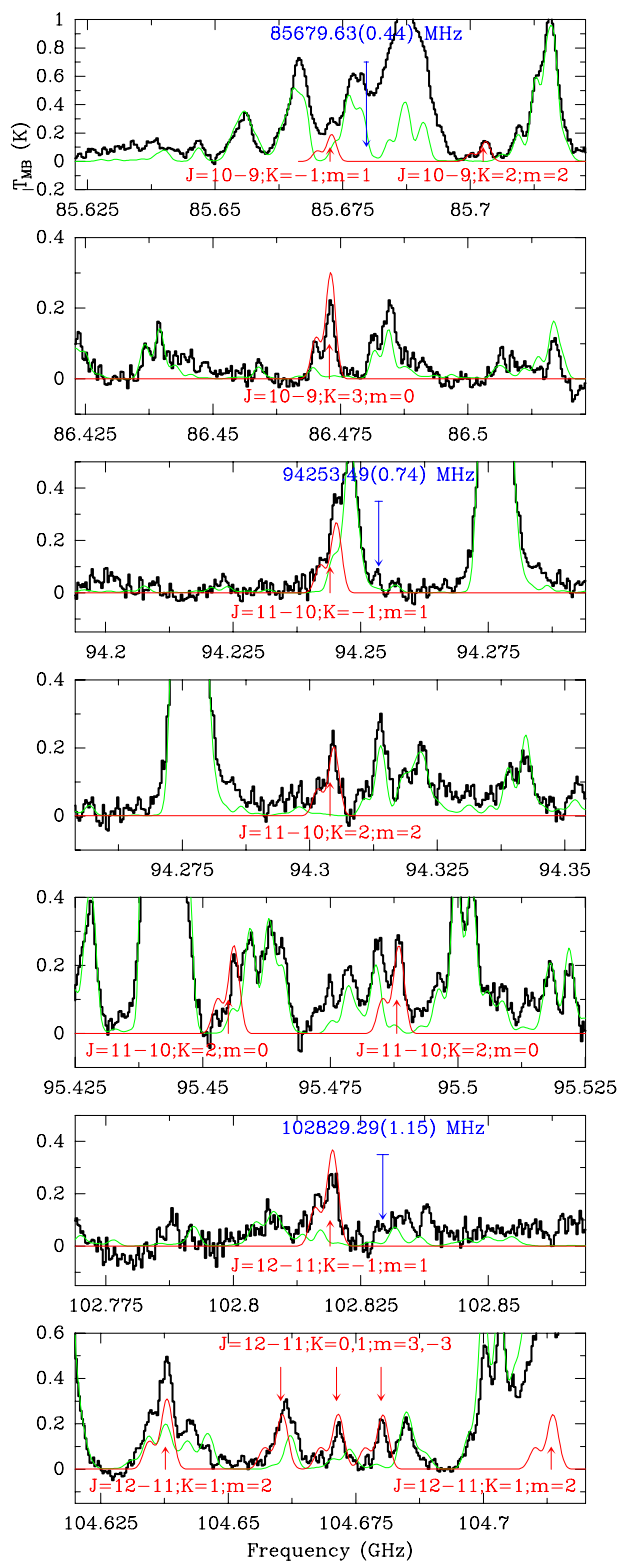
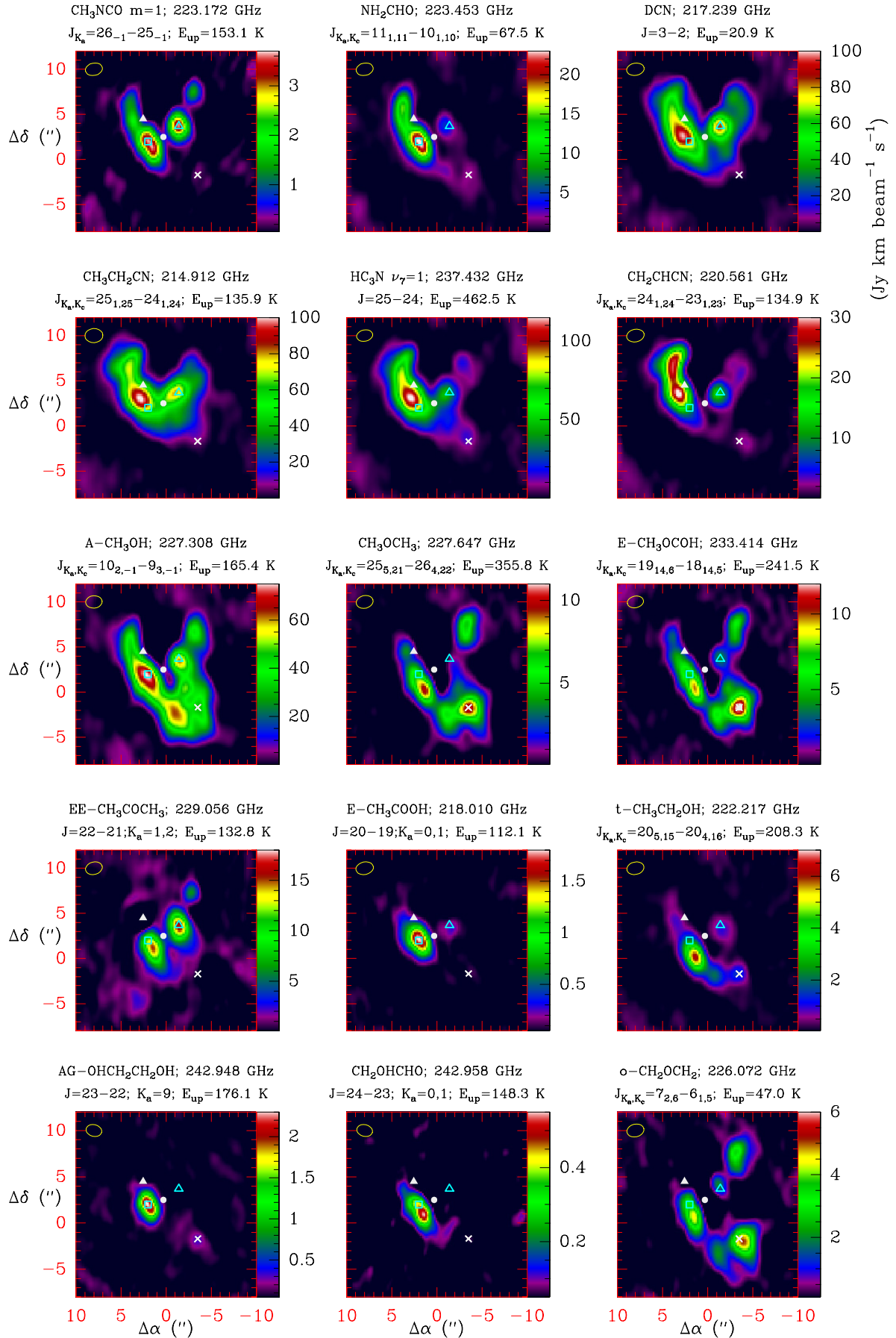


Fig. B.1. continued.



**Fig. B.2.** Selected lines of  $\text{CH}_3\text{NCO}$  in Sgr B2(N) at 3 mm. Observed data (black histogram spectrum) and total model of the source (green curve) are from [Belloche et al. \(2013\)](#). Our best model for  $\text{CH}_3\text{NCO}$  is given by the red line. Frequencies given by [Halfen et al. \(2015\)](#) with their uncertainty are indicated by the blue arrows and lines. A  $v_{\text{LSR}}$  of  $+64.0 \text{ km s}^{-1}$  is assumed.



**Fig. B.3.** Spatial distribution of selected molecules from the ALMA data of Orion between 213–247 GHz (see text).

**Table B.3.** Model for the IRAM 30 m data based on previously analysed molecular species.

Reference	Studied species	Notes
Tercero et al. (2010) <sup>†</sup>	OCS, CS, H <sub>2</sub> CS, HCS <sup>+</sup> , CCS, CCCS	<i>bc</i>
Tercero et al. (2011) <sup>†</sup>	SiO, SiS	<i>bc</i>
Daly et al. (2013) <sup>†</sup>	CH <sub>3</sub> CH <sub>2</sub> CN	<i>abc</i>
Esplugues et al. (2013a) <sup>†</sup>	SO, SO <sub>2</sub>	<i>bc</i>
Esplugues et al. (2013b) <sup>†</sup>	HC <sub>3</sub> N, HC <sub>5</sub> N	<i>bcd</i>
López et al. (2014) <sup>†</sup>	CH <sub>2</sub> CHCN	<i>abc</i>
Marcelino et al. (in prep.) <sup>†</sup>	HCN, HNC, HCO <sup>+</sup>	<i>bcd</i>
Demyk et al. (2007)	<sup>13</sup> C-CH <sub>3</sub> CH <sub>2</sub> CN	<i>ac</i>
Margulès et al. (2009)	CH <sub>3</sub> CH <sub>2</sub> C <sup>15</sup> N, CH <sub>3</sub> CHDCN, CH <sub>2</sub> DCH <sub>2</sub> CN	<i>ac</i>
Carvajal et al. (2009)	<sup>13</sup> C-HCOOCH <sub>3</sub>	<i>ac</i>
Marcelino et al. (2009)	HNCO	<i>c</i>
Margulès et al. (2010)	DCOOCH <sub>3</sub>	<i>ac</i>
Tercero et al. (2012)	<sup>18</sup> O-HCOOCH <sub>3</sub>	<i>ac</i>
Motiyenko et al. (2012)	NH <sub>2</sub> CHO, NH <sub>2</sub> CHO $v_{12} = 1$	<i>ac</i>
Coudert et al. (2013)	HCOOCH <sub>2</sub> D	<i>ac</i>
Tercero et al. (2013)	CH <sub>3</sub> COOCH <sub>3</sub> , CH <sub>3</sub> CH <sub>2</sub> OCOH	<i>ac</i>
Cernicharo et al. (2013)	NH <sub>3</sub> D <sup>+</sup>	<i>ac</i>
Kolesníková et al. (2013)	c-C <sub>6</sub> H <sub>5</sub> OH (not detected)	<i>ac</i>
Haykal et al. (2013)	CH <sub>2</sub> CHCH <sub>2</sub> CN (not detected)	<i>ac</i>
Bell et al. (2014)	CH <sub>3</sub> CN	<i>bc</i>
Kolesníková et al. (2014)	CH <sub>3</sub> CH <sub>2</sub> SH, CH <sub>3</sub> SH, CH <sub>3</sub> OH, <sup>13</sup> CH <sub>3</sub> OH, CH <sub>3</sub> CH <sub>2</sub> OH	<i>ac</i>
Haykal et al. (2014)	<sup>13</sup> C-HCOOCH <sub>3</sub> $v_t=1$	<i>ac</i>
Tercero et al. (2015)	CH <sub>3</sub> CH <sub>2</sub> OCH <sub>3</sub>	<i>ce</i>
Kolesníková et al. (2015)	CH <sub>3</sub> COOCH <sub>2</sub> (not detected)	<i>ace</i>
Alonso et al. (2015)	CH <sub>2</sub> CHCOOH (not detected)	<i>ace</i>
López et al. (in prep.)	HCOOCH <sub>3</sub> $v_t=0,1,2$ , CH <sub>3</sub> COOH $v_t=0,1,2$ , CH <sub>2</sub> OHCHO	<i>ce</i>
In progress	CH <sub>2</sub> OCH <sub>2</sub> , AG-OHCH <sub>2</sub> CH <sub>2</sub> OH	<i>c</i>
In progress	<sup>13</sup> C-CH <sub>3</sub> CN, CH <sub>3</sub> CN $v_8=1$	<i>c</i>
In progress	CH <sub>3</sub> OCH <sub>3</sub> , CH <sub>3</sub> COCH <sub>3</sub> , H <sub>2</sub> <sup>13</sup> CO	<i>c</i>

**Notes.** <sup>(†)</sup> In this analysis we have include all isotopologues and vibrational excited states of the molecule. <sup>(a)</sup> Papers in collaboration with spectroscopists. <sup>(b)</sup> Papers dividing the analysis of the Orion surveys in different families of molecules. <sup>(c)</sup> Papers based on the IRAM 30 m 1D-survey (Tercero et al. 2010) and/or 2D-survey (Marcelino et al., in prep.). <sup>(d)</sup> Papers based on *Herschel*/HIFI data. <sup>(e)</sup> Papers based on ALMA SV data.